SANDIA REPORT

High-Speed, Sub-Pull-In Voltage MEMS Switching

Gregory N. Nielson, Michael J. Shaw, Olga B. Spahn, Gregory R. Bogart,
Michael R. Watts, Roy H. Olsson III, Paul Resnick, David Luck,
Steven Brewer, Chris Tigges, Grant Grossetete

Sandia National Laboratories

High-Speed, Sub-Pull-In Voltage MEMS Switching

Gregory N. Nielson[1], Michael J. Shaw[2], Gregory R. Bogart, Olga B. Spahn[3],
Michael R. Watts[4], Roy H. Olsson III[1], Paul Resnick[2], David Luck[2],
Steven Brewer, Chris Tigges[5], Grant Grossetete[3]

[1]Advanced MEMS
[2]MEMS Core Technologies
[3]RF/Optoelectronics
[4]Applied Photonic Microsystems
[5]Photonic Microsystems Technologies

Sandia National Laboratories
P.O. Box 5800
Albuquerque, NM 87185-1080

Abstract

We have proposed and demonstrated MEMS switching devices that take advantage of the dynamic behavior of the MEMS devices to provide lower voltage actuation and higher switching speeds. We have explored the theory behind these switching techniques and have demonstrated these techniques in a range of devices including MEMS micromirror devices and in-plane parallel plate MEMS switches. In both devices we have demonstrated switching speeds under one microsecond which has essentially been a firm limit in MEMS switching. We also developed low-loss silicon waveguide technology and the ability to incorporate high-permittivity dielectric materials with MEMS. The successful development of these technologies have generated a number of new projects and have increased both the MEMS switching and optics capabilities of Sandia National Laboratories.

Acknowledgements

Table of Contents

Executive Summary

In this report we describe and explore a new concept for switching microelectromechanical systems (MEMS). This approach takes advantage of the dynamic motion of the switch to allow both lower voltage operation and higher-speed switching. Secondary benefits include slower contact speeds which reduces material damage at the contact points and lower energy requirements for operation.

We have applied this switching technique to a number of devices. The first device that we demonstrated this approach on was a relatively large MEMS micromirror device. This device was fabricated and designed under a different project but had the proper structure to allow operation with the new dynamic switching concept. We demonstrated switching at voltages below the pull-in voltage of the structure.

We also designed, fabricated, and tested a series of MEMS micromirrors that were designed to operate at very high speeds. These micromirrors switched in 225 ns, which established a new switching time record for micromirror devices by an order of magnitude. These devices have switching speeds that are competitive with acousto-optic modulators and therefore extend the reach of MEMS micromirrors to a whole new range of applications.

We also demonstrated an in-plane, parallel plate MEMS structure that provides switching in under 500 ns, over a gap of almost 2 mm. This also sets a high-speed switching mark, relative to the switching gap. This device was a precursor to a MEMS integrated optical switch where a MEMS structure is combined with optical waveguides to create a MEMS switching device. As part of this work, low-loss crystalline silicon waveguide technology was developed at Sandia for the first time. These new silicon waveguides have led to a number of new projects and significantly increase the optical technology capability of Sandia National Laboratories. MEMS devices were fabricated that combined the MEMS structures with the waveguides but the waveguides had extremely high loss resulting in an inability to fully test these devices. Work is ongoing in a new project to address the optical loss problem and simplify the fabrication of these switches.

Finally, some exploratory work was done on incorporating high-permittivity materials into MEMS devices. The high-permittivity materials enable lower hold-voltages for MEMS switches which has been the limiting parameter on the switching voltage of these devices. This work experimentally demonstrated the viability of incorporating high-permittivity into MEMS with functional devices.

Overall, this project was highly successful. The dynamic switching mechanisms proposed were demonstrated in a range of devices illustrating both a reduction in voltage required and high-speed switching records. In addition, many new technologies were developed that have spawned a range of new projects. These results squarely place Sandia National Laboratories at the forefront of high-speed MEMS switching.
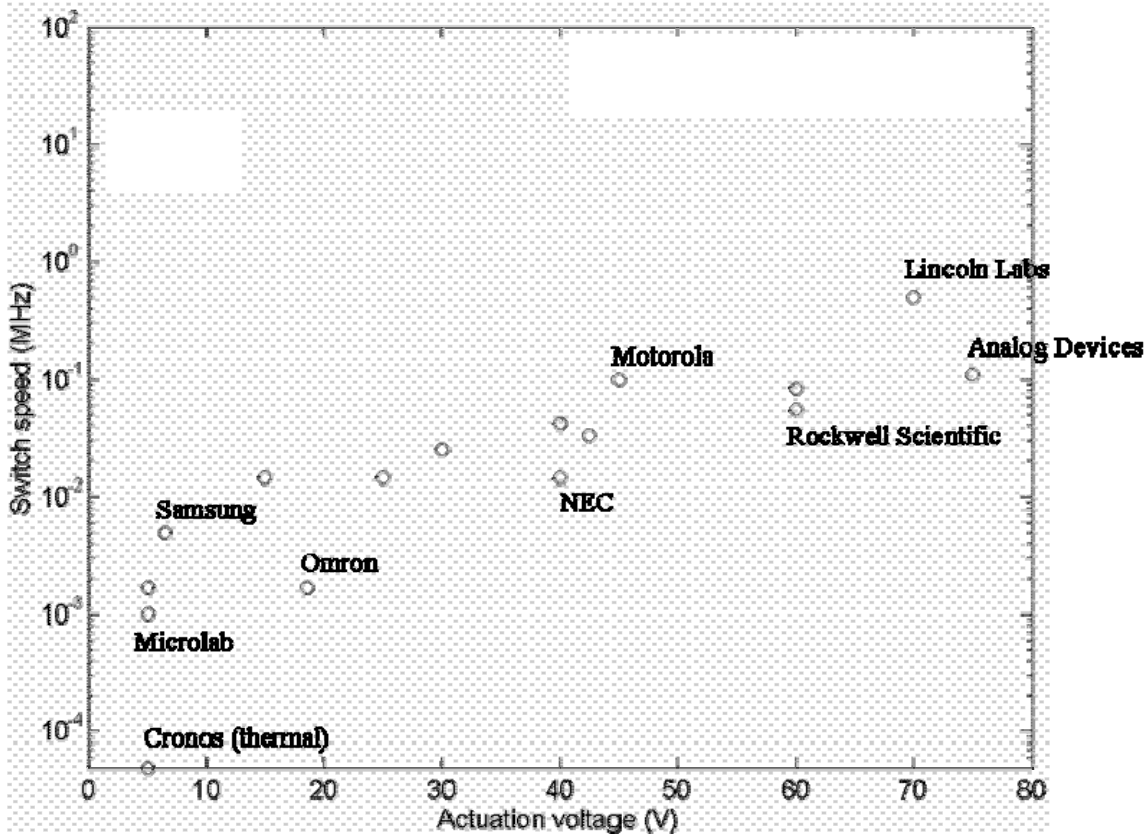
Figure 1.1 Switching speed versus actuation voltage for a number of RF MEMS switches [1]. Note the clear relation between switching speed and voltage.

1.0 Introduction

MEMS switching has been an area of significant research for a number of years. MEMS switches operate in a number of different domains with the most significant of those being electrical (low frequency), RF, optical, and fluidic. The functional benefits resulting from these switches have been hampered by either high voltage required (i.e. electrostatic and piezoelectric switching) or high power requirements (i.e. thermal and magnetic switching). In addition, all of these switching techniques have been hampered by slow switching speeds. Many mechanisms switch in speeds on the order of milliseconds while the fastest devices have been limited to at best a few microseconds. There is a fundamental relation between switching speed and voltage for electrostatic MEMS switches that dictates the speed achievable with MEMS devices. Figure 1.1 shows a number of RF MEMS switches developed by a number of research labs and companies that shows the clear relation between switching speed and voltage.

Standard electrostatic MEMS switching operates under quasistatic conditions. If the dynamic behavior is considered, and taken advantage of, the relation between the switching speed and voltage follows a different relation that allows both a decrease in voltage and a decrease in switching time. To achieve this requires that the MEMS device be designed specifically for dynamic electrostatic MEMS switching.

9

Through these techniques, we demonstrate both a reduction in actuation voltage and an increase in switching speed for both torsional and parallel plate devices. The trade-off to these dynamic switching techniques is that the control of the devices becomes more complex than for the simple quasistatic switching case. Judgment needs to be exercised in determining which switching technique provides the best performance for a given application.
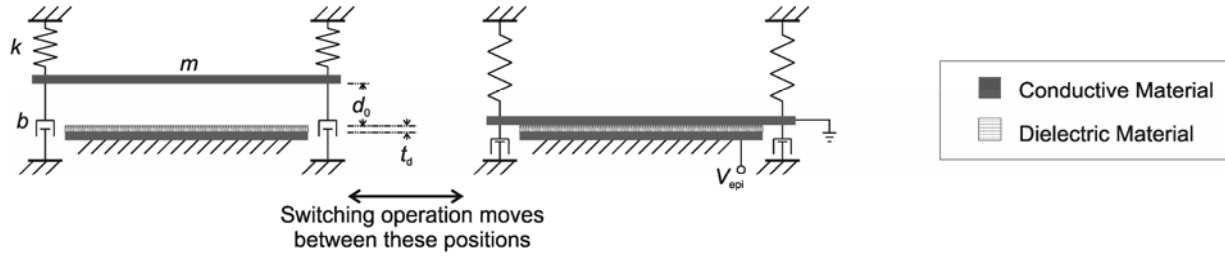
Figure 2.1 Lumped parameter model of a standard parallel plate electrostatic actuator showing the open and closed position of the switch [2].

2.0 Dynamic Switching Theory

Taking advantage of the dynamic behavior of MEMS switches significantly improves the performance achievable. To understand the benefits of operating MEMS switches according to the dynamic switching principles requires first an understanding of standard electrostatic MEMS switching, since the behavior that enables dynamic switching is based on the standard switching technique.

2.1 Standard Electrostatic MEMS Switching

An electrostatic MEMS switch is comprised of two parallel plate electrodes, one of which is fixed and the other is suspended by a compliant structure that allows it to move. When a voltage is applied across the two plates, opposite signed charges build up on the two plates which exert an attractive force that pulls the plates together. Because of the nonlinearity of the force resulting from the electrostatic attraction, the plates experience an equilibrium bifurcation that results in a "pull-in" effect. This pull-in effect occurs at a voltage level defined by the design of the structure and is referred to as the pull-in voltage. This behavior is readily shown by analyzing the equations of motion of a lumped parameter model of an electrostatic switch.

Figure 2.1 shows a lumped parameter model of a standard parallel plate electrostatic MEMS switch. The equation of motion for the movable plate is

$$m\ddot{x} + b\dot{x} + kx = \frac{\varepsilon A V^2}{2(d_0 - x)^2} \, , \qquad (2.1)$$

where m is the mass of the plate, k is the spring constant of the suspending structure, b is the damping coefficient of the system, ε is the permittivity of free space, A is the overlap area of the two electrodes, d_0 is the initial gap between the plates, and x is the displacement of the movable plate from its equilibrium position.

According to standard operation, quasistatic conditions are assumed which allows the velocity and acceleration terms to be neglected. Solving then for the voltage gives

$$V = \sqrt{\frac{2kx(d_0 - x)^2}{\varepsilon A}} \; . \qquad (2.2)$$

Equation 2.2 has a local maximum at $x = d_0/3$. This point is the position at which the pull-in phenomenon occurs. The voltage associated with this pull-in position is
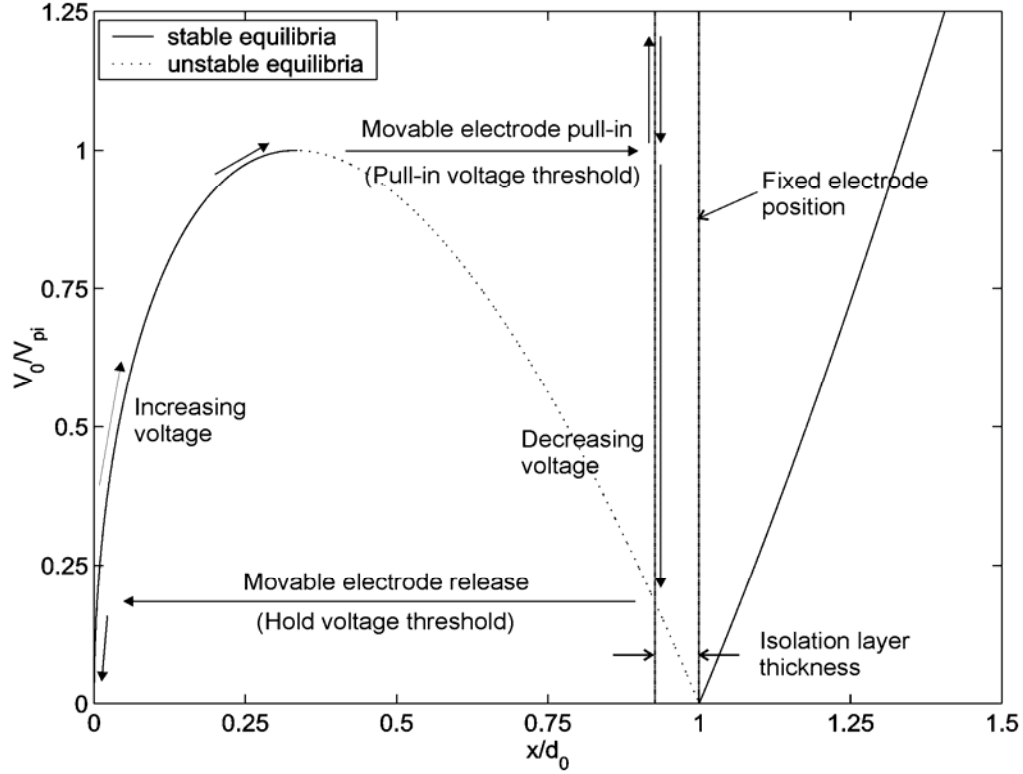
Figure 2.2 Applied voltage versus displacement equilibrium curve for a parallel plate electrostatic actuator [3].

$$V_{pi} = \sqrt{\frac{8kd_0^3}{27\varepsilon A}} \, . \tag{2.3}$$

Equation 2.2 is plotted in Figure 2.2 with the voltage scaled by the pull-in voltage and the displacement, x, scaled by d_0. The typical mode of operation of an electrostatic switch is also depicted in the Figure 2.2. The voltage is increased until it exceeds the pull-in voltage which causes the movable plate to snap into the pulled-in position. The pulled-in position is defined by the dielectric material or mechanical stops that keeps the two plates from touching and electrically shorting. We will refer to this air or dielectric layer as the isolation layer thickness, t_d. To release the plate from the pulled-in position requires that the applied voltage be lowered until it reaches the hold voltage threshold level. At this point, the movable electrode snaps free from the isolation layer. The hold voltage level is given by

$$V_h = \sqrt{\frac{2k(d_0 - t_d)t_d^2}{\varepsilon A}} \, . \tag{2.4}$$
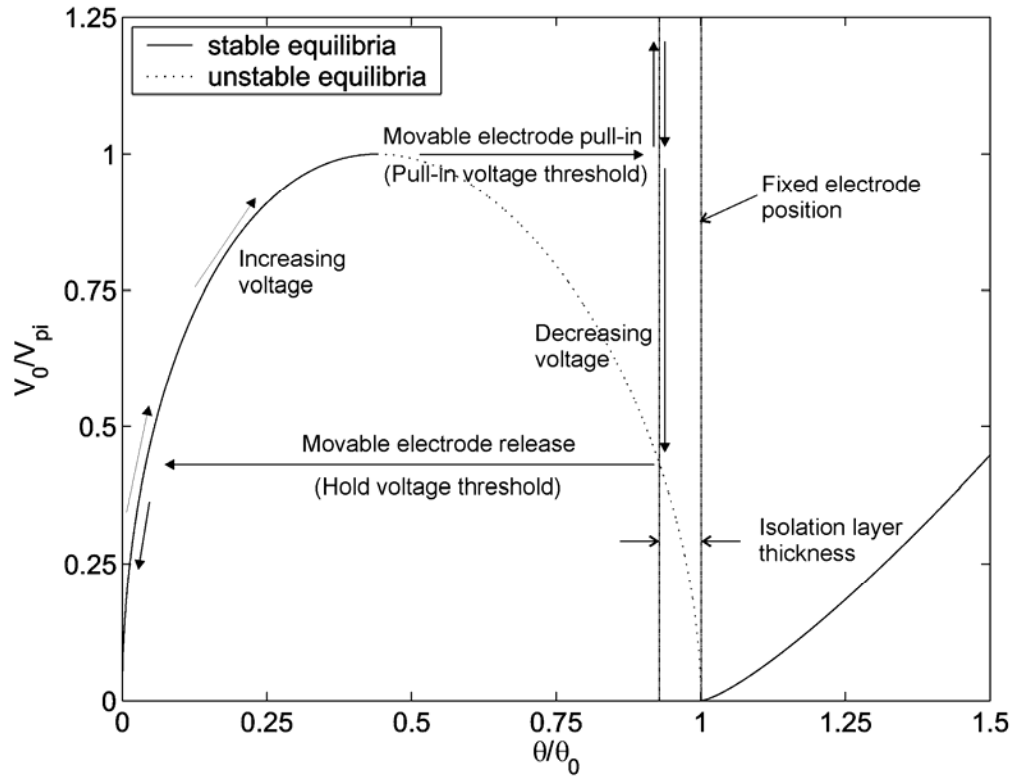
Figure 2.3 Applied voltage versus displacement equilibrium curve for a torsional electrostatic actuator [3].

Note that the isolation layer thickness determines the level of the hold voltage. If the layer is very thin, the hold voltage will be very low. The minimum isolation layer thickness is determined by the actuation voltage required by the switch and the breakdown field of the isolation layer material. In Equation 2.4, we assume that the relative permittivity of the isolation layer is unity but this is often not the case. By using an isolation material with a higher permittivity, the hold voltage is reduced for a constant isolation layer thickness. For dynamic switching, this can be a desirable mechanism and is explored in Section 6.0.

A comparable derivation is possible for torsional electrostatic MEMS switches. The behavior is similar to the parallel plate structure, with some subtle differences. For instance, the local maximum associated with the pull-in phenomenon is shifted slightly to the right. The equilibrium curve associated with the torsional electrostatic actuator is plotted in Figure 2.3. For the full derivation of the torsional switch behavior, see [3] reprinted in Appendix A.
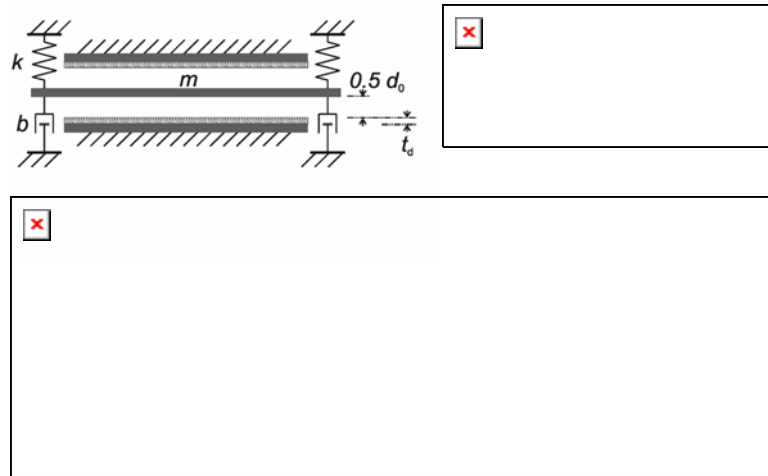
Figure 2.4 Lumped parameter model of the structure required for dynamic operation of a parallel plate electrostatic actuator. The two pulled-in positions, which constitute the two switch positions during operation, are also shown [2].

2.2 Dynamic Electrostatic MEMS Switching

The dynamic switching approach requires a more complex structure than that shown in Figure 2.1. One additional fixed electrode or plate is required and needs to be positioned such that the two fixed electrodes are symmetrically located around the movable plates' zero bias equilibrium position. The switch operates between the two pulled-in positions defined by the fixed electrodes. Figure 2.4 shows the required electrode arrangement for a parallel plate actuator with the two switch positions during operation.

For a torsional switch, the structure required for dynamic switching is the same structure typically used for standard torsional switching. A lumped parameter model illustrating this structure is shown in Figure 2.5. In this case, the switch rotates from one pulled-in position to the opposing pulled-in position. This means that most torsional electrostatic MEMS switches can operate with the dynamic switching technique as constituted.
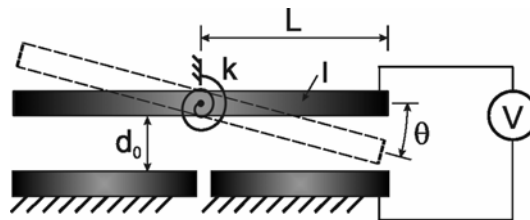
Figure 2.5 Lumped parameter model of a torsional electrostatic actuator. Note the two fixed electrodes placed symmetrically relative to the rotating electrode.

Dynamic switching operates between the two opposing pulled-in positions defined by the two fixed electrodes on either side of the moving electrode's unactuated equilibrium position. Because the switch is always in one of two pulled-in states, the switch always possesses stored energy in the mechanical domain to drive switching.

The switch operation is initiated by the release of the voltage holding the movable electrode in its

14

initial pulled-in position. Upon release from one pulled-in position, the movable electrode will accelerate, overshoot its equilibrium position, and come near the second fixed electrode if the system is underdamped. Due to this close proximity, the second electrode can catch and hold the movable electrode in a pulled-in position with a voltage less than the pull-in voltage.

The hold voltage, defined in Equation 2.4, is the lower limit of the actuation voltage for the dynamic switching technique; however, the actuation voltage may need to be higher if the mechanical resonance quality factor is too low. A quality factor as low as five can provide an appreciable decrease in the required actuation voltage [2].

Under normal operation, the switch operates at a voltage just above the hold voltage. However, the switch requires initialization (i.e. initial pull-in of the movable electrode from its undeflected equilibrium). This can be achieved by applying a relative large voltage that exceeds the pull-in voltage; however, this then requires that the isolation gap between the electrodes be able to hold off this high voltage and thus be thicker than would be required by just the hold voltage. This additional thickness leads to an increase in the hold voltage and reduces the performance improvements resulting from the dynamic switching approach. However, by again taking advantage of system dynamics, this initial pull-in can also be achieved at a voltage much less than the pull-in voltage [3].

The switch can be initialized by applying a voltage signal at the resonant frequency of the device such that energy is built up in the mechanical resonance of the structure. When there is sufficient energy stored in the mechanical resonance, the device will achieve a pulled-in state. This allows the switch to be initialized at a voltage less than the pull-in voltage of the device.

2.3 Initializing the MEMS Switch (Resonant Pull-in)

The concept behind initialization of the switch with resonant pull-in is that energy is injected into the mechanical system over time and thus allows for a lower voltage to be used than would be required if a simple ramp or step function signal were applied. The lower initialization voltage that is provided by the resonant pull-in technique allows a thinner isolation layer to be used and thus reduces the hold voltage level. Combining the resonant pull-in with the dynamic switching creates a system optimized for the fastest possible switching speed at the lowest voltage possible.

A detailed analysis of the dynamic behavior leading to pull-in was conducted. This analysis is found in [3], included in Appendix A.

2.4 Discussion of Design Considerations

The hold voltage is defined by the effective gap between the electrodes when the suspended structure is in its pulled-in position. The thickness of this gap need not be large but the gap does need be thick enough to maintain electrical isolation between the two electrodes. If the operating voltage is low, the gap can be very narrow.

The isolation gap is sometimes defined by a dielectric material in between the two plates (deposited on either the fixed electrode, the moving electrode, or in some cases both electrodes). In other devices, the isolation layer is created by using mechanical stops to limit the motion of the movable electrode before it comes into contact with the fixed electrode. In this case, the dielectric between the two is air, some other gas, or vacuum.

Whatever comprises the dielectric separating the two electrodes, the key material parameter metric to judge candidate materials by is the product of the relative permittivity of the material

with its dielectric strength. A high permittivity makes a dielectric layer appear thinner to the two electrodes. A high dielectric strength allows a thinner dielectric layer to be used. Thus, both material parameters are equally important in determining the ideal material. As part of this project we explored the use of high-permittivity materials in electrostatic MEMS switches (see Section 6.0).

Another important consideration for the dielectric material used in the MEMS structure is its propensity for dielectric charging. This can be a significant problem for MEMS electrostatic switches. The least likely devices to exhibit dielectric charging are structures where the dielectric layer is defined by mechanical stops. This may not be possible or desirable in all situations. An alternative approach that we used to reduce dielectric charging was to operate the switches in vacuum. We experienced much less charging when we tested our devices in vacuum as compared to air. The vacuum operation also allowed an increased mechanical quality factor which is a benefit to the dynamic switching behavior.

One last design consideration for high-speed MEMS switches is that through particularly good design practices the voltage can be lowered dramatically, thus allowing the stiffness of the MEMS structure to be increased to allow for high-speed switching. However, the stiffness of the structure can only be increased to a certain degree due to limitations imposed by material properties and device geometries. These limitations determine the ultimate speed at which a MEMS device can switch. For the very smallest MEMS (NEMS) switching structures, switching speeds of 1 ns are theoretically possible [4].
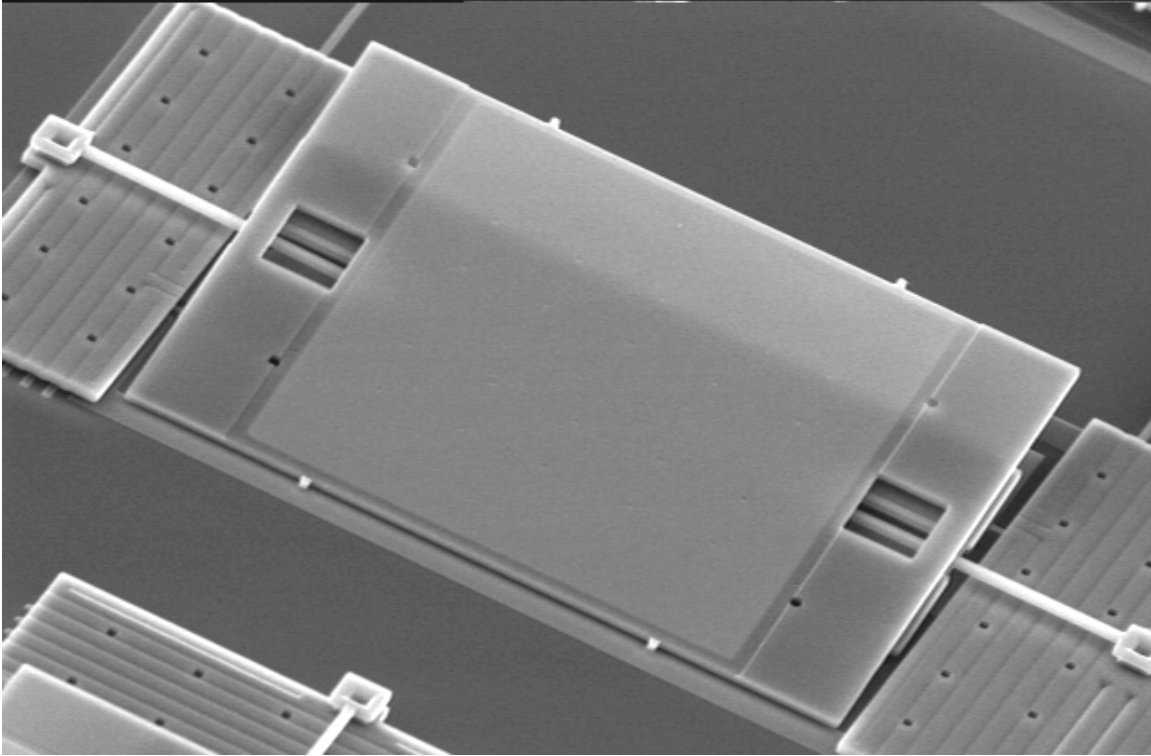
Figure 3.1 SEM of the large MEMS mirror device. The mirror surface is 120 μm by 160 μm.

3.0 Large MEMS Micromirror Switching

For the initial demonstration of the dynamic switching technique we took advantage of the fact that most torsional micromirror devices have the required structure for dynamic switching. A lumped parameter model of the structure of a MEMS micromirror device is illustrated in Figure 2.5.

3.1 Mirror Device

The device we used was a relatively large MEMS micromirror device developed at Sandia National Laboratories. An SEM image of the device is in Figure 3.1. This device has both a large mirror surface (120 μm × 160 μm) and a large angular displacement (±10°). This device was designed and fabricated in the SUMMiT V^{TM} process.

3.2 Testing Results

This micromirror device was set up in a test stand that included an illuminating laser, computer control of the actuation voltage of the device, and a position sensitive optical detector (PSD). The output of the PSD was collected and compared with the applied voltages to determine the system response. These tests were all performed in air. The quality factor of the mechanical system was in the range of five to ten.
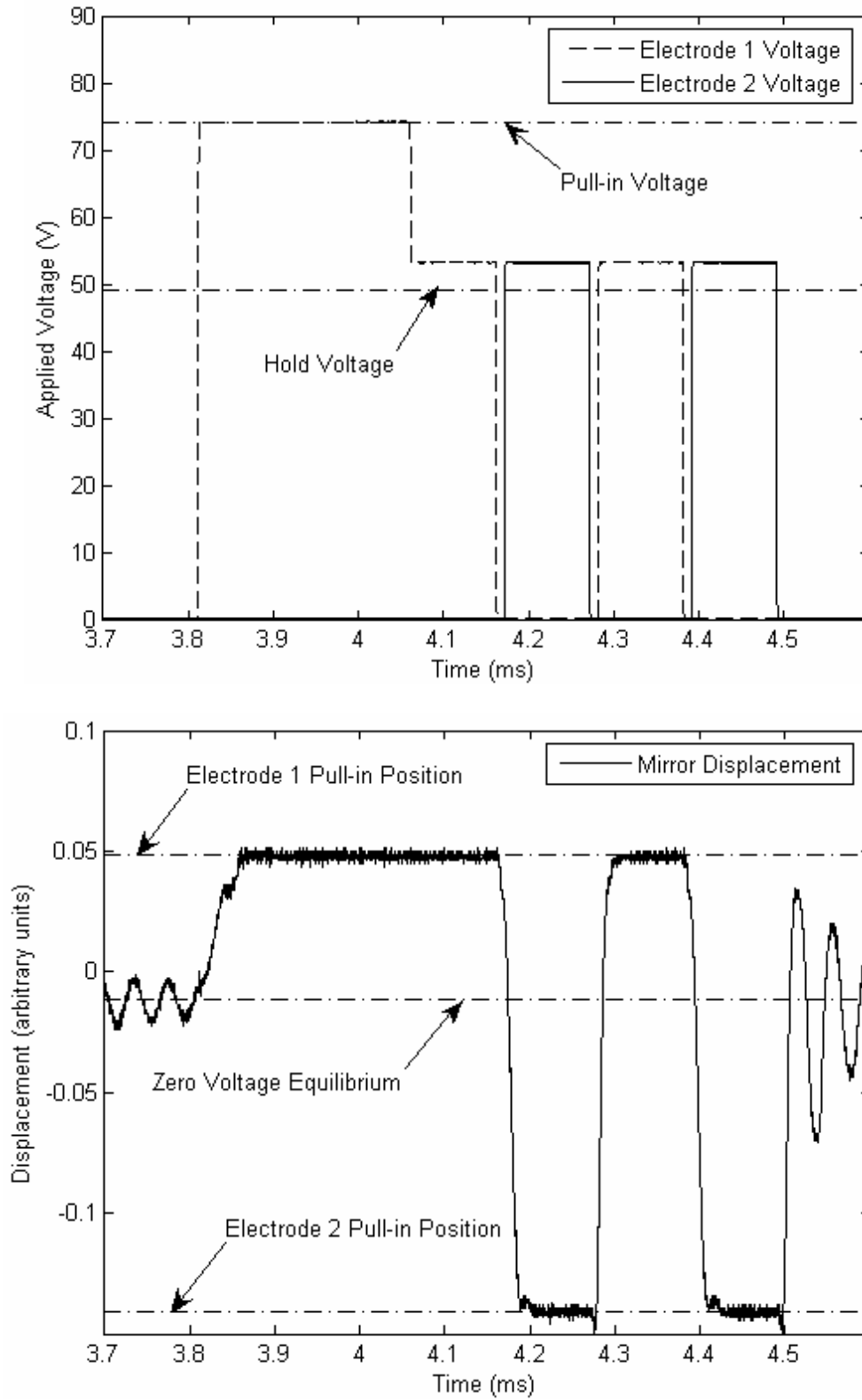
Figure 3.2 Plots showing the applied voltage and the resulting dynamic switching of the large MEMS torsional mirror[2].
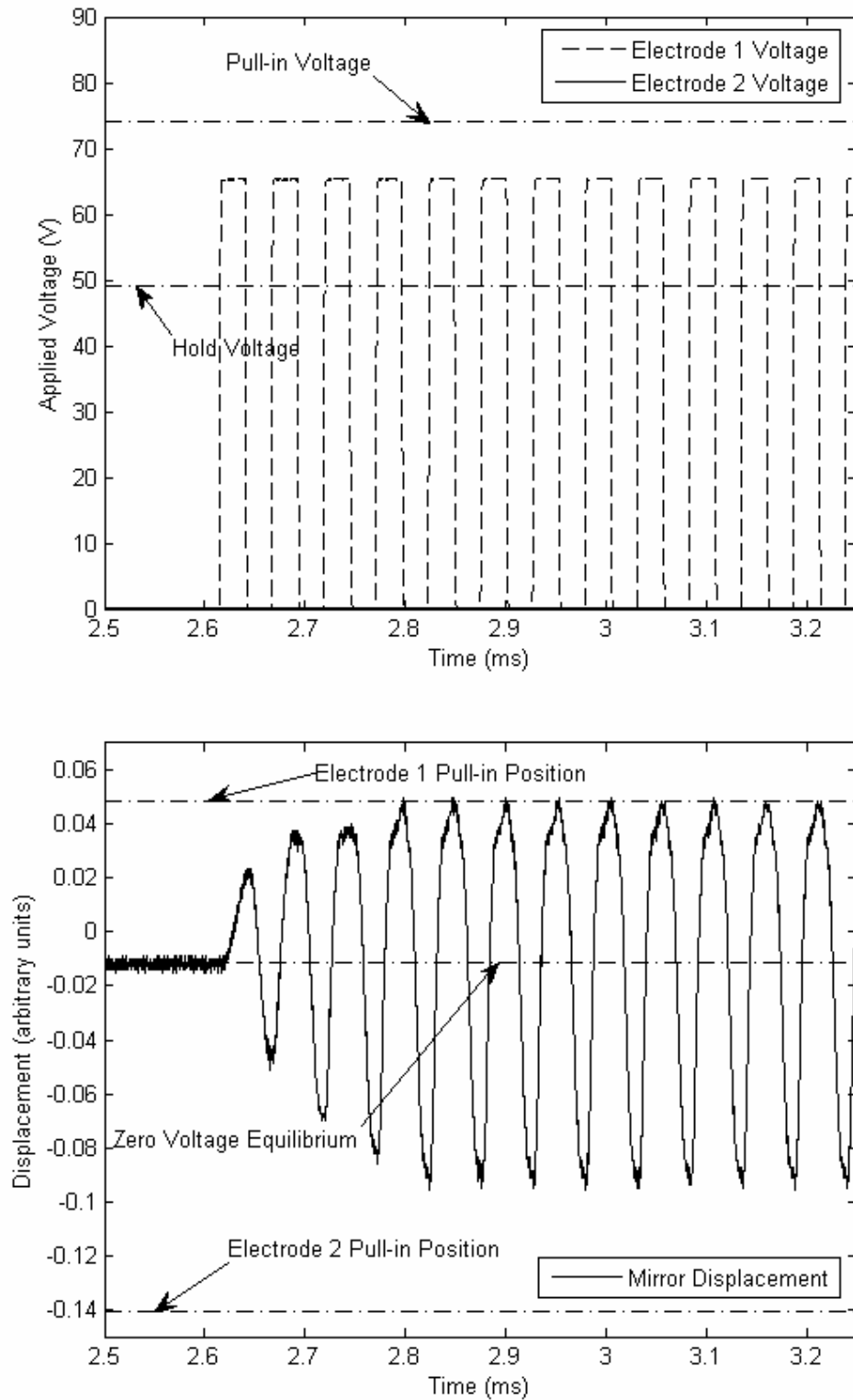
Figure 3.3 Plots showing the applied voltage and the resulting resonant pull-in of the structure.

Figure 3.2 shows the results of a test indicating successful dynamic switching. This is indicated by the ability to switch between pulled-in positions at a voltage lower than the pull-in voltage of the MEMS micromirror. To initialize the switch (intitially pull-in the device), we applied a voltage that exceeded the pull-in voltage (74 V for this device). Once pulled-in, we lowered the voltage to 53 V which was just above the hold voltage of 49 V and switched the 53 V bias between the two fixed electrodes. As seen in Figure 3.2, with this change in bias, the structure switched between the pulled-in positions defined by the fixed electrodes. The switching time for the device was 25 μs (0 to 100%). Note that a small delay was included between turning the voltage off of one of the fixed electrodes and turning it on the other fixed electrode. This delay was necessary for the switching to operate properly.

We also performed tests related to the resonant pull-in of the MEMS micromirror device. Figure 3.3 shows the results of these tests. The applied voltage was below the pull-in voltage yet after about the fourth cycle, the structure reached an amplitude that brought the micromirror into contact with the fixed electrode on the side that the voltage was applied to. Because of the constraints of the computer control of the applied voltage, it was difficult to move from a square wave to a constant voltage so it was not possible to catch the switch in its pulled-in state; however, had there been more flexibility in the applied voltage this would have been trivial to accomplish. The key thing that this test demonstrated was that the device performed as expected with the resonant pull-in technique. The voltage used in this test was 65 V. With higher quality factors (i.e. vacuum operation), this voltage is expected to go down dramatically.

4.0 Fast MEMS Micromirror Switching

Optical MEMS micromirrors have unique characteristics that make them appealing for such applications as telecommunications, projection displays, quantum computing, and wavefront correction. One performance characteristic that has limited the application of MEMS micromirrors is switching speed. Prior to this work, the switching speeds reported for MEMS micro-mirror devices have been in the range of a few microseconds to milliseconds [5-7].

As part of the high-speed switching project, we developed a high-speed MEMS micromirror device. This research was motivated by the need within Quantum computing for a chip with a large number of high-speed optical switches. These switches needed to switch faster than one microsecond and ideally would be competitive with acousto-optic modulators (i.e., switching speeds on the order of 100 ns). The devices we designed and tested switched between states in 225 ns and are therefore competitive with acousto-optic modulators but with the additional beneficial characteristics of micromirrors (e.g. cost, size, integration ability, low-power, etc.).

4.1 Design

The design of these MEMS micromirror devices was driven by high-speed switching. To achieve this goal, there were several important considerations. In general, the mechanical resonant frequency of a MEMS switching device is closely tied to the switching speed. This is especially true of MEMS switches using the dynamic switching approach. For a micromirror device that operates in a torsional mode, the resonant frequency is $\omega_0 = (k/I)^{1/2}$, where k is the stiffness of the torsional spring and I is the mass moment of inertia of the moving mirror plate. Therefore, to achieve high-speed switching requires that the mass moment of inertia be reduced while the stiffness is increased. Without any other changes, this leads to an increase in the operating voltage and higher stresses in the material. To alleviate these two issues, the gap between the plates was minimized at the cost of a smaller angular displacement between the switching states.

The micromirror plate is essentially a rectangular plate. The mass moment of inertia of a plate of this nature rotated about the axis defined by the torsional springs is

$$I = \frac{1}{12} mb^2 = \frac{1}{12} \rho thb^3 , \tag{4.1}$$

where m is the total mass of the plate , b is the long dimension of the plate orthogonal to the axis of rotation, h is the long dimension of plate parallel to the axis of rotation, t is the thickness of the plate, and ρ is the density of the material comprising the plate.

To minimize the mass moment of inertia of the plate requires either a change in one of the dimensions of the plate or changing the material, and thus the density, of the plate. Because of the cubic exponent on the b dimension, manipulating this term has the strongest effect, however, it is normally desirable for mirrors to have an aspect ratio close to one.

The thickness of the plate can be reduced only to the extent that deformations of the mirror surface don't exceed the planarity metric required for the application. This constraint brings into consideration the Young's modulus of the material forming the mirror plate. A material with a high modulus will deform less for a given thickness than a material with a low modulus.

Because of our constraint to use SUMMiT V™ for fabrication of the devices, the material was fixed as polysilicon. This also fixed the defined the thicknesses that could be used for the

micromirror plate (essentially the thicknesses of the different polysilicon layers or a combination of them).

The torsional stiffness is defined by the torsional springs that suspend the micromirror plate above the substrate. A simple torsional spring that is commonly used is just a fixed-fixed beam between the micromirror plate and the substrate. This beam operates in a twisting mode with a torsional stiffness of

$$k = \frac{G k_1 b_t h_t^3}{L_t},$$

(4.2)

Where G is the shear modulus, b_t is the long dimension of the rectangular cross-section of the beam, h_t is the short dimension of the rectangular cross-section of the beam, L_t is the length of the beam, and k_1 is a parameter dependent on the aspect ratio of the beam cross-section (b_t/h_t). Values for k_1 are given in Table 4.1.

**Table 4.1 k_1 parameters for a range of beam cross-section aspect ratios [REFERENCE].**

b/h	1	1.5	2	2.5	3	4
k_1	0.141	0.196	0.229	0.249	0.263	0.281

The shear modulus is related to Young's modulus, E, and the Poisson ratio, v.

$$G = \frac{E}{2(1+v)},$$

(4.3)

From Equation 3 it is apparent that there are three independent geometric parameters to vary in the design of the torsional spring as well as the shear modulus (which is varied by using different materials for the spring). In our design, the shear modulus is fixed by the SUMMiT V™ polysilicon. Also, the thickness of the spring (which could correspond to either b_t or h_t, depending on the final design) is constrained to the layer thicknesses of SUMMiT V™. This leaves just two parameters to freely vary in the torsional spring design, the spring length and the spring width. (It should be noted that there are two springs on each micromirror providing a total torsional stiffness twice that given by Equations 4.2). In the actual spring designs, the connecting points of the springs were rounded to reduce stress concentrations at those points. This resulted in an increased stiffness of the torsional springs above that predicted by Equation 4.2.

The requirements for these mirrors were to have a mirror surface of at least 20 μm × 20 μm and to have a switching speed of less than a microsecond. This means that, the resonant frequency needs to be approximately 500 kHz or higher (assuming that a switch operation requires the time of about one-half resonant cycle).
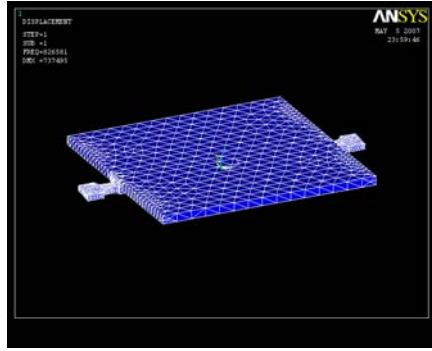
(A)
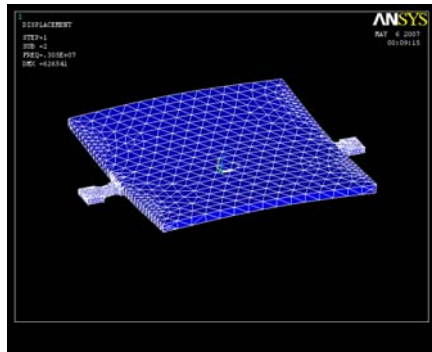
(B)
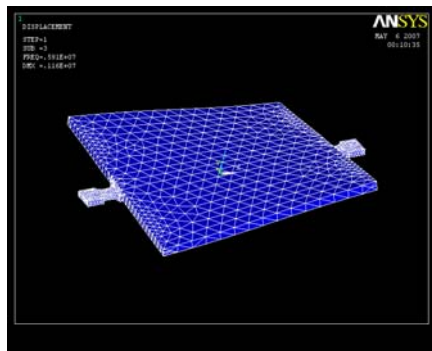
(C)

Figure 4.1 Three lowest frequency modes of the device #32. The frequency of the mode shown in A) is 830 kHz (torsional), B) is 3.1 MHz (bending), and C) is 5.9 MHz (twisting).

We designed a number of micromirror devices that use the poly1 and poly2 layers. In some instances the poly1 layer was used for the micromirror and poly2 was used as the torsional spring. In other instances, the usage was reversed. Table B.1 in Appendix B shows a complete listing of the different designs created. The resonant modes of the designs were evaluated to be certain that the lowest frequency mode was the torsional mode of the mirrors. Figure 4.1 shows the three lowest resonant modes of device #32. This mirror uses poly2 for the mirror surface and poly1 for the torsional spring. The mirror surface is 40 μm × 40 μm.
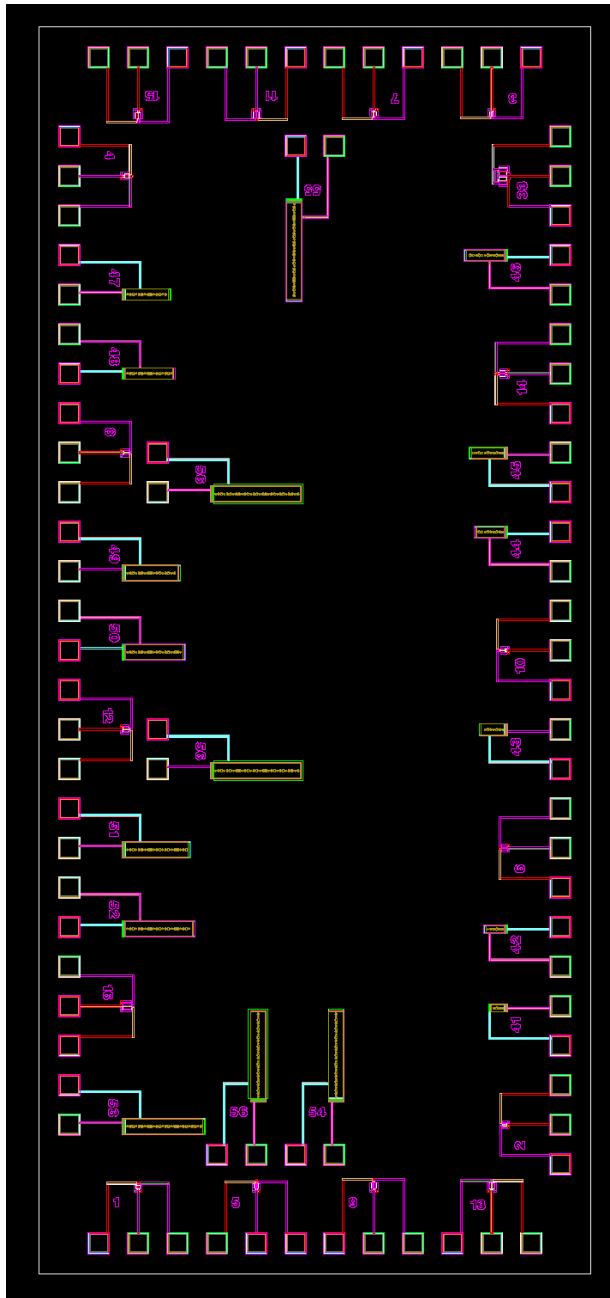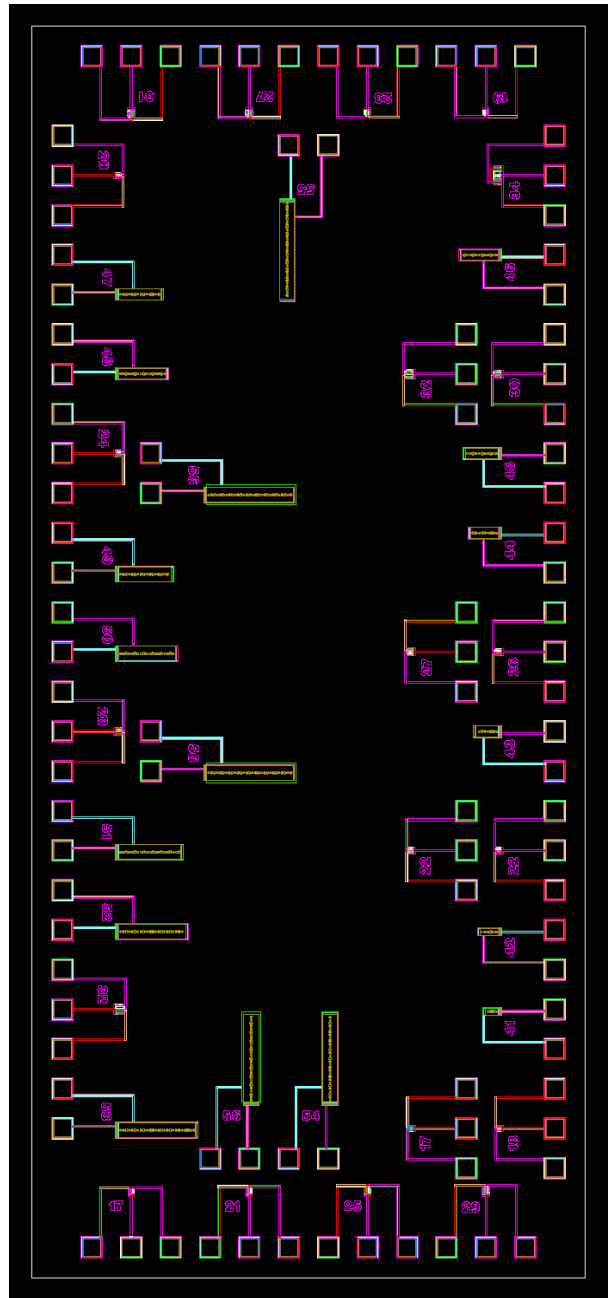
Figure 4.2 (A) Die layout for chip containing devices 1-16, and device 33 (along with other unrelated devices). (B) Die layout for the chip containing devices 17 through 32 and 34 (along with other unrelated devices.
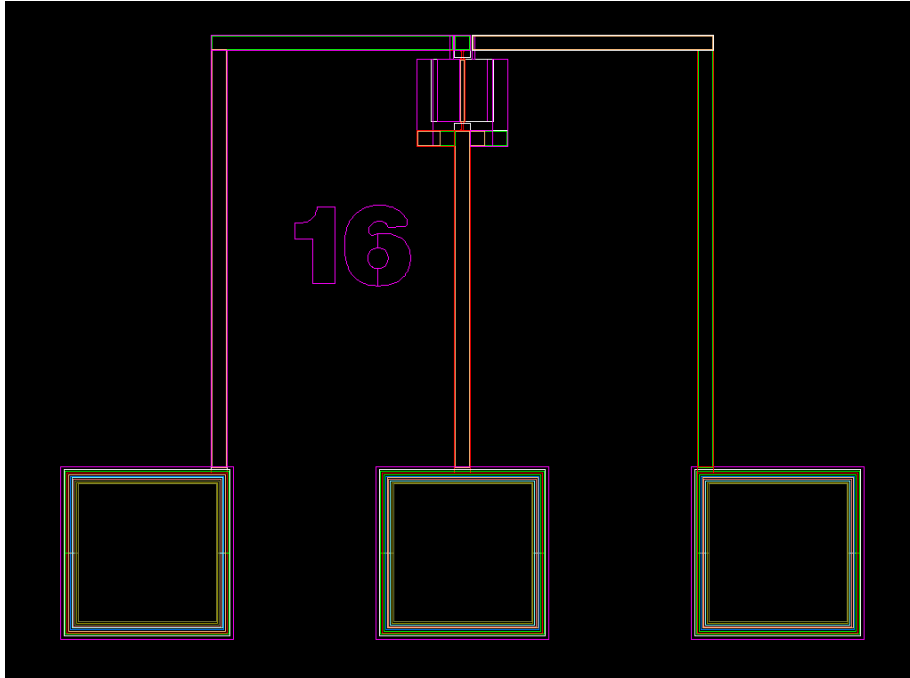
(A)
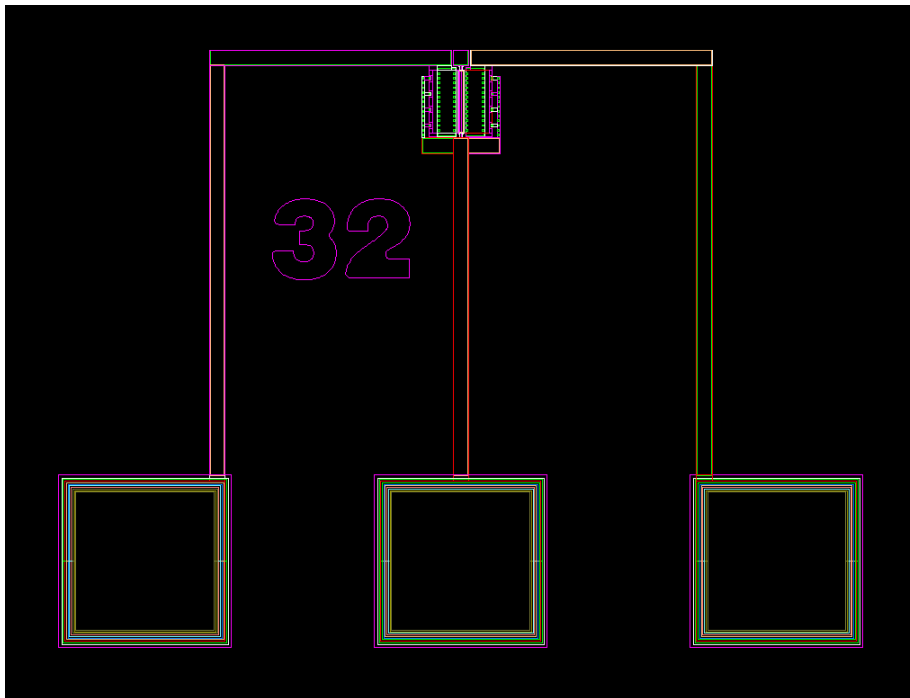
(B)

Figure 4.3 Example layouts of the two basic designs. A) utilizes the poly 1 layer for the mirror and the poly 2 layer for the torsional spring. B) uses the poly 1 layer for the torsional spring and the poly 2 layer for the mirror.
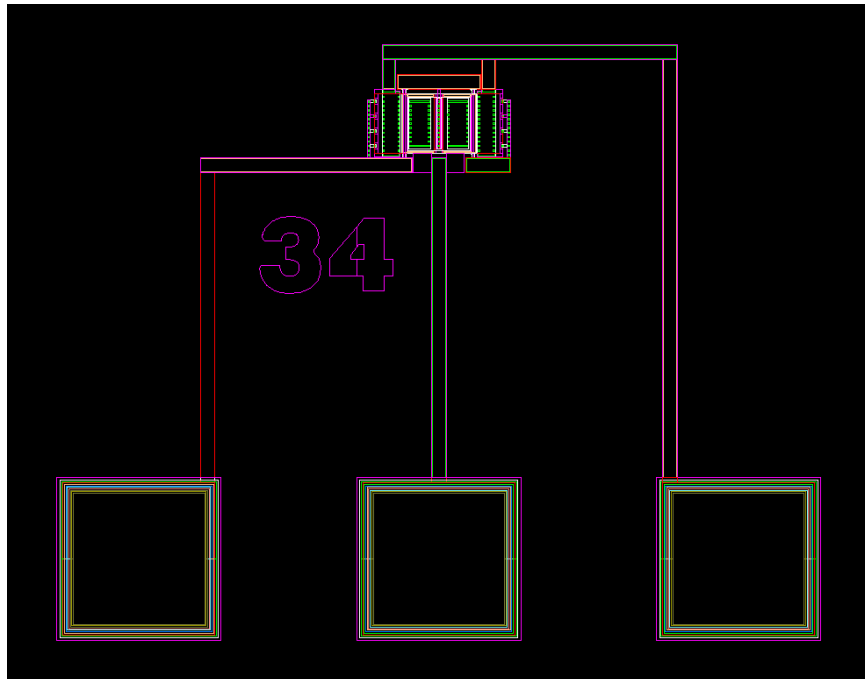
(A)
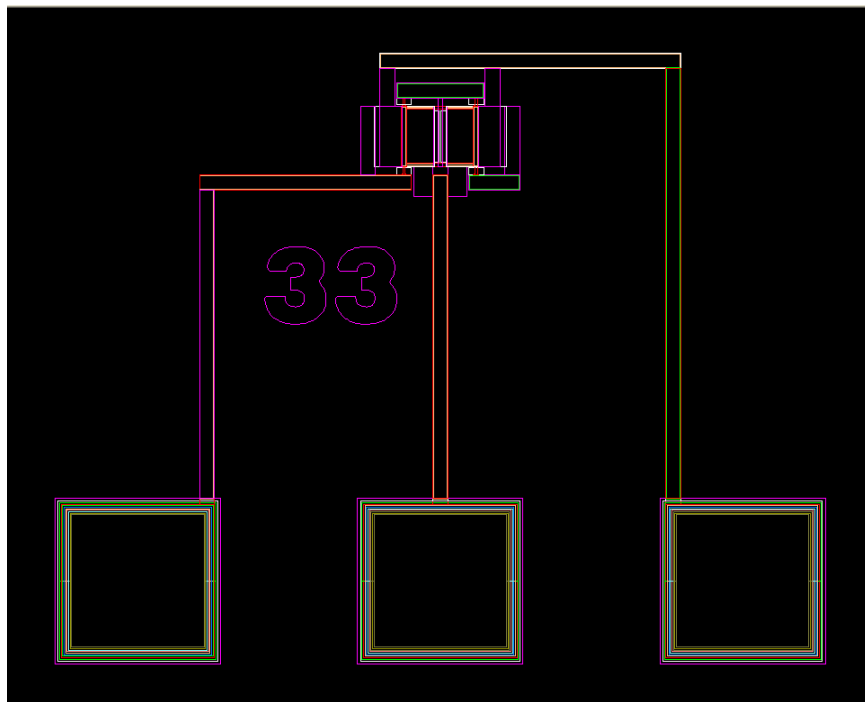
(B)

Figure 4.4 Combined mirror designs for achieving very high stiffness. A) combines two mirrors where the poly 1 layer is used for the torsional spring and poly 2 is used for the mirror structure. B) combines two mirrors where the poly 1 layer is used for the mirror structure and the poly 2 layer is used to create the torsional spring.

For device #32, the predicted resonant frequency indicates a switching time of 602 ns. This is a conservative estimate because the electrostatic forces driving the switching will, even with the dynamic operation, reduce the time required for switching below one-half the time for a resonant cycle. The range of devices included designs that had mirrors sized as small as 20 μm × 20 μm. Some of these devices had torsional resonant frequencies as high as 3.6 MHz, corresponding to a (conservative) switching time estimate of 140 ns. The smaller mirror sizes of these higher speed devices results in a smaller actuator area and therefore higher pull-in and hold voltages.

Figure 4.2 shows the die layout of the two modules containing the different device designs. There are two basic designs. One design uses the Poly1 layer as the mirror surface and the Poly2 layer as the torsional spring. The other design reverses the usage of those layers. Example layouts of each of those two basic designs are illustrated in Figure 4.3.

The constraints on the metallization in SUMMiT VTM would not permit the application of aluminum to the Poly1 or Poly2 layers. We did design some metallized structures to evaluate the roughness and curvature of the surface resulting from the metal deposition but this required that we build up the mirror surface with the higher poly layers. These designs are included in the die layout and are numbered according to the design that they were built up on.

One of the challenges in designing these mirrors was achieving a high torsional stiffness. To address this, two designs were created where two mirrors were connected with bending tethers to provide a "folding" style operation. This allows for a total stiffness resulting from the four torsional springs holding the two connected mirrors as well as the folding tethers connecting the two mirrors. The layouts for these designs are shown in Figure 4.4.

4.2 Fabrication Results

The MEMS micromirror device was fabricated with Sandia National Laboratories' SUMMiT V[TM] MEMS fabrication process [8]. The SUMMiT V[TM] process uses polysilicon for the structural material and silicon oxide as the sacrificial material. There are five distinct layers of polysilicon in the process. Chemical mechanical polishing (CMP) is utilized to smooth the silicon oxide layers prior to the deposition of the polysilicon layers. Owing to the fact that this is a standard process at Sandia National Laboratories, the devices resulting from the fabrication process were impressive.

Figure 4.5 shows SEM images of a typical device #32. The micromirror plate portion of the structure is formed out of the third polysilicon layer (Poly2) and is 40 μm by 40 μm by 1.5 μm thick. The torsional springs on either side of the plate are formed from the second polysilicon layer (Poly1) and are 1.0 μm thick, 3 μm long, and 2 μm wide. The fixed electrodes located underneath the micromirror plate for electrostatic actuation are formed by laminating the first and second polysilicon layers together (Poly0 and Poly1). The gap between the fixed electrodes and the torsional plate is 0.3 μm. The overlap area between each fixed electrode and the torsional plate is 480 μm^2. Mechanical stops are employed to keep the plate from coming into contact with the fixed electrodes. The mechanical stops are also comprised of the first and second polysilicon layers laminated together but are electrically isolated from the fixed electrodes.

Figure 4.6 shows SEM images of device 16. The micromirror plate for this device is also 40 μm by 40 μm but since it is comprised of the poly1 plate it is only one micron thick. Note that the torsional spring is on the top of the plate and is composed of the poly 2 layer. The gap between the torsional plate and the fixed electrodes is 0.5 μm.
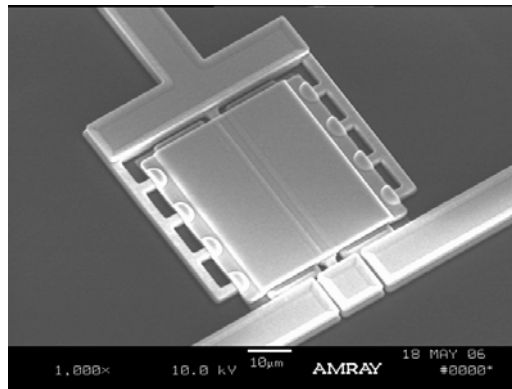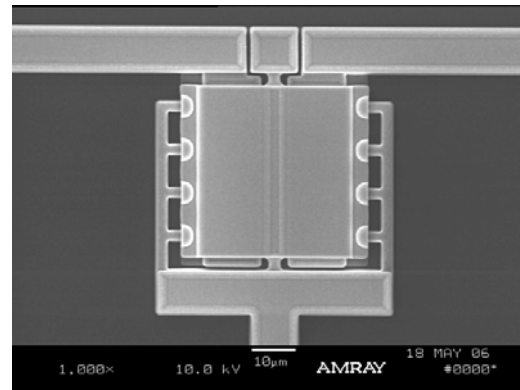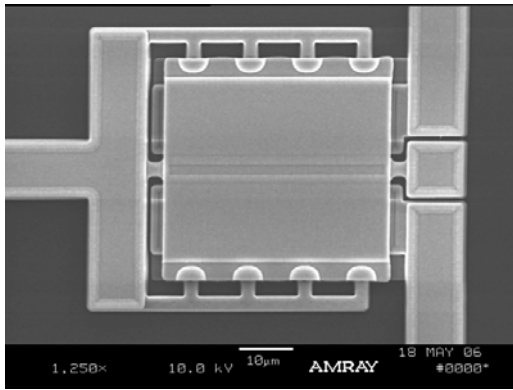
Figure 4.5 SEM images of device 32. The mirror structure is 40 μm × 40 μm.
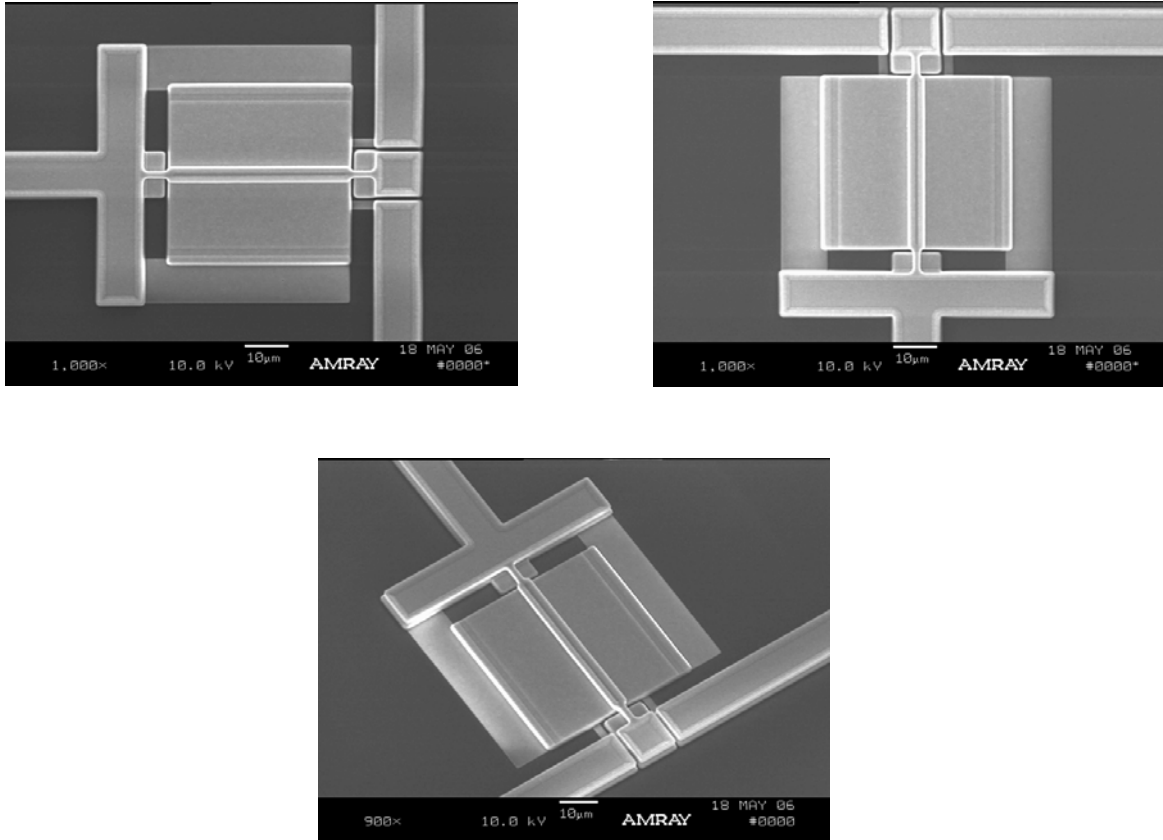
Figure 4.6 SEM images of micromirror device 16. The micromirror plate is 40 μm by 40 μm.
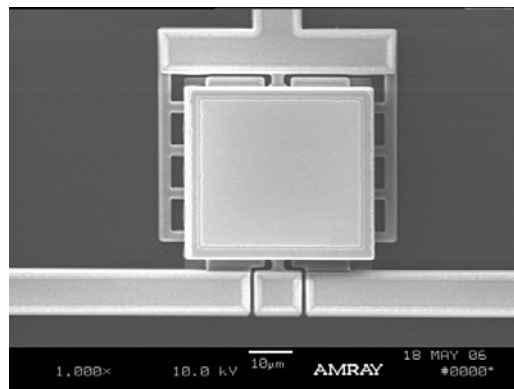
Figure 4.7 SEM image of device 32 with built up poly layers and metallization layer.

Figures 4.7 shows an SEM image of a device that has additional poly layers built up on the mirror which allows the metallization layer for a better mirror surface. We analyzed the surface quality of the metallized mirror using a white-light interferometetry based profilometer. Figure 4.8 shows the results from that profilometer measurement. The RMS roughness of the aluminum surface was under 5 nm. The surface of the micromirror had some curvature. This is likely due to

the tensile residual stress of the aluminum film. The radius of curvature of the mirror was measured to be about 8 mm.
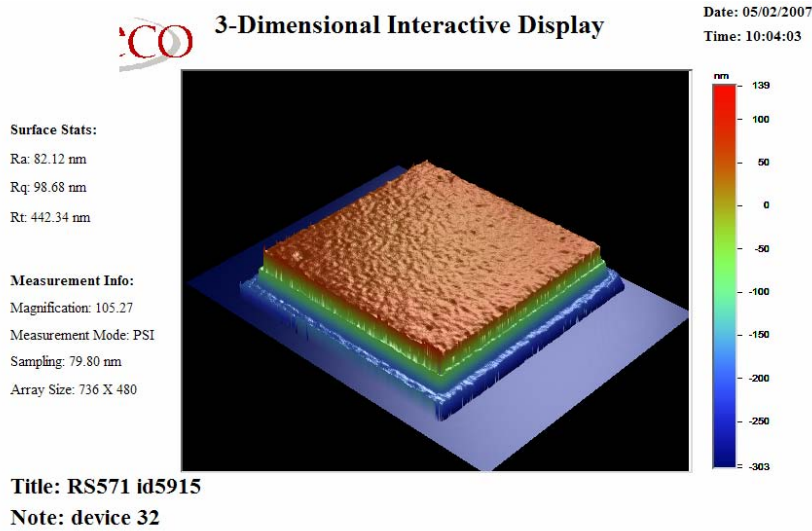
Figure 4.8 Veeco white-light interferometry based profilometer measurement of the surface of the metallized mirrors.

Figure 4.9 shows the fabricated results for the micromirror designs that combined two mirror devices together in a folding mechanism to allow increased stiffness. The fabrication results of both designs appeared to be quite good.

(A)

(B)
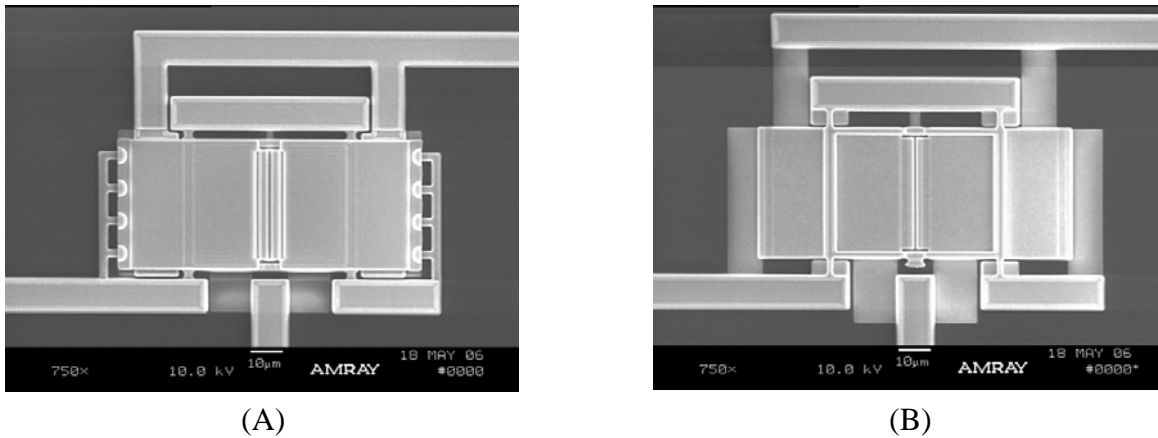
Figure 4.9 SEM images of the two mirror designs that combined two mirrors in a folding style operating to allow for increased stiffness. A) uses the Poly2 layer for the mirror structure and B) uses the Poly1 layer for the mirror surface.

4.3 Switching Results

The switches were tested in a series of experiments to characterize their behavior. The first tests performed were quasistatic tests where the applied voltage was ramped up slowly and measurements were made of the angle of the mirror surface. These tests were conducted for all 32 single mirror designs. The results of these tests are summarized in Table 4.2 with plots of all the data in Appendix C. In places where the data did not follow the traditional pull-in behavior,

an "NA" was placed in the table. This result indicates that either the design of the structure did not perform in the traditional manner (many of the aggressive designs fell into this category) or the structure itself was damaged somehow. The angle of the mirrors was determined using interferometry.

Table 4.2 Quasistatic test results for micromirror devices. NA indicates a value was not obtained.

Device #	State #1 V_{pi}	State #1 V_h	State #1 Angle	State #2 V_{pi}	State #2 V_h	State #2 Angle
1	NA	NA	NA	NA	NA	NA
2	NA	NA	NA	NA	NA	NA
3	NA	NA	NA	NA	NA	NA
4	75	NA	NA	75	60	-1.95°
5	62	52	2.15°	60	48	-2.23°
6	90	NA	1.66°	75	NA	-1.78°
7	45	NA	1.89°	45	NA	-1.94°
8	NA	NA	NA	NA	NA	NA
9	42	38	1.78°	44	40	-2.01°
10	48	34	1.72°	50	38	-1.72°
11	44	20	1.55°	NA	NA	NA
12	52	38	1.43°	52	38	-1.60°
13	32	20	1.49°	36	22	-1.72°
14	34	NA	1.43°	44	18	-1.49°
15	30	NA	1.60°	52	NA	-1.49°
16	38	22	1.09°	28	22	-1.26°
17	68	62	1.26°	66	62	-1.43°
18	NA	NA	NA	NA	NA	NA
19	58	52	1.49°	NA	NA	NA
20	50	34	-1.26°	48	26	-1.26°
21	34	34	1.38°	34	30	-1.38°
22	50	40	1.26°	44	34	-1.03°
23	48	42	1.14°	54	48	-1.09°
24	32	28	1.03°	36	28	-1.20°
25	30	18	1.15°	NA	NA	NA

26	NA	NA	NA	28	14	-1.15°
27	40	28	0.92°	32	30	-0.097°
28	40	24	0.97°	32	22	-0.92°
29	28	32	0.97°	38	18	-0.92°
30	NA	NA	NA	NA	NA	NA
31	20	16	0.97°	18	24	-0.92°
32	24	16	0.86°	NA	NA	NA

We tested the metallized mirrors to show that they also are operational. Figure 4.10 shows the results of one of those tests. The total displacement of the edge of the micromirror is approximately 0.6 μm. The total reflection angle change between states is just under 2°.
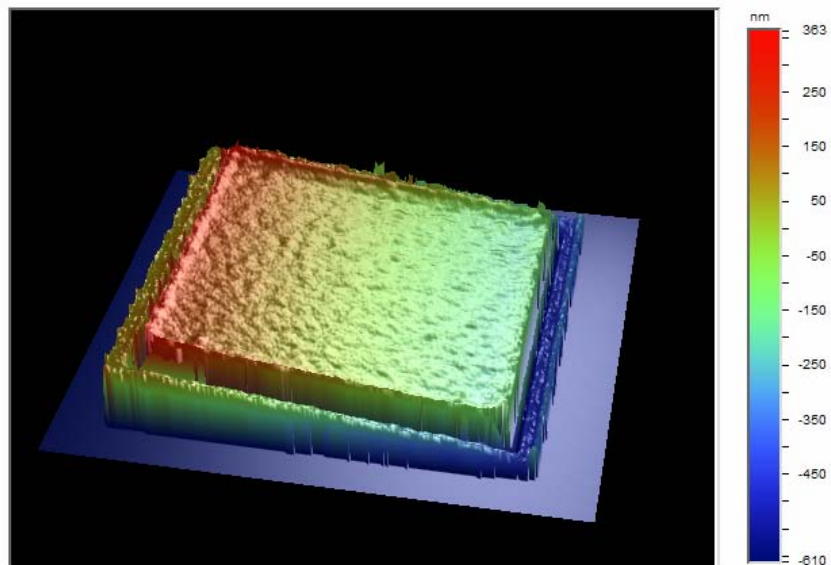
Figure 4.10 showing an actuated micromirror (device 32) with metallization.

The switching tests exploring switching speed and dynamic switching used device 32. Device 32 had the largest overlap area of the electrodes combined with the smallest gap. This made the capacitance changes associated with device 32 the largest and thus allowed the best chance for the control circuitry to perform well.

The switching speed and dynamic switching tests were performed in a vacuum chamber. Under quasistatic conditions the mirror tested had a pull-in voltage of 19.7 V and a hold voltage of 14.5 V. The resonant frequency was found to be 750 kHz. Figure 4.11 (A) shows the test setup used for characterizing the performance of the micromirror switch. The two inputs to the PCB are the bias voltage from the voltage source and the switch control signal from the waveform generator. The switch control signal controls a transistor that switches the voltage applied to the micromirror from the bias voltage to ground. One of the fixed electrodes is always held at ground and the other is always held at the bias voltage. Depending on the voltage applied to the
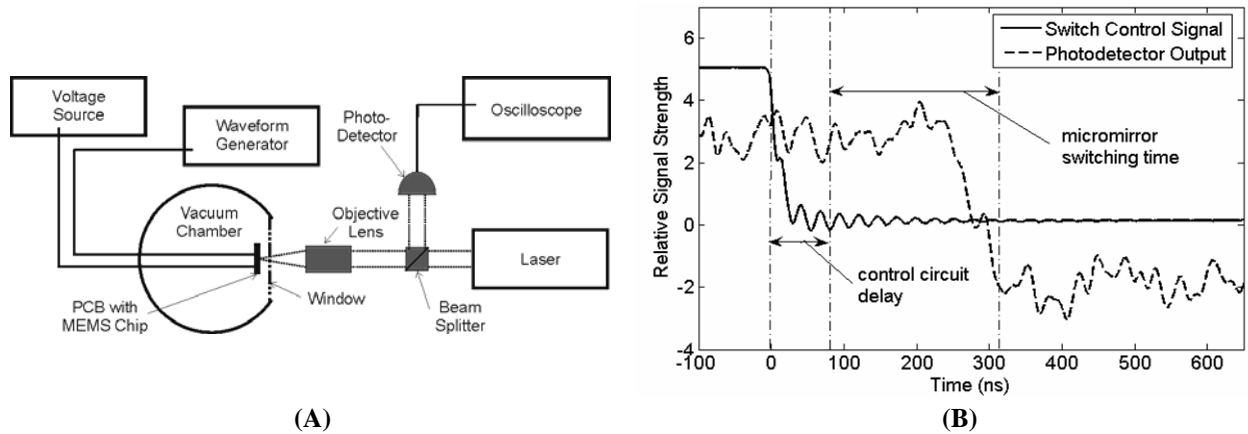
Figure 4.11 (A) is a schematic representation of the test set-up. (B) shows the results of the micromirror switch testing. Total switching time is 310 ns. 85 ns is due to the control circuit delay, indicating that the MEMS micromirror switches in 225 ns. The bias voltage applied for these tests was 22 V.

micromirror, the micromirror will be pulled-in to one or the other of the fixed electrodes. The high-voltage transistor controlling the bias voltage has an 85 ns delay time. The vacuum chamber was held at 1.5×10^{-5} torr during testing.

By switching between pulled-in states, the device avoids long settling times for mechanical vibrations that are typically observed with MEMS micromirrors when they are not mechanically held in place.

The switch test results are given in Figure 4.11 (B). The switching time for the micromirror device was 225 ns. The bias voltage used for the switching tests was 22 V. During testing, the switch was operated at repetition rates of up to 100 kHz. The device exhibited no failure over hundreds of millions of cycles.

Dynamic switching was also evaluated with this device. The first effort was directed toward the demonstration of the dynamic pull-in effect with the MEMS mirror devices. Resonant pull-in converts electrostatic energy into mechanical energy, which is stored in the mechanical resonance of the structure. A certain amount of energy is required to achieve pull-in. By building up mechanical energy over a number of cycles, the voltage required for pull-in is reduced.

Resonant pull-in was achieved by driving the device at resonance using the positive feedback oscillator circuit shown in Figure 4.12. A DC bias voltage (which must exceed the hold voltage to achieve pull-in) is applied to the device, causing the mirror to deflect due to voltage changes at the amplifier output. Dynamic mirror deflections produce a time varying current at the input of the oscillator sustaining amplifier due to the change in capacitance between the mirror and the electrode, completing the positive feedback loop. When the resonance achieves sufficiently high amplitude such that the structure comes very near to making contact, the structure will be pulled in and held in place by the DC bias voltage. Resonance allows for switching at voltages much less than the quasi-static pull-in voltage.
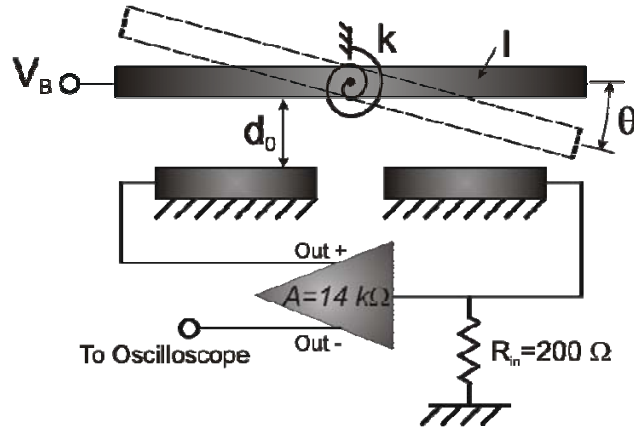
Figure 4.12 Resonant pull-in oscillator schematic.

The hold voltage is the minimum voltage required to hold the switch once it is pulled in and sets the lower limit on the bias voltage required to achieve resonant pull-in. Once the device is initially pulled in using resonant techniques, switching can be achieved using a voltage slightly above the hold voltage. Thus the voltage required for the initial pull-in sets the maximum voltage required for the switch. High quality factors are required for the resonant pull-in voltage to approach the hold voltage. A low quality factor indicates that the mechanical structure is less efficient at storing energy in resonance, thus requiring a higher actuation voltage.

Figure 4.13 shows a schematic diagram of how the voltages were applied to the structure for network analyzer testing. Figure 4.14 is the fundamental resonant peak (751 kHz) of the device at a bias voltage of 12.5 V and RF power of -50 dBm. The quality factor is 3000 under a 40 mTorr vacuum.

Figure 4.15 shows three output waveforms from the oscillator circuit with increasing bias voltage. With the mirror bias voltage very close to the hold voltage large non-linearities are present, indicating resonant pull-in is about to occur. When the structure pulls in, the oscillator circuit output waveform becomes flat.
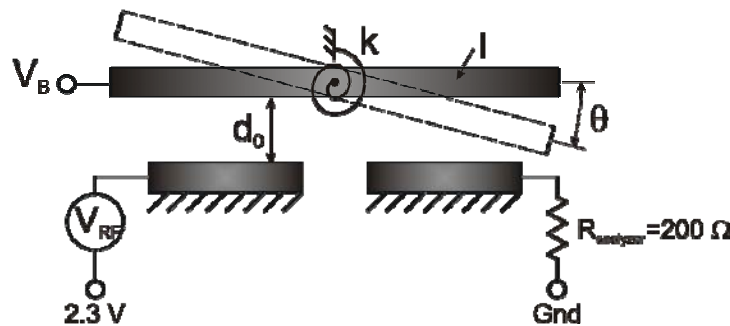
Figure 4.13 Schematic drawing indicating the voltages applied to the torsional MEMS device during network analyzer testing. A 2.3 V DC bias voltage is applied to one of the electrodes to mimic the DC offset of the amplifier in Figure 4.12, providing consistent pull-in and hold voltage measurements between the two test techniques.
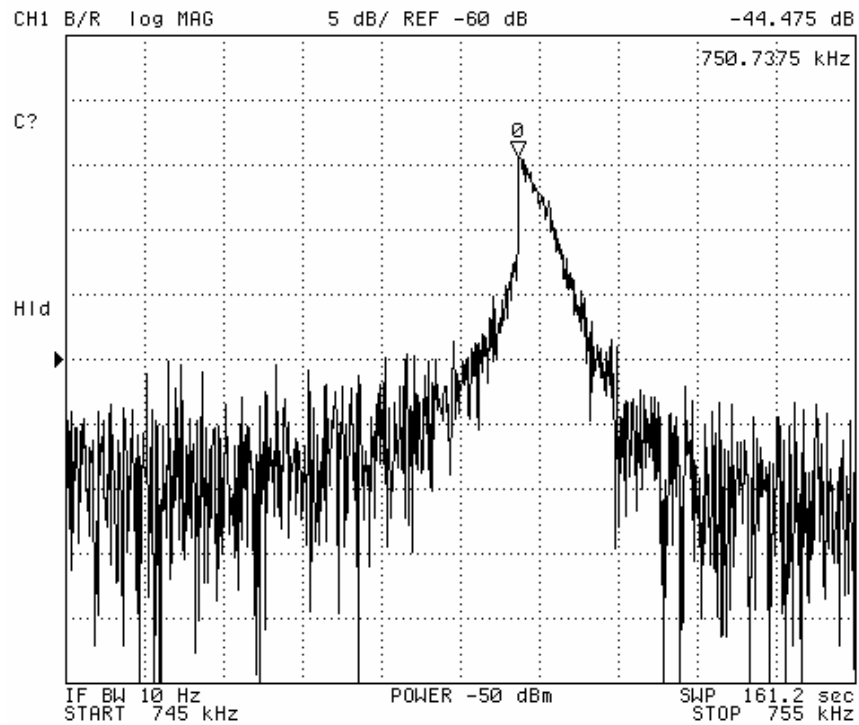
Figure 4.14 Typical resonant peak observed during the testing and characterization of the torsional MEMS device. The device was in a 40 mTorr atmosphere with an applied bias of 12.5 V and -50 dBm RF power. The resonant peak was at 750.7375 kHz with a quality factor of 3000.
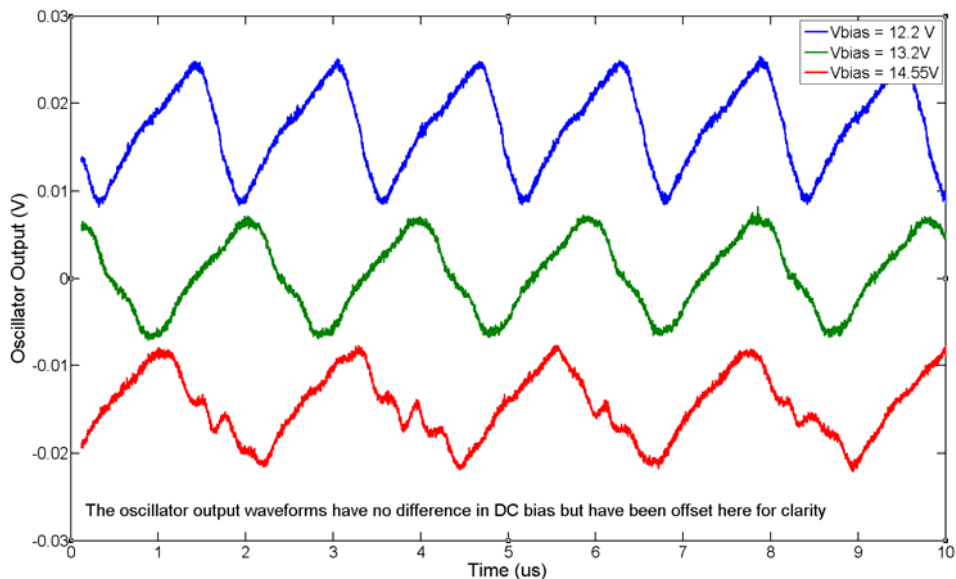
Figure 4.15 Comparison of the waveforms resulting from the oscillator circuit driving the resonance of the torsional MEMS device. Note that with increasing bias, the period of the waveform is increasing. Also, at the bias of 14.55 V (just prior to achieving resonant pull-in) the waveform is beginning to show some higher frequency information. Upon achieving resonant pull-in, the output waveform becomes flat (not shown).

35
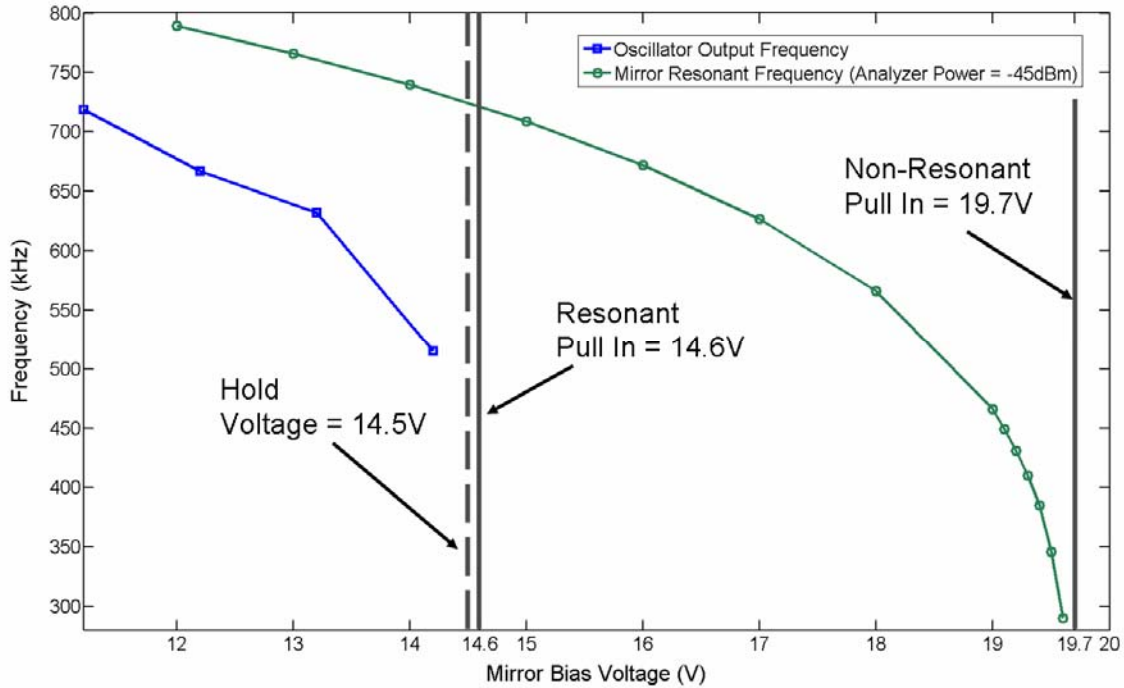
Figure 4.16 Plot showing the effect of the bias voltage on the resonant frequency of the MEMS device. Also shown is the non-resonant and resonant pull-in voltages. The resonant pull-in voltage represents more than a 25% reduction in the voltage required to achieve pull-in. The resonant pull-in voltage is achieved at a voltage that is just 100 mV above the hold voltage.

Figure 4.16 shows the change in resonant frequency (both oscillator and network analyzer outputs) that results from increasing the applied DC bias to the structure. The quasi-static pull-in and hold voltages were found using a network analyzer to determine what state the structure was in (i.e. pulled-in or free to resonate). Resonant pull-in was achieved using the oscillator circuit at 14.6 V, while the standard quasi-static pull-in voltage was found to be 19.7 V. The hold voltage was measured to be 14.5 V using both the oscillator circuit and network analyzer. With resonant pull-in, we demonstrated pull-in at a voltage that was more than 25% less than the standard pull-in voltage and only 100 mV above the hold voltage.

Dynamic switching between the pulled-in states was attempted with the switching circuit described earlier where one fixed electrode was set at ground and the second was set at a bias voltage and the torsional mirror electrode was switched between the ground and the bias voltage. With this arrangement, dynamic switching between the pulled-in states was not achieved at voltages below the quasi-static pull-in voltage. This was likely due to the moving electrode bouncing away from the pulled-in state after coming into contact with the mechanical stops. Because the hold voltage was only 25% less than the pull-in voltage and because the voltage switching occurred immediately, the moving electrode actually came into contact with the mechanical stops at a high velocity leading to a significant bounce. The solution to this is to provide a delay in switching between voltages so that the moving electrode did not accelerate beyond that provided by the forces from the springs. However, the switch circuit developed did not provide such a delay and therefore switching at less than the pull-in voltage was not achieved with this device. A redesign of the switching circuit allowing for a delay is anticipated to solve this problem. However, while this would lead to a 25% decrease in the voltage, it would also

slow the switch down by almost a factor of three. This does not seem like a worthwhile design trade-off.

4.5 Discussion

The results of the micromirror device design and testing indicate an order of magnitude improvement in switching speed compared with any other MEMS micromirror device. This improvement in switching speed opens many new possibilities for micromirror applications. These applications include ion-trap based quantum computing, telecommunications, high-resolution scanning micromirror projection displays, and many other applications that currently use acousto-optic modulators [9].

Further improvements in switching speed can be realized by decreasing the size of the mirror (micromirrors with dimensions as small as 10 μm × 10 μm have been shown to be useful [5]). This should reduce switching speeds further with the possibility of reaching sub 100 ns switching times with a micromirror device.

The dynamic switching concepts were demonstrated to a limited extent. Resonant pull-in was achieved while dynamic switching between pulled-in states was not demonstrated. The torsional structure did not allow a significant reduction in the actuation voltage. The torsional structure does not come into intimate contact with the fixed electrode which limits the hold voltage to a significant fraction of the pull-in voltage. Therefore, the dynamic switching techniques do not provide a significant benefit. (It is likely to be more desirable to design the structure with a more compliant torsional spring to achieve a lower actuation voltage if that is the design objective.)

If the fixed electrodes can be designed so that they are slanted (or effectively slanted by a stepped edge) according to the angle achieved at pull-in by the moving electrode, the hold voltage can be reduced to the point where dynamic switching techniques may make sense to utilize.

(A)   (B)
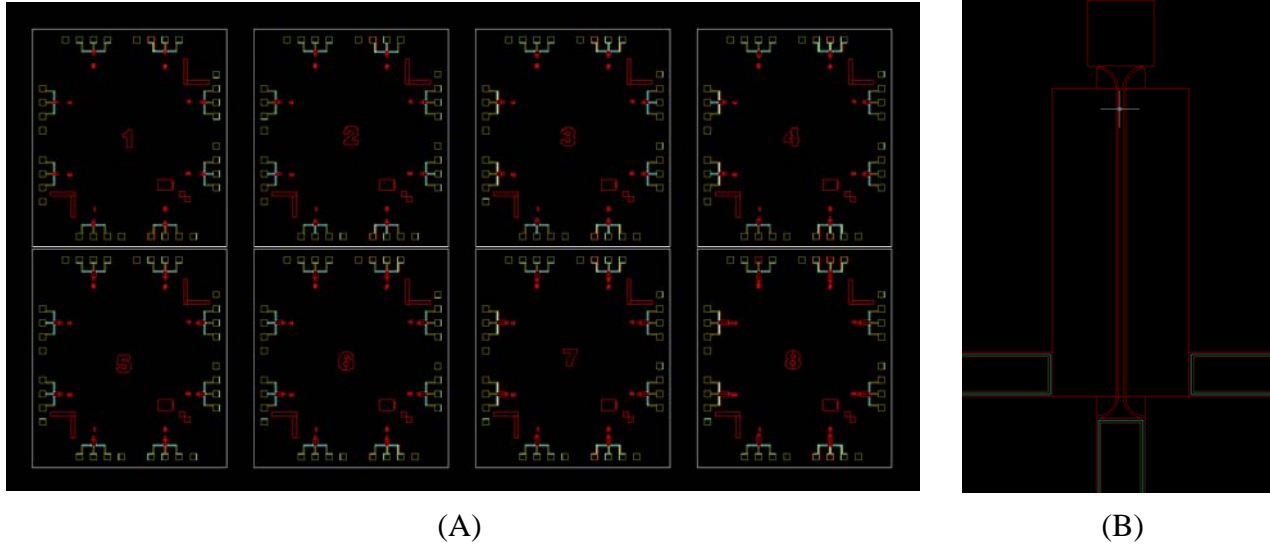
Figure 5.1 Mask layout for the MEMS structure design. (A) shows the entire reticle. (B) shows device 7 from die 8.

5.0 Integrated Optical MEMS Switching

Combining MEMS with integrated optics to create optical switching devices have the potential to create very high speed switching structures. The high speed switching potential comes from the fact that less mass is required to move for an integrated optical switch than for a free-space optical switch based on a micromirror structure. In addition, if evanescent coupling is used as the switching mechanism, only a relatively small displacement is required to switch the light from one waveguide to other. This small displacement further adds to the high-speed switching potential of the device. Furthermore, the evanescent coupling based switching provides a mechanism that can, in theory, provide for 100% switching of the light. The more common approach of using end-coupling will always have losses due to the change in index experienced by the light. Dynamic switching can also be used to further lower the voltage and/or increase the switching speed of the devices.

5.1 Design

The approach taken in developing the MEMS waveguide switch device was to develop the optics and the MEMS structure separately. When sufficiently developed, the MEMS structure was integrated with the waveguides to demonstrate the full switching structure.

The MEMS structure was designed in a single polysilicon layer where all of the switching structures, the two fixed electrodes and the single moving electrode, were all created within the single layer. The moving electrode was designed as a fixed-fixed beam. The sacrificial layer was silicon oxide with the release being accomplished by a timed HF etch. This allowed for a simple MEMS structure that provides relatively simple fabrication of the MEMS device.

The layout for the MEMS switch structure is shown in Figure 5.1. Note the fixed-fixed beam width is much less than the width of any other structure. This significant difference in width allows a fairly straightforward timed etch release. The one complicated portion of the process was the electrical isolation of the MEMS structure. This was accomplished by releasing the structure with a timed release, coating the structure with silicon nitride, refilling the structure with PSG (phosphorus doped silicon oxide) to allow the metallization to be completed followed by a final release of the device. A full listing of the different device designs is in Appendix D.

Some of the devices were isolated electrically using high-permittivity dielectric materials. These materials allow a lower hold voltage for the same thickness material and therefore can be significant for dynamic switching. These devices are described in Section 6.

5.2 MEMS Fabrication

The fabrication process flow is shown in Figure 5.2. The most significant challenge encountered during fabrication was the CMP of the PSG to allow for metallization to be accomplished. The PSG was rapidly removed during the CMP resulting in thinning of the silicon nitride layer. This did not cause a significant problem because the electrical isolation needed to be on the sidewalls of the moving and fixed electrodes while the top silicon nitride was not critical.

Silicon oxide is deposited to create the sacrificial layer. The 2.25μm poly-silicon structural layer is then deposited.

The poly-silicon structural layer is patterned and etched with photolithography and reactive ion etching.

Poly-silicon doubly fixed beams are released with a timed HF etch.

60nm of Silicon nitride is conformally deposited to create the dielectric layer for electrical isolation.
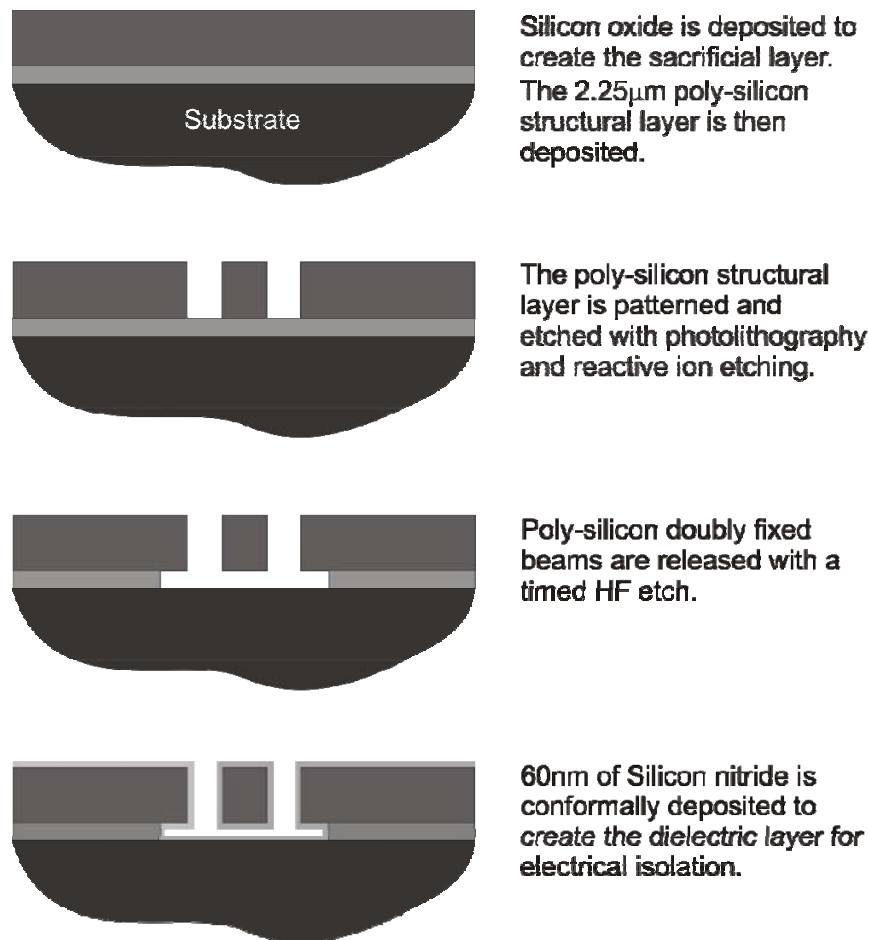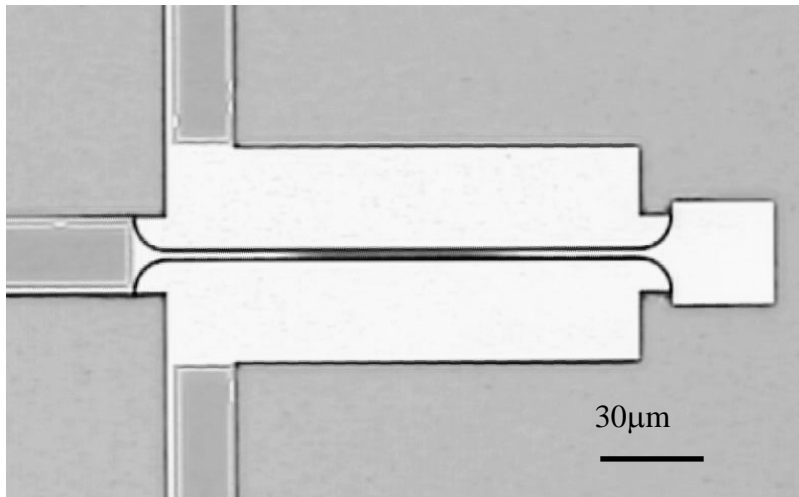
**Figure 5.2 fabrication process flow for the MEMS switching device.**

Figure 5.3 Typical switching structure showing the effect of the CMP on the silicon nitride layer of the device (the darkened region of the center movable electrode is a residual portion of the silicon nitride film).

Figure 5.3 shows a typical device resulting from the fabrication of the device. The fabrication results were quite good resulting in a high yield of functional devices.

5.3 MEMS Testing

The devices were tested according to the schematic shown in Figure 5.4. The devices are simple mechanical switches and there do not have any active electrical or optical contacts with which to get a strong switching signal from. To monitor the switching, we tightly focused light onto the switching structure and monitored the intensity of the reflected light. The intensity of reflected light was modulated slightly by the movement of the beam allowing us to monitor the switching.
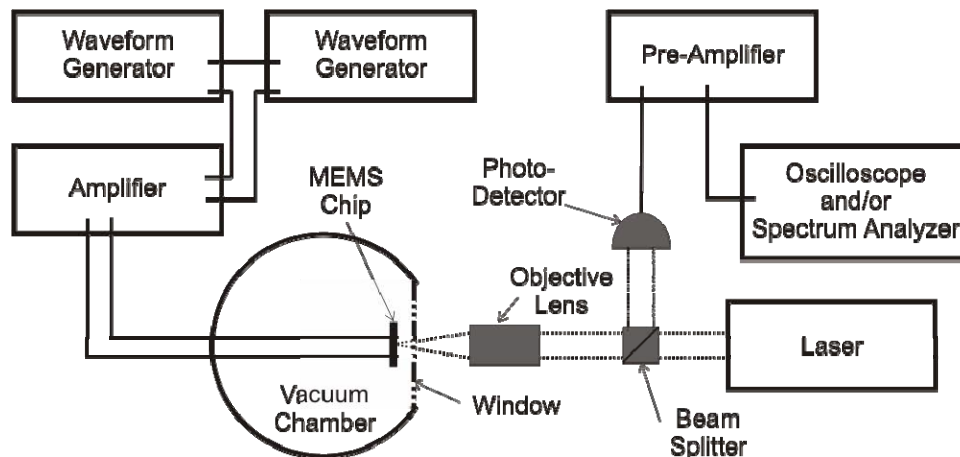
Figure 5.4 Test set-up for the MEMS strain-energy switching structure. The position of the movable beam is sensed by focusing light onto the beam and measuring the reflected light with a photodetector. The intensity of the reflected light is dependent on the position of the beam. The two arbitrary waveform generators are synchronized to achieve the necessary timing for the switch signals. The device is tested in a vacuum chamber to improve the mechanical Q and avoid dielectric charging.

41

(A)

(B)
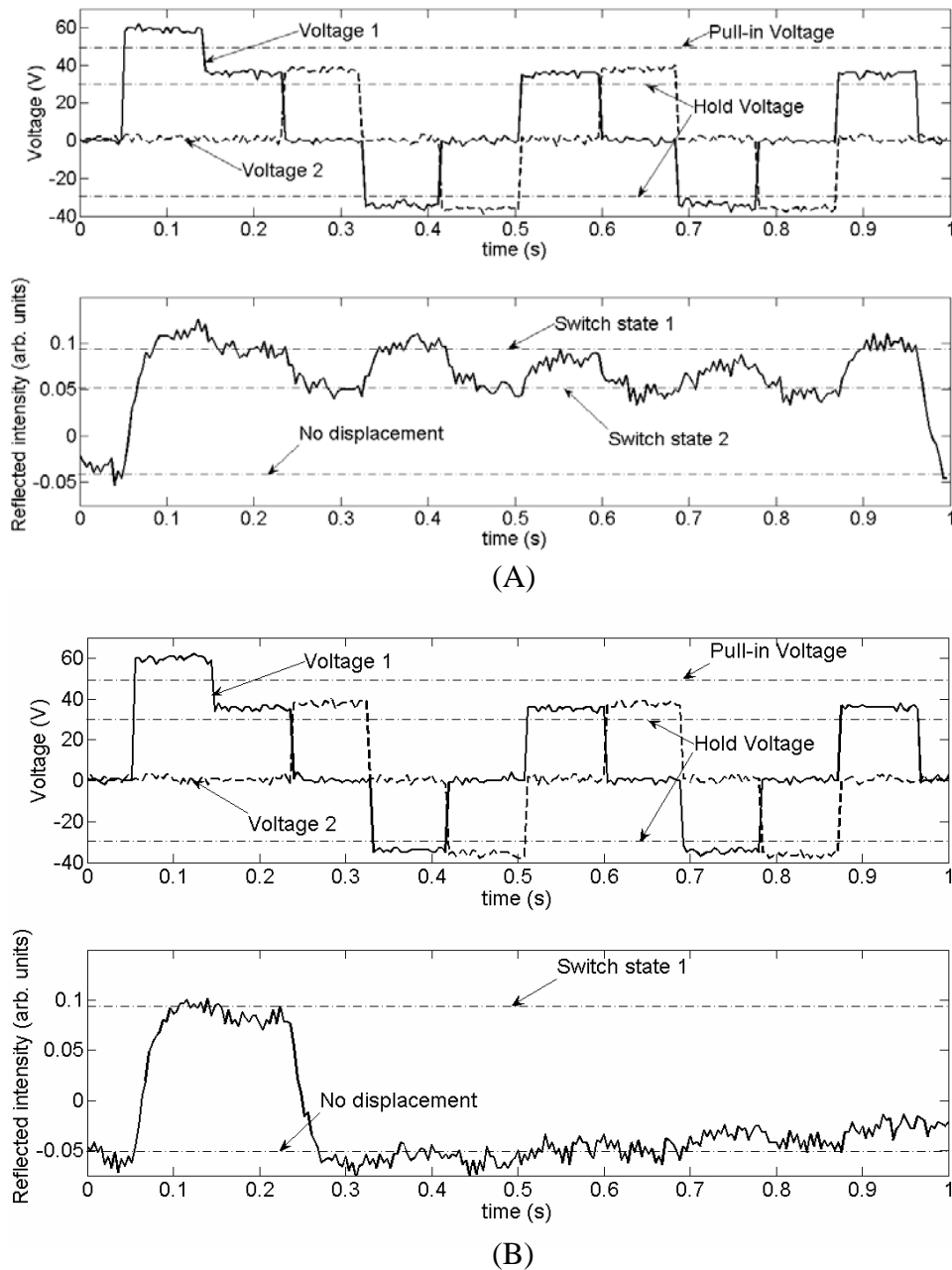
Figure 5.5 Input voltage signals with the resulting reflected optical intensity from the device. (A) demonstrates the strain-energy switching method allowing switching from one pulled-in state to the other with voltages below the pull-in voltage. In (B) the timing of the two voltage signals is slightly offset, causing the device to not operate according to the strain-energy switching method. In both (A) and (B) an initial voltage is shown that is higher than the pull-in voltage. This is to initially pull-in the structure to "initialize" it for operation according to the strain-energy switching technique. Note that the reflected optical intensity data presented here was low-pass filtered to remove high frequency noise. Thus, the switching times that these plots seem to indicate are not the actual switching speeds.

The test results are given in Figure 5.5. The signal-to-noise ratio resulting from this test set-up was very weak. To clarify the signal, the output was low-pass filtered. The low-pass filtering caused the signal to not represent well the switching speed. In other tests, the switching speed was found to be between 350 ns and 500 ns. A more precise measurement was impossible due to the noise in the signal. This range corresponds well to the expected speed found by taking the time for one half of a mechanical cycle at the resonant frequency (i.e. 658 ns) as an upper bound and then considering that the actual switching time will be faster due to the applied voltage and the nonlinear Duffing spring effect causing additional acceleration towards the destination electrode.

The structure's first resonant mode was at 760 kHz. The pull-in voltage was 48 V, with a 30 V hold voltage. Figure 5.5 shows that after an "initialization voltage" that exceeded the pull-in voltage, the structure was switched back and forth between pulled-in states with voltages that were less than 75% of the pull-in voltage (35 V). The suspended beam displaced a total of 1.8 μm during the switch operation. This switching speed combined with the total displacement of the switch and actuation voltage is a significant improvement in switching performance over standard parallel plate MEMS switches (approximately an order of magnitude improvement).

5.4 Waveguide Design and Fabrication

The second portion of the effort to develop the MEMS integrated optical switches was to develop low-loss waveguides in silicon. Previous work at Sandia National Laboratories developed low-loss waveguides in silicon nitride, however, the silicon nitride waveguides have a
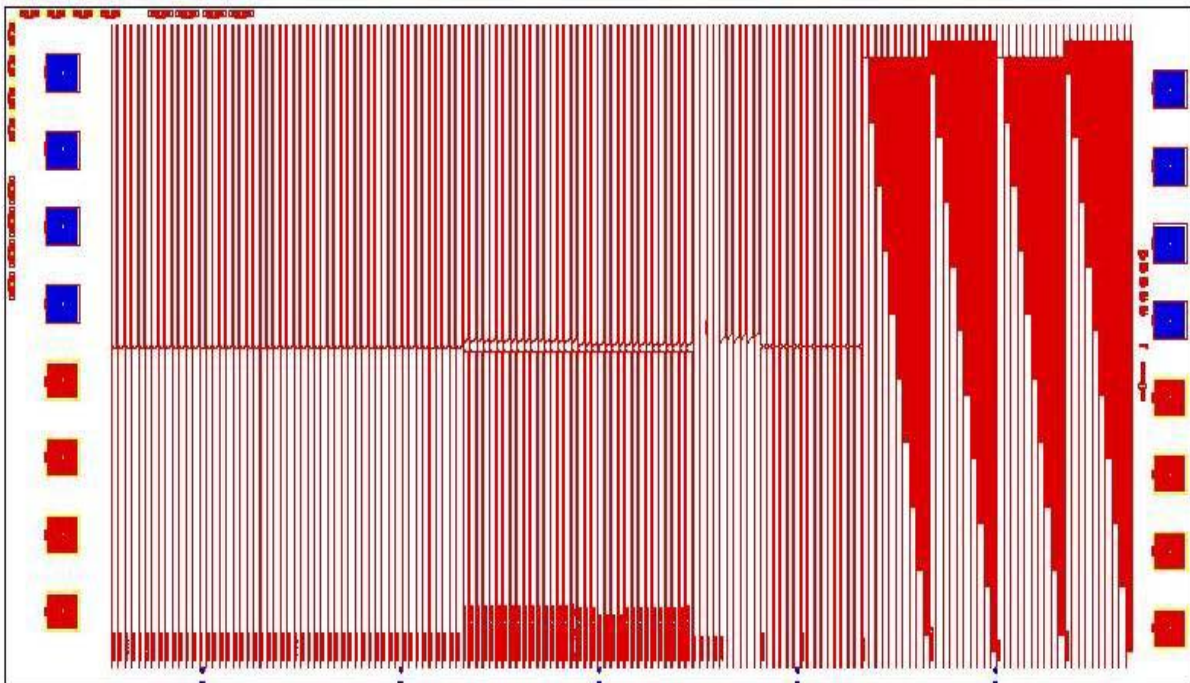
Figure 5.6 layout of the silicon integrated optics test mask. Mask includes couplers, ring resonators, and folded waveguide structures of a variety of dimensions to determine performance and optical loss.

larger cross-section and require much thicker cladding layers making integration with MEMS more challenging.

In the development of the silicon waveguides, amorphous, polycrystalline, and crystalline silicon waveguides were explored. The crystalline silicon waveguides came from silicon-on-insulator (SOI) wafers. The polycrystalline and amorphous silicon films were deposited in the MDL on top of TEOS oxide deposited on a silicon substrate.

A standard mask was developed with integrated optical test structures to determine the performance of the different silicon waveguides. Figure 5.6 shows this test mask layout. A variety of optical elements were designed into the mask including optical couplers, ring resonators, and long waveguide sections. In each of these elements a range of devices were designed with different dimensions to analyze the performance of the devices.

The silicon waveguides have a cross-section that is 500 nm wide by 200 to 250 nm thick. The coupling gaps designed in the mask went down to dimensions as small as 150 nm. To achieve this kind of resolution, it was necessary to use the highest resolution photo-lithography tool available in the MDL.

5.5 Waveguide Results

A number of wafers with silicon waveguides were fabricated in the MDL. Waveguides of amorphous silicon, polycrystalline silicon, and crystalline silicon were fabricated. The amorphous and polycrystalline silicon waveguides were found to be highly lossy, likely as a result of the many free bond sites within the material. The crystalline silicon waveguides were found to be quite low-loss. Waveguides with less than 1 dB/cm of loss have been demonstrated. This has allowed quality factors of ring resonators in the hundreds of thousands to be achieved.
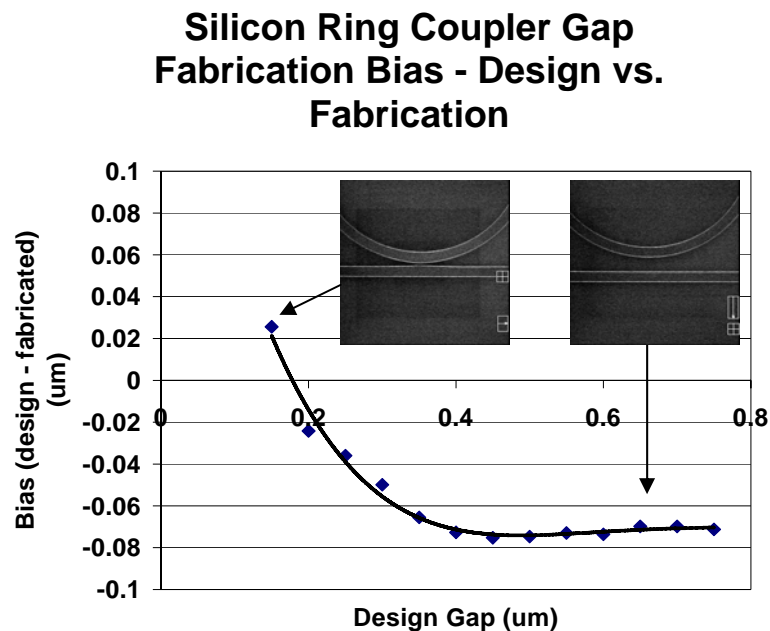
Figure 5.7 Proximity effects in the lithography and etch of the coupling gaps between ring resonators and waveguides.

The small dimensions of the coupling gaps led to some proximity effects in the lithography. This effect was studied to allow for compensation in future waveguide layouts. Figure 5.7 shows the proximity effect observed for coupling gaps in the waveguides. The proximity effects begin to be observed below a gap size of about 400 nm.

The waveguides themselves appeared to come through the fabrication very well. The sidewalls were quite smooth and the small features were well developed. Figure 5.8 illustrates some of these results.

(A)   (B)
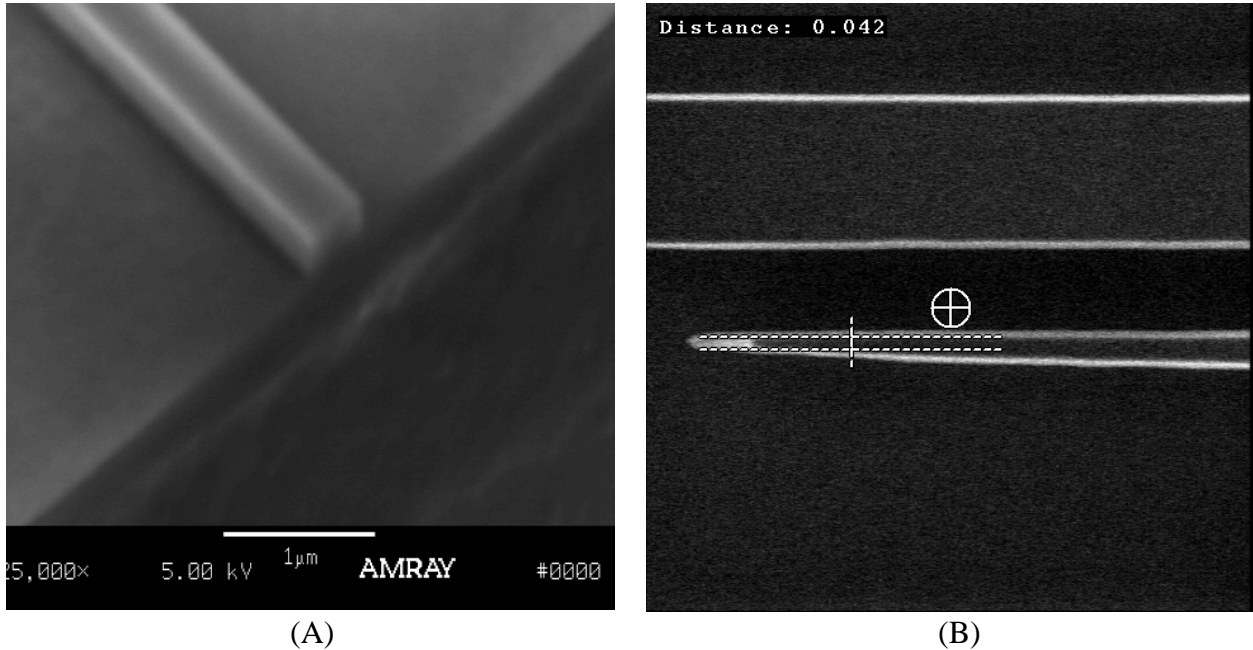
Figure 5.8 (A) illustrates the very low sidewall roughness of the fabricated waveguides. (B) shows some very fine features (~40 nm) that came through the waveguide fabrication.

5.6 Combined MEMS/waveguide Design

With the successful demonstration of both the MEMS switching structures and the waveguides, we next worked on integrating the waveguides with the MEMS devices. The fabrication process designed for the integration of the waveguides and the MEMS was complicated by the SOI requirement of the waveguide structures. The resulting fabrication process is described in the fabrication section (Section 5.7).

The design of the structure required silicon for the waveguide core, silicon oxide for a cladding layer, and polysilicon for the MEMS structure. All three of these components are required in the fixed-fixed MEMS beam. The challenge in the design of this structure is that the silicon oxide is compressive and can lead to buckling of the beams. This was considered in the design of the structures and a range of devices were designed where the length of the fixed-fixed beams were varied from slightly above the calculated critical buckling length to well below the critical buckling length. Figure 5.9 shows the layout of the masks for the devices. The details on the full array of devices designed for the prototype fabrication run of the integrated optical MEMS switches are given in Appendix E. Broadband switching devices where two waveguides were
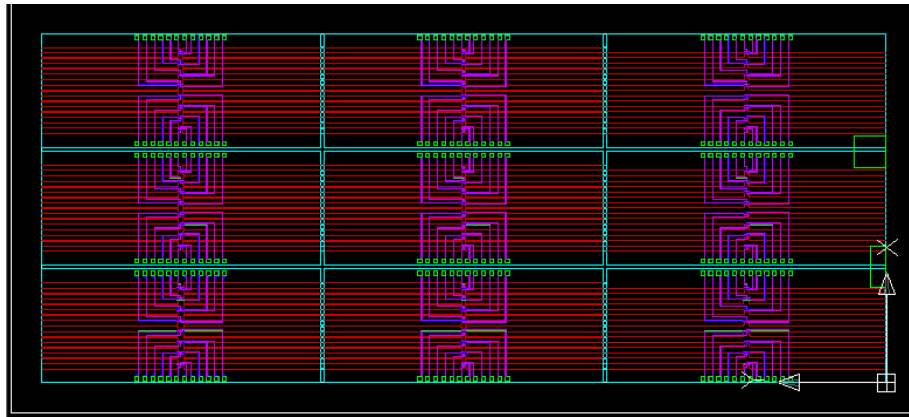
(A)
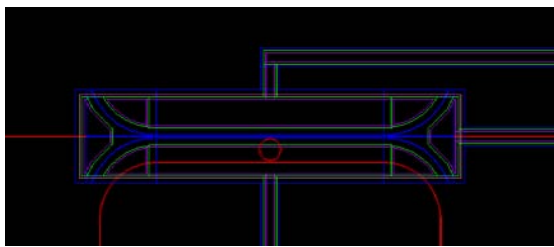
(B)
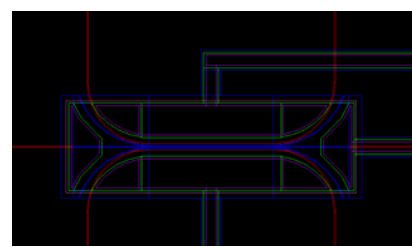
(C)

Figure 5.9 Mask layout for the integrated optical MEMS switch devices. (A) is the full reticle showing the nine different die. (B) is a wavelength selective switching device (i.e. with an optical resonator). (C) is a broadband coupling device (i.e. no optical resonator).

moved in and out of coupling were designed as well as wavelength selective switches were designed that moved a waveguide in and out of coupling with a ring resonator.

A range of coupling gaps were designed into the devices as well as a variety of initial gaps between the electrodes. The gaps were designed to be small to minimize the switching time required for the devices. These narrow gaps led to challenges during fabrication.

5.7 Integrated MEMS/Waveguide Fabrication

An experimental fabrication technology was considered for the creation of the integrated optical MEMS switching device. Significant process development work was done in the process of creating these devices. In this process, we encountered several problems with the fabrication strategy as well as created some robust solutions to those problems. Many of the problems encountered resulted from the very small gaps between the waveguides and MEMS electrodes. Also, in spite of the efforts to design structures that would resist buckling, significant problems with buckling of the center beam were encountered. Only the very shortest beams designed did not buckle.

Fabrication of an integrated optical switch was performed in the SiliconFab (MDL). The complete flow is represented in Figures 5.10 – 5.12.

a. Planar view of representative device

c. Pattern the silicon waveguides.

d. Apply 1.0 um oxide, 2.25 um polysilicon, 0.5 um oxide hard mask over waveguides

b. Start with SOI wafer
0.2 um silicon
3.0 um buried oxide (BOX)

e. Pattern hard mask, etch high aspect ratio trenches in polysilicon.
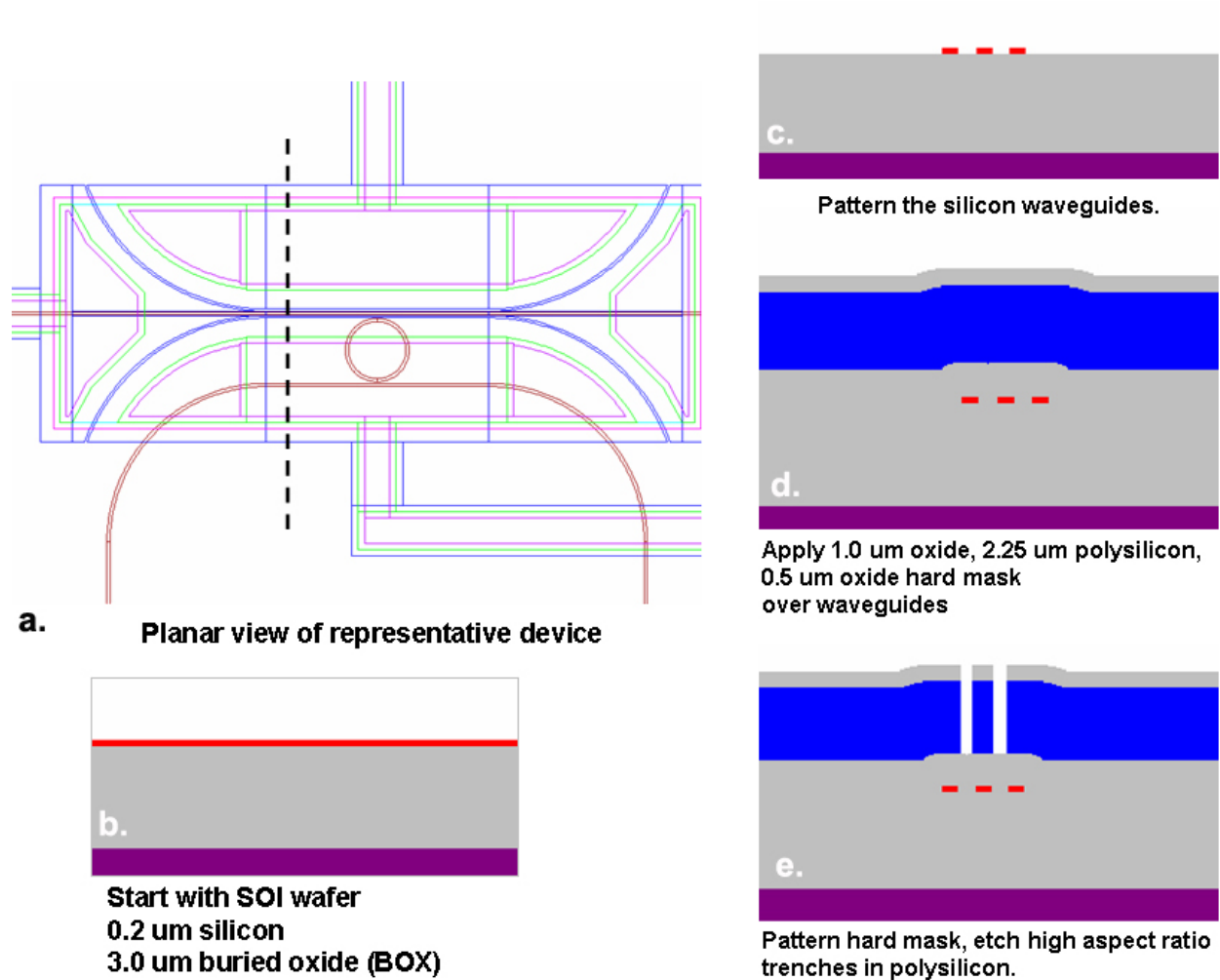
Figure 5.10 Design and 2D cross-sections of a representative element for the Integrated Optical Switch from the Sandia 2D Process Visualizer, Version 2.35.
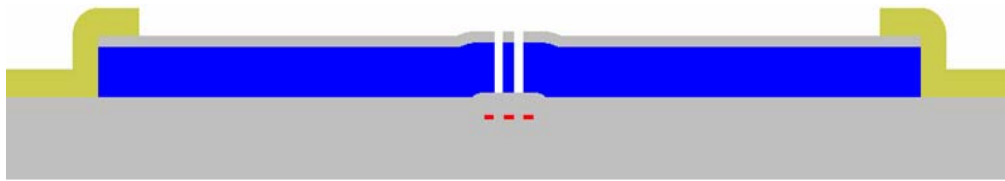
Photo pattern opening above the open features in the polysilicon.
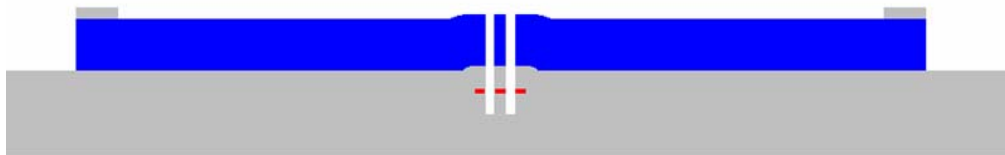
Use Polysilicon as hard mask to etch past the silicon waveguide into the oxide below
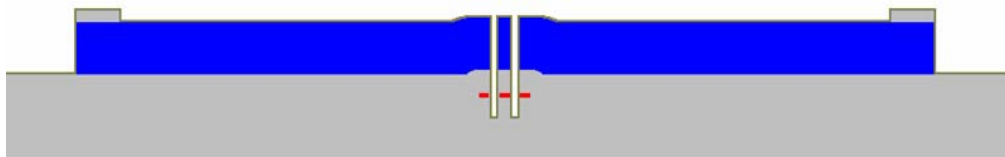
Coat all structures with silicon nitride in conformal deposition
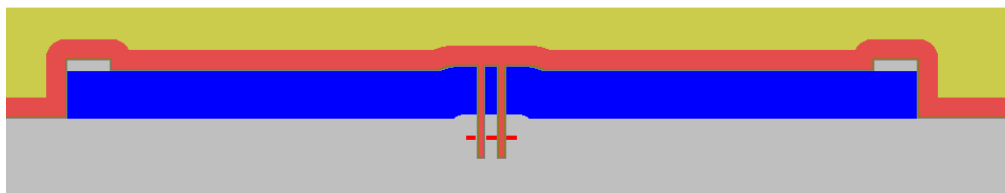
Coat all structures with PSG (Phosphosilicate Glass)
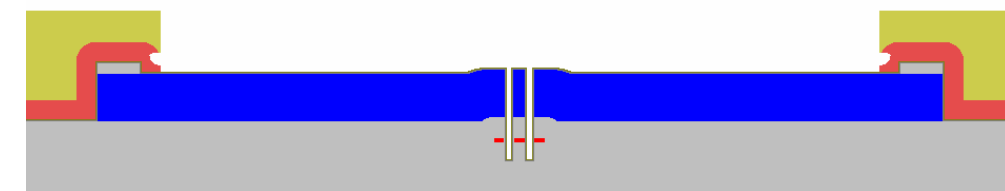
Wet etch PSG away from features in Hydrofluoric acid (HF)
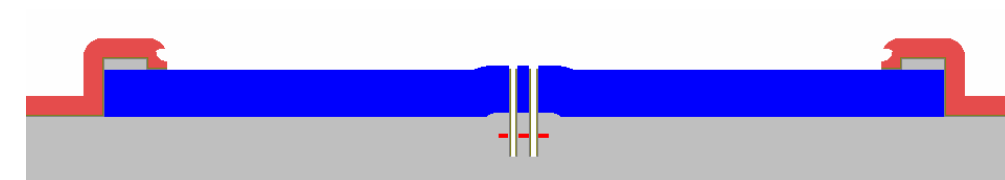
Reactive ion etch the bottoms of the trenches to allow access to lower oxide

Figure 5.11 Process flow continued from Figure 5.10.
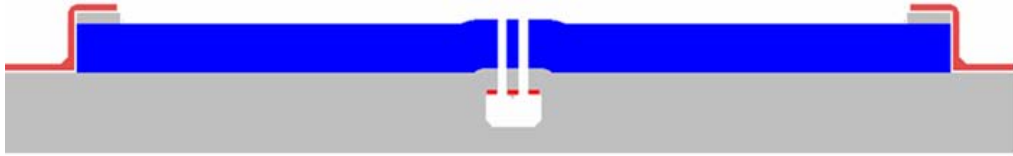
Undercut bottoms of trenches so the center is free to move, then etch PSG away with HF and silicon nitride away in hot Phosphoric acid.
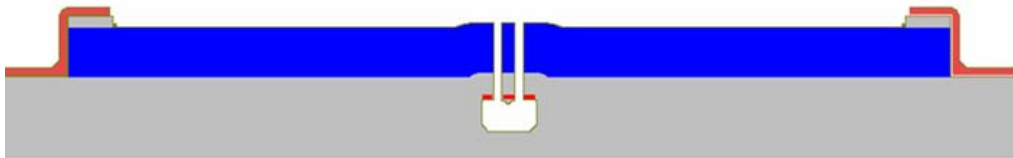
Coat all structures with silicon nitride in conformal deposition
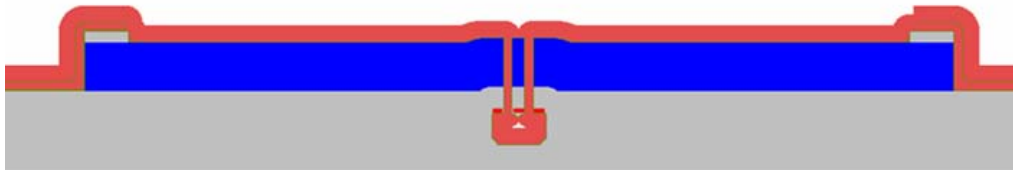
Coat all structures with PSG (Phosphosilicate Glass)
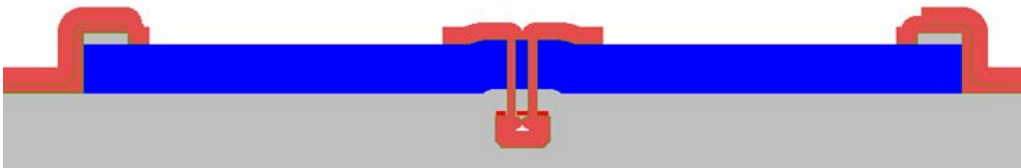
Pattern PSG glass to open areas that require metal
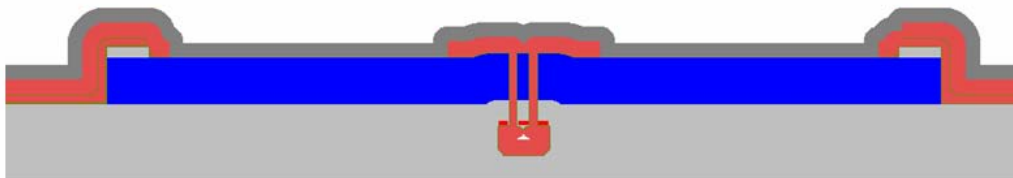
Coat with Aluminum-0.5%Copper
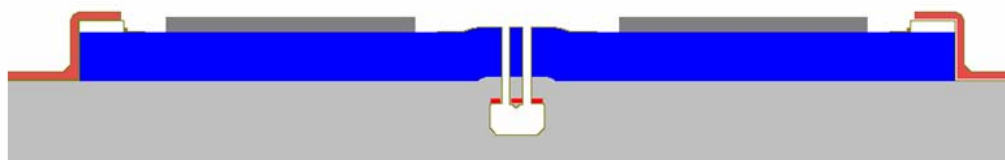
Pattern metal in RIE, and strip PSG glass away in HF - Complete

Figure 5.12 Process flow continued from Figure 5.11.

49

a. Pattern hard mask, etch high aspect ratio trenches in polysilicon.

b. First etch recipe didn't produce straight sidewalls.

c. After etch development cycle the sidewalls look very straight and consistent.
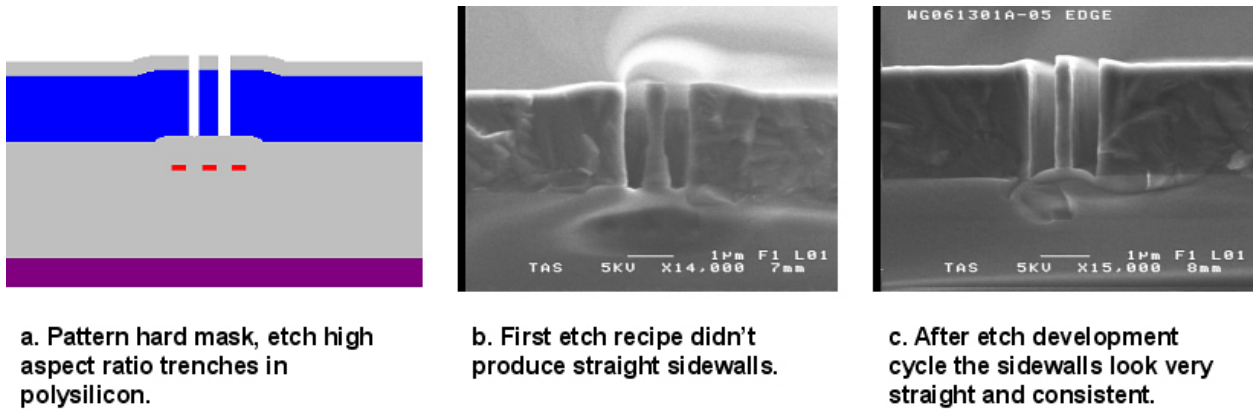
Figure 5.13 a. 2D cross section of high aspect ratio Polysilicon structure. b. First attempt at etching the trench. c. Straight sidewall, high aspect ratio etch profile from development cycle.

The silicon on insulator layer was patterned with the standard waveguide processes that have been shown to be low loss. The first non-standard process was the high aspect ratio etch for the mechanical structures as shown in Figure 5.13.

The second challenge that was encountered was the continuation of the etch into the silicon oxide material as shown in Figure 5.14a, where a timed etch was needed as well as a straight sidewall. The development cycle result seen in Figure 5.14b performed well, however the result on the actual devices shown in Figure 5.14c is tapered but acceptable.

Deep RIE etch past waveguide into oxide
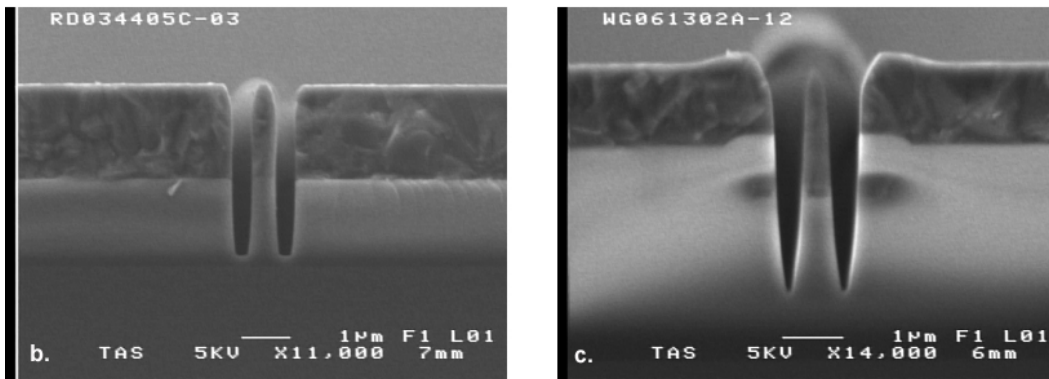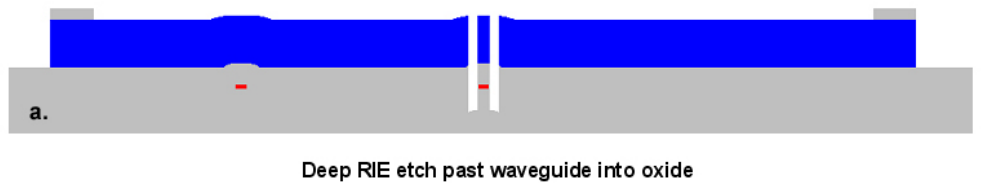
First process development etch was too deep but was able to get an etch rate.

Actual device with oxide etch past waveguides

Figure 5.14 a. 2D cross section of deep oxide etch profile. b. After development cycle a consistent etch channel was possible. c. Actual etch profile on device wafer.

Reactive ion etch the bottoms of the trenches to allow access to lower oxide.
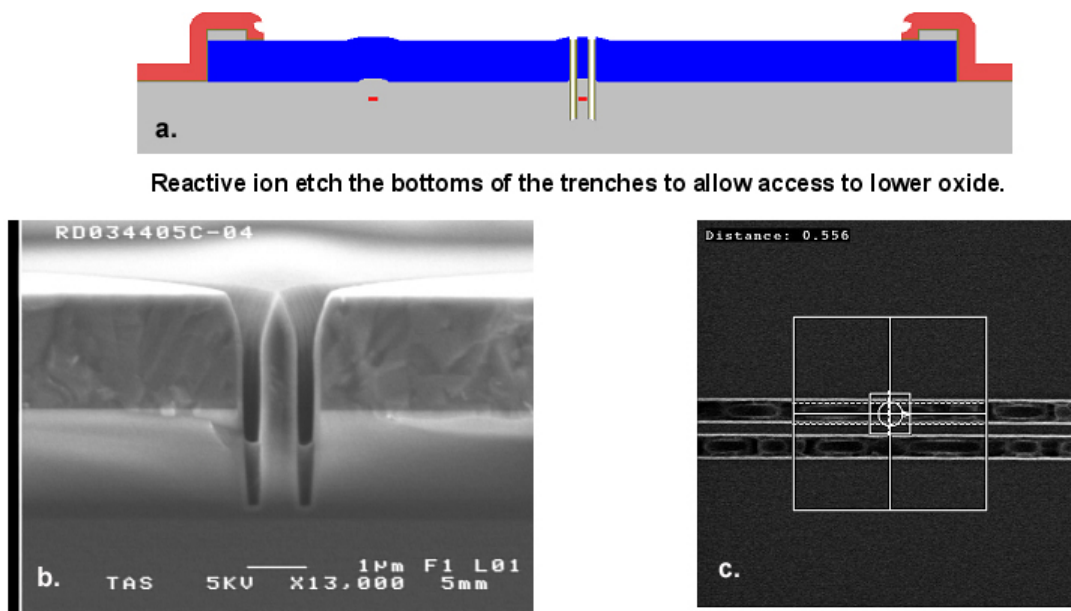
Figure 5.15 a. 2D cross section of intended silicon nitride open etch. b. first attempt at the open etch had photo resist (PR) remaining in trench. c. PR lattice can barely be seen remaining.

The nitride trench bottom open etch shown in Figure 5.15a that was initially attempted failed due to photo resist (PR) not being completely exposed and developed in the ASML Scanner stepper due to the narrow trench configuration. Figure 5.15b shows the result and Figure 5.15c shows the interference pattern that was created in the PR with an exposure wavelength of 248 nm.

The first lot (WG061301A) was processed with a large exposure energy 75 mJ and exposed 3 times to clear the PR. While this strategy worked on those wafers the lithography engineer was not willing to allow the strategy to be repeated due to of the possibility of degradation to the optics at those high energy levels. Also, some PR did not completely clear in some areas on the wafer.

The solution for this problem was to coat the wafers with Phosphosilicate glass (PSG) glass and pattern the glass with the lithography step, avoiding subjecting the deep narrow trench to the lithography step, and then stripping the PSG out of the trench with a wet process.

The PSG mask strategy worked for the intended purposes, but may have contributed to an undercut problem, which is discussed below. Successful trench bottom open step can be seen in Figure 5.16.
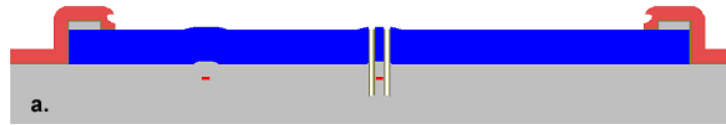
a.

Reactive ion etch the bottoms of the trenches to allow access to lower oxide.
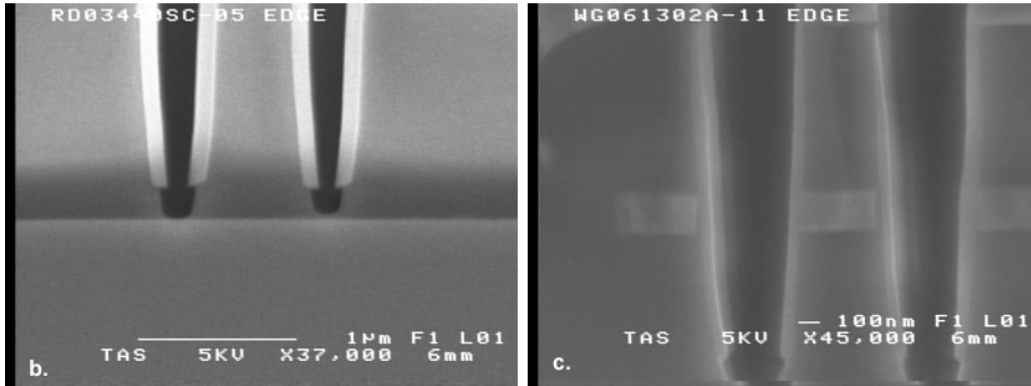
b. SEM of trench bottoms showing complete opening of the silicon nitride layer

c. Device with trench bottom open with silicon nitride on sidewalls

Figure 5.16 a. 2D cross section of the silicon nitride bottom open step. b. Successful silicon nitride trench bottom open. c. Enlarged view of a product wafer result showing the SOI waveguides.

The PSG etch used on the second lot (WG061302A) may have degraded and thinned the nitride protective layer in the trench at the interface of the polysilicon to silicon oxide interface, and the silicon nitride bottom etch thinned the protective layer even more allowing some defects at the interface. The undercut created the desired geometry but also produced some areas at the polysilicon to oxide interface that were not protected. Additional nitride was applied to the remaining wafers in the second lot (WG061302A) to be sure there was enough nitride before the trench bottom open step. None of the wafers in the second lot made it through the wet processes without having some undercut at the polysilicon to oxide interface. The first lot (WG061301A) wafers did make it through this step, where the PSG step was not used because the 75mJ energy level exposure which was repeated three times cleared most of the structures.

Undercut bottoms of trenches so the center is free to move, then etch PSG away
with HF and silicon nitride away in hot Phosphoric acid.
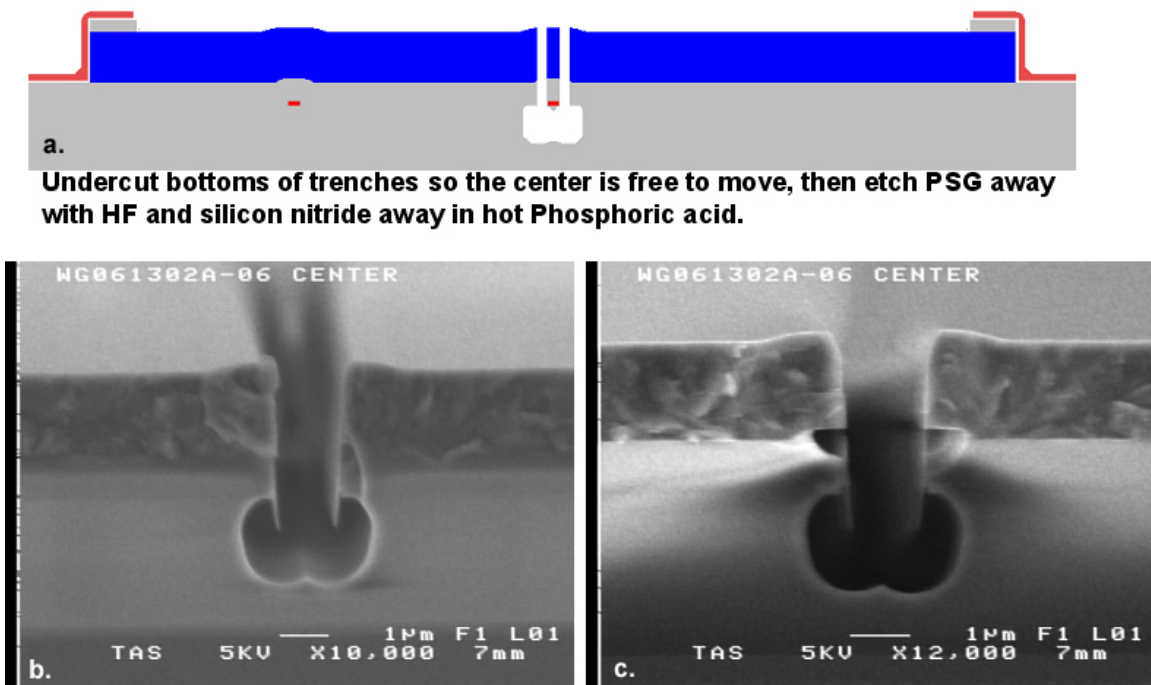
Figure 5.17 a. 2D cross section of undercut etch process step. b. Center beam is broken from cleaving the structure. Center beams were in tact before cleaving the wafer. c. Undercut between polysilicon to silicon oxide interface.

After the silicon nitride was removed in a wet process the beams had buckled, along with the undercutting of the oxide/polysilicon interface as can be seen in Figure 5.18. Backside films were removed to try to un-buckle the beams where the backside films held the wafer in relatively flat curvature as can be seen in Figure 5.19. By removing the films on the back side a negative curvature was predicted. That was not successful in relieving all the stress in the buckled beams.

The next effort was to over etch the oxide in the trenches by a short amount to reduce the oxide polysilicon interactions as shown in Figure 5.19b. That helped to some degree but significant buckling problems remained. The final attempt at straightening the beams was to anneal the wafers so we could get a maximum effect from the backside film removal. We annealed the 2 wafers left from lot WG061301A, that had backside films removed. One wafer had the over etch mentioned above in Figure 5.19b and the other did not. The only wafer that showed a significant number of unbuckled beams was wafer 1 which had all three processes performed (the backside films removed, the over etch, and the subsequent anneal). A detailed map was made that shows which die had unbuckled beams shown in Figure 5.20.

Some devices appear to have been completed successfully from wafer WG061301A-01. A SEM image of a completed device can be seen in Figure 5.21b. The SEM image shown in Figure 5.21c shows a device with too much over etch resulting in the release of the center waveguide. The majority of devices had waveguides that had come detached from the center beam. This is a challenge with timed wet processing, where wet processes have the tendency of being non-uniform due to varying solution flow around the wafers.
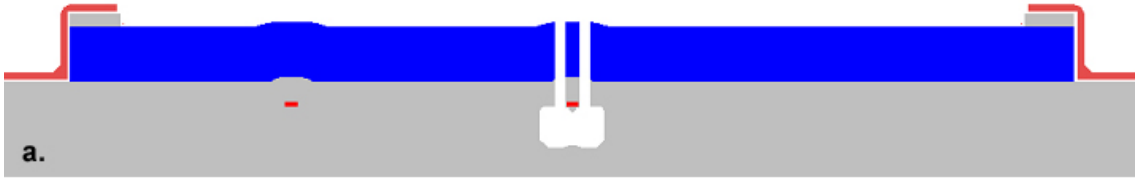
Second lot Undercut bottoms of trenches so the center is free to move, then etch PSG away with HF and silicon nitride away in hot phosphoric acid (hot phos).
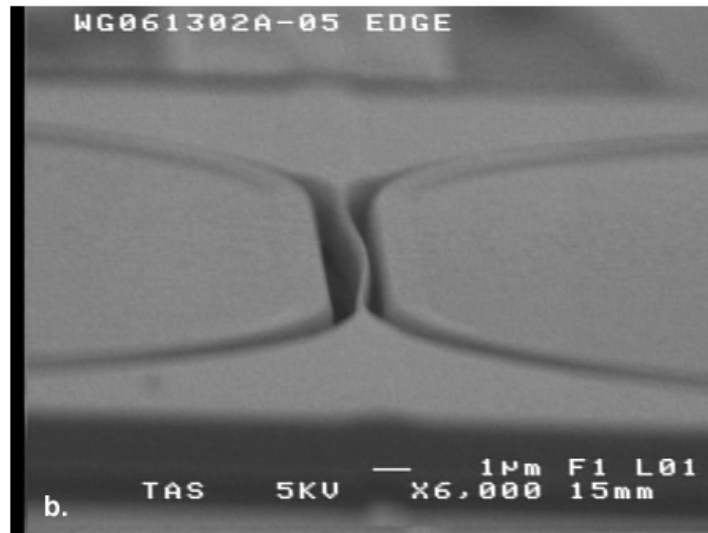
Figure 5.18 a. 2D cross section of undercut structure with silicon nitride removed. b. Buckled beam after silicon nitride was removed.
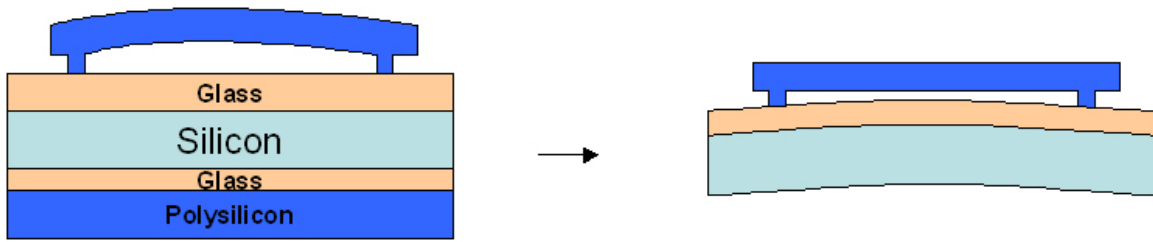
a. Backside films were removed to try and un-buckle the beams
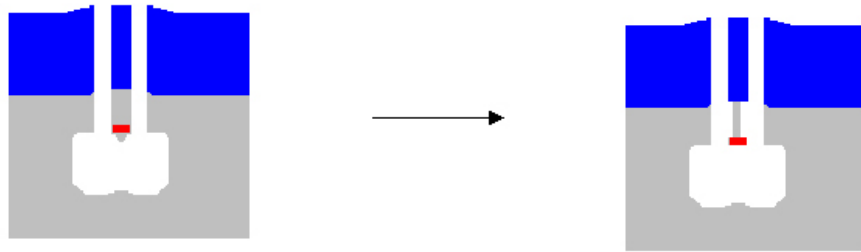
b. Over etch the oxide in the trenches by a short amount to reduce the oxide polysilicon interactions.

Figure 5.19 a. Representative picture of how to reduce stress in center beam by removing the backside films. b. 2D cross section of over etching the oxide between the waveguide and the polysilicon.

Figure 5.20 Map of which modules have straight center beams. Green is straight, red is buckled.
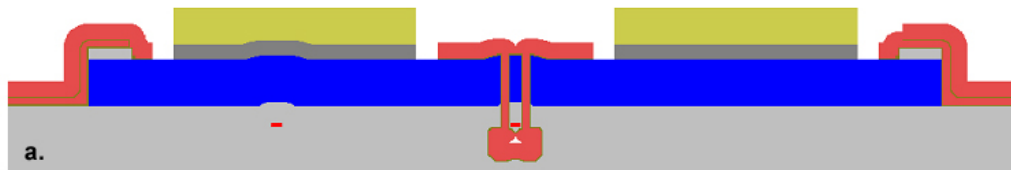
Pattern metal in RIE, cross section is shown with PR still on metal and PSG still in trenches.
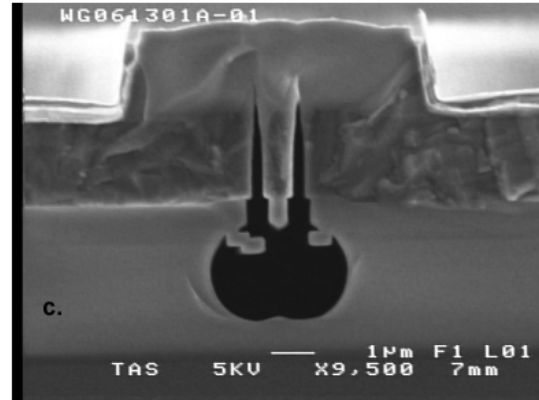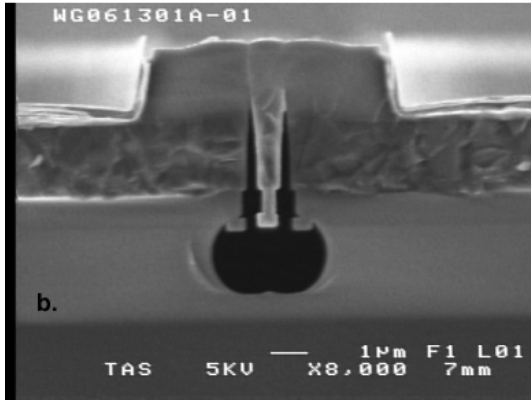
Figure 5.21 a. 2D cross section of metal process. Section is shown with PR still on metal and PSG still in trenches. b. Device that has been completed successfully. c. Device with too much over etch resulting in the release of the center waveguide.

5.7 Testing Results

Parts from WG061301A-01 were able to be released and tested. The devices were tested in a test stand designed and assembled for the testing of integrated optical chips. The light was injected into and collected from the chip using lensed fibers. Light from a tunable laser with wavelengths from 1495 nm up to 1620 nm was used in the testing.

The optical loss in the waveguides was found to be extremely high and only minimal light is able to be transmitted. Because of the very low amount of light transmitted, the switch performance characteristics were not able to be determined. In the testing performed, the beam structures were observed to move but due to the small dimensions it was impossible to determine anything further.

5.8 Discussion and Conclusions

The ultimate results of this work are mixed. The MEMS structures demonstrated alone were very successful. These devices demonstrated world record switch performance using the dynamic switching techniques. These devices were not able to be tested using the resonant pull-in due to the difficulty in sensing the change in capacitance of the small structures. However, overall the MEMS structures were a significant success.

The silicon waveguides that were first demonstrated within this project have been a tremendous success. This work has led to a number of new projects utilizing silicon waveguides as a key component. The problem with loss in the waveguides combined with the MEMS structures is

57

currently being investigated under a new project. TEM samples are being processed to look at the waveguide section of the devices and look for any apparent problems with the waveguide to oxide interfaces and also to look for large stress issues that may have been caused by the high temperature anneal sequence necessary for creation of the polysilicon structures.

A design of experiments is underway to discover why the waveguides have such high loss. Other silicon waveguides processed in this fabrication strategy without the high temperature anneals and polysilicon MEMS structures have very low losses so it is likely that the high temperature anneal causes changes in the materials that result in high losses. Other factors being looked at are the type of oxide deposition and the type of oxide precursor in the oxide cladding deposition, as some oxides have higher levels of carbon and hydrogen byproducts, and use different plasma generation methods, where there may be some plasma damage occurring form the initial stages of the deposition.

The next design will need to be modified to compensate for the residual stress in the fixed-fixed beams. There may be several approaches to this but the most likely approach is to incorporate a compliant structure in the beam section to allow for stress relaxation. Process modifications may also be needed in order to minimize out of plane bending in the beams due to the effective stress gradient in the beam created by the asymmetry of the oxide trapped between the beams and the waveguide. One strategy is to balance the surface forces between the polysilicon beams and the oxide cladding on the underside of the beams with a top oxide. The new design would also benefit from larger gaps so the lithography steps can be accomplished with standard processing parameters.

6.0 High Permittivity Materials for Electrical Isolation

For dynamic switching the hold voltage determines the minimum operating voltage of the switch. This means that any mechanism that decreases the hold voltage also decreases the actuation voltage as long as the mechanical damping is sufficiently low. So far in the experimental demonstrations, the hold voltage has been the limiting factor in the voltage required for switching. High-Permittivity materials have material properties that may reduce the required hold voltage thus leading to a decrease in the actuation voltage of the switches. These reductions are potentially significant depending on the material used.

6.1 Benefit of High-Permittivity Materials

Equation 2.2 in Section 2.1 gives the hold voltage resulting from the lumped parameter model given in Figure 2.1 of a parallel plate actuator. If the isolation layer is assumed to be a material with a relative permittivity different from the permittivity of free space, then the equation for the hold voltage becomes

$$V_h = \sqrt{\frac{2kdt_d^2}{\varepsilon_r^2 \varepsilon A}} \, , \qquad (6.1)$$

where the ε_r is the relative permittivity of the isolating dielectric material between the moving and the fixed electrodes and d is the distance of travel of the free electrode from its at rest position to the pull-in position defined by the dielectric material.

If Equation 6.1 is reorganized as

$$\left(\frac{V_h}{t_d}\right)\varepsilon_r = \sqrt{\frac{2kd}{\varepsilon A}} \, , \qquad (6.2)$$

and realizing that voltage over thickness term is maximized at the breakdown field of the dielectric material, it is clear that by maximizing the product of the breakdown field and the permittivity of the material selected for the isolation layer between the electrodes the highest stiffness (or largest gap or smallest area) MEMS device can be achieved. This product of permittivity and the breakdown field is the key material metric by which to determine the optimal dielectric material. This means that for electrostatic MEMS actuators that use dynamic switching and operate at a voltage limited by the hold voltage, there may be a significant benefit to using high permittivity dielectric materials that are beginning to be used as gate oxides in CMOS.

Table 6.1 lists some of the more common high-permittivity materials and compares them to silicon oxide and silicon nitride (which are commonly used as insulating layers in MEMS switching devices). The material properties listed in Table 6.1 indicate performance improvements of over a factor of two can be achieved by using high-permittivity materials. The real improvement could be even more significant than indicated here since the high-permittivity materials are still being developed and with higher quality materials the breakdown field will likely increase. Also, the values given for silicon oxide are for very high quality silicon oxide used in transistor gates. The silicon oxides used with MEMS devices typically have lower performance parameters than those given in Table 6.1.

One consideration that is not included as a material parameter in Equation 6.2 is the propensity of the material to trap charges. This is a significant problem for dielectrics associated with MEMS structures. This is an area of research that has not been well explored but there are some indications that operating MEMS structures in a vacuum significantly decreases the trapped charges in the materials [10]. Any consideration of different dielectric materials must account for dielectric charging.

Table 6.1 Dielectric constants and breakdown fields of high-permittivity materials compared with silicon oxide and silicon nitride[11-15]. The product of the two material parameters is the key metric for minimizing the hold voltage of the devices. The performance improvement is essentially the increase in resonant frequency (i.e. switching speed) at a set voltage achieved through using the material in place of silicon oxide (or the decrease in required voltage for a set resonant frequency).

Material	Dielectric Constant	Breakdown Field (MV/cm)	Product (MV/cm)	Performance Improvement Factor Relative to Silicon Oxide
SiO_2	3.9	15	58.5	0.0
Si_3N_4	7	10	70	1.20
Al_2O_3	9	10.3	92.7	1.58
Y_2O_3	15	4	60	1.03
La_2O_3	23	4.2	96.6	1.65
Ta_2O_5	28	4.5	126	2.15
TiO_2	80	1.35	108	1.85
HfO_2	25	4	100	1.71
ZrO_2	25	4	100	1.71

6.2 Fabrication of MEMS Switches with High-Permittivity Materials

The MEMS switches used for the experimental demonstration of the high-permittivity materials for electrical isolation are those described in Section 5.1 where the MEMS structure is created out of a single polysilicon layer. For these devices, the silicon nitride isolation layer was omitted during processing of the structures and the devices were fabricated, diced, released and wirebonded without any dielectric coating. At this point, the entire package with the MEMS switches was loaded into an atomic layer deposition tool and the high-permittivity dielectric materials were deposited on the devices to a thickness of 55 nm. The materials explored were aluminum oxide (Al_2O_3- ALD done at Sandia) and hafnium oxide (HfO_2 – ALD done at the University of Illinois at Champagne-Urbana). Zirconium Oxide (ZrO_2 – ALD done at Sandia) was also deposited on MEMS structures but those devices were delivered late and were not able to be tested.
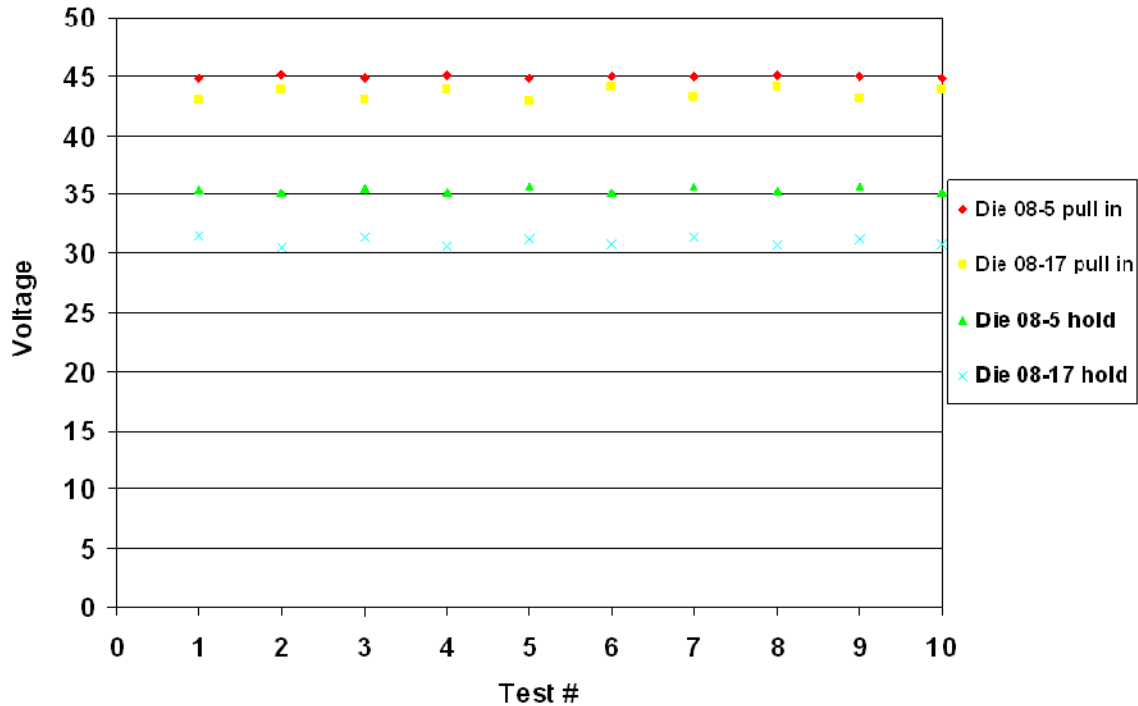
Figure 6.1 Pull-in and hold voltage test results in vacuum from two devices. Both were devices were design #3 from two different #8 die. These devices had 55 nm of aluminum oxide deposited as an isolating dielectric layer.

6.3 Experimental Results

The devices were tested in vacuum to determine their pull-in and hold voltages for the devices. Tests were also conducted in air but had significant variability in the data, likely due to dielectric charging. The vacuum data was much more consistent. Each device was subjected to a series of 10 test cycles of pull-in and release. The pull-in and hold voltage was recorded for each cycle. The polarity of the applied voltage was reversed with each pull-in cycle to help avoid charging effects (in vacuum dielectric charging effects were not observed).

Figure 6.1 shows results from two different #3 devices on die #8 chips with aluminum oxide coating the structure. Figure 6.2 shows the results from a device #3 from die #8 with hafnium oxide deposited on the structure. The results from all devices from which data could be collected is found in Appendix F. Because of differences between devices in terms of beam dimensions as well as the significant differences in the materials used as isolation layers (such as residual stress and modulus) it is difficult to compare performance results between the devices. The aluminum oxide coated devices appeared to be much more robust than the hafnium oxide coated devices. This may be due to the difference in tools (Sandia rather than the University of Illinois) used for the deposition rather than anything intrinsic to the film itself. These results demonstrate that using high-permittivity dielectrics as an isolating material in MEMS is feasible with the result being higher performing switches.
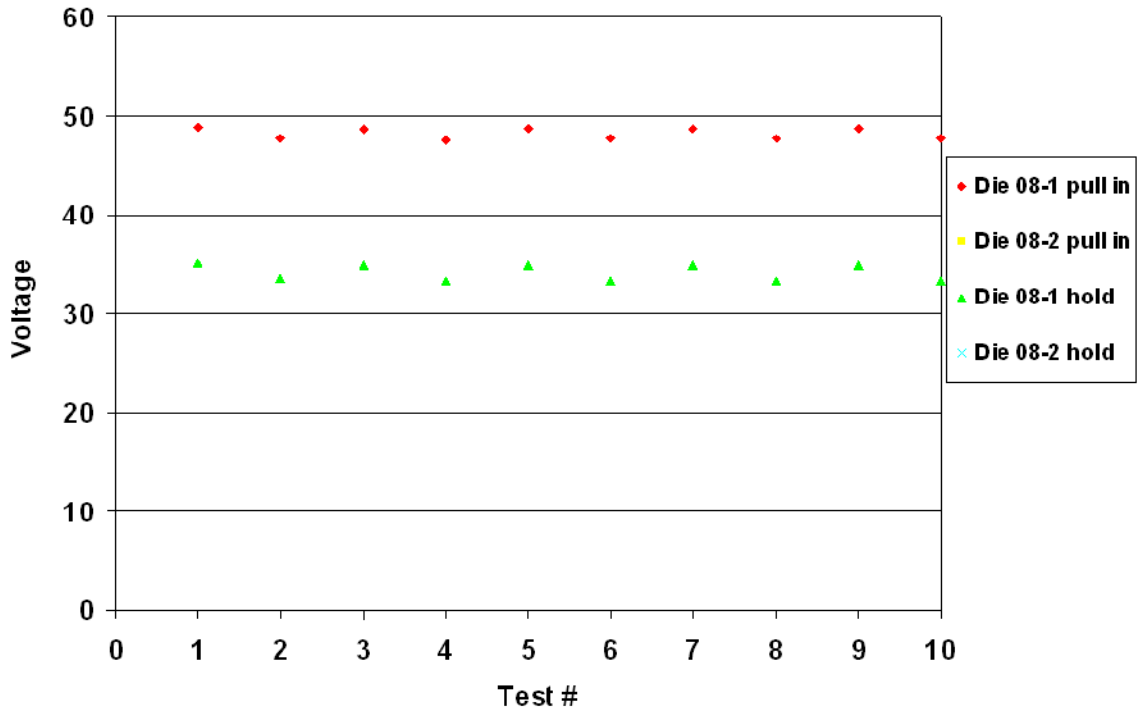
Figure 6.2 Pull-in and hold voltage test results in vacuum for device design #3 from die #8. This device had 55 nm of hafnium oxide deposited as an isolation layer. (Note that another device #3 from a different die was also tested but did not function.)

Further research is need to characterize the dielectric films in terms of residual stress, Young's modulus, and Poisson's ratio to fully characterize the mechanical behavior of the switch. High cycle number tests also need to be performed to understand any fatigue effects. Finally, efforts to maximize the breakdown field of the film as well as the permittivity are of significant value.

7.0 Discussion of Results

This project successfully demonstrated dynamic switching of MEMS devices and in the process set new high-speed switching marks for both torsional devices as well as parallel plate devices. This is a significant accomplishment that extends the range of applications addressable by MEMS switching devices. Switching at sub-microsecond speeds is desirable in optical switching as well as in RF MEMS switches. At smaller scales switching times can approach the nanosecond range which would allow these NEMS switches to compete with CMOS transistor switches in certain metrics.

The focus of this work was primarily in switching in the optical domain. The MEMS micromirror switches designed as part of this project demonstrated for the first time sub-microsecond switching of micromirrors. In fact, the switching time observed was an order of magnitude improvement over the next fastest published result for a micromirror device. This development now allows MEMS micromirror devices to compete with acousto-optic modulators for switching light in a large number of applications. One application of particular interest for Sandia National Laboratories is a need for these mirrors in ion and neutral-atom trap based quantum computers. To date there is no other device available that would allow scaling up the size of these kinds of quantum computers [9].

Another area of effort has been the development of a high-speed MEMS-enabled integrated optical switch where light is switched on-chip from one waveguide to another through evanescent coupling. While the complete integrated optical switch structure was not ultimately functional, there were a number of significant developments resulting from this work. The first key demonstration was the in-plane parallel plate switching device that utilized dynamic switching. With this demonstration, a new switching speed record was set for a MEMS device switching over a gap of nearly two microns. In addition to this demonstration, silicon waveguide technology was developed at Sandia. This capability has gone on to contribute to a number of both internally and externally funded projects. This capability significantly extends Sandia's technological ability. Finally, we also demonstrated the use of high-permittivity dielectrics as isolation layers in these MEMS devices. These materials can provide more than a factor of two reduction in the actuation voltage required for MEMS switches. This is a significant development that has not been demonstrated before.

These unprecedented results position Sandia National Laboratories as a leader in high-speed MEMS switching and has led to a number of follow-on projects resulting from the technologies developed. By both technical and programmatic metrics this has been a highly successful project.

References

1. Rebeiz, G. M., *RF MEMS Theory, Design, and Technology*, John Wiley & Sons, Hoboken, New Jersey, 2003.

2. Nielson, G. N., Olsson, R. H., Bogart, G. R., Resnick, P. R., Spahn, O. B., Tigges, C., Grossetete, G., Barbastathis, G., "Dynamic pull-in and switching for sub-pull-in voltage electrostatic actuation," *The 14th International Conference on Solid-State Sensors, Actuators, and Microsystems* (Transducers '07), vol. 1, p. 455-459, June 2007.

3. Nielson, G. N., Barbastathis, G., "Dynamic pull-in of parallel plate and torsional electrostatic MEMS actuators," *Journal of Microelectromechanical Systems* (JMEMS), vol. 15, p. 811-821, Aug. 2006.

4. Czaplewski, D. A., Nielson, G. N., Nordquist, C. D., *Nanomechanical Switching at 1 ns and 1 V using an In-plane Dynamic Switching Technique*, Sandia National Laboratories proposal to DARPA, July 2007.

5. L. J. Hornbeck, "A Digital Light Processing^{TM} update – status and future applications," in *Proceedings of the IS&T/SPIE Conference on Projection Displays V* (SPIE, San Jose, 1999), pp. 158-170.

6. D. S. Greywall, et al., "Crystalline silicon tilting mirrors for optical cross-connect switches," JMEMS 12, 708-712 (2003).

7. J.-C. Tsai and M. C. Wu, "Gimbal-less MEMS two-axis optical scanner array with high fill-factor," JMEMS 14, 1323-1328 (2005).

8. *Sandia MEMS Advanced Design Short Course*, Class Materials, 2004.

9. A. Steane, "How to build a 300 bit, 1 Giga-operation quantum computer," arXiv.org /abs/quant-ph/0412165, 1-13 (2006).

10. Nielson, G. N., Barbastathis, G., "A physically based model for dielectric charging in an integrated optical MEMS wavelength selective switch," *IEEE/LEOS International Conference on Optical MEMS and Their Applications* (Optical MEMS 2005), August 2005.

11. Wilk, G. D., Wallace, R. M., Anthony, J. M., "High-κ gate dielectrics: Current status and materials properties considerations," *Journal of Applied Physics*, 89, p. 5243-5275, 2001.

12. Kim, J.-Y., Barnat, E., Rymaszewski, E. J., Lu, T.-M., "Frequency-dependent pulsed direct current magnetron sputtering of titanium oxide films," *J. Vac. Sci. Technol.*, 19, p. 429-434, 2001.

13. Hausmann, D. M., de Rouffignac, P., Smith, A., Gordon, R., Monsma, D., "Highly conformal atomic layer deposition of tantalum oxide using alkylamide precursors," *Thin Solid Films*, 443, p. 1-4, 2003.

14. He, W., Schuetz, S., Solanki, R., Belot, J., McAndrew, J., "Atomic layer deposition of lanthanum oxide films for high-κ gate dielectrics," *Electrochemical and Solid-State Letters*, 7, p. G131-G133, 2004.

15. Kolodzey, J., Chowdhury, E. A., Adam, T. N., Qui, G., Rau, I., Olowolafe, J. O., Suehle, J. S., Chen, Y., "Electrical conduction and dielectric breakdown in aluminum oxide insulators on silicon," *IEEE Transactions on Electron Devices*, 47, p. 121-128, 2000.

Appendix A

Dynamic Pull-In of Parallel-Plate and Torsional Electrostatic MEMS Actuators

Gregory N. Nielson, *Member, IEEE*, and George Barbastathis, *Member, IEEE*

Abstract—An analysis of the dynamic characteristics of pull-in for parallel-plate and torsional electrostatic actuators is presented. Traditionally, the analysis for pull-in has been done using quasi-static assumptions. However, it was recently shown experimentally that a step input can cause a decrease in the voltage required for pull-in to occur. We propose an energy-based solution for the step voltage required for pull-in that predicts the experimentally observed decrease in the pull-in voltage. We then use similar energy techniques to explore pull-in due to an actuation signal that is modulated depending on the sign of the velocity of the plate (i.e., modulated at the instantaneous mechanical resonant frequency). For this type of actuation signal, significant reductions in the pull-in voltage can theoretically be achieved without changing the stiffness of the structure. This analysis is significant to both parallel-plate and torsional electrostatic microelectromechanical systems (MEMS) switching structures where a reduced operating voltage without sacrificing stiffness is desired, as well as electrostatic MEMS oscillators where pull-in due to dynamic effects needs to be avoided. [1256]

Index Terms—Electrostatic devices, microactuators, microelectromechanical systems (MEMS), microresonators, nonlinear systems, switches.

NOMENCLATURE

m	Mass of the moving parallel-plate electrode.
I	Mass moment of inertia of the moving torsional electrode.
b	Damping coefficient.
k	Spring stiffness.
ϵ	Dielectric constant of medium between plates.
A	Overlap area of movable and fixed parallel plates.
L	Length of the moving torsional electrode from rotation center to tip.
w	Width of the moving torsional electrode.
d_0	Initial gap between plates.
x	Displacement of the movable plate.
$\dot{x}$	Velocity of the movable plate.
$\ddot{x}$	Acceleration of the movable plate.
$x_{\max}$	Step response overshoot or limit cycle amplitude.
$x^*_{\max}$	Maximum step response or limit cycle that does not lead to pull-in.
θ	Angular displacement of the movable torsional plate.
$\dot{\theta}$	Angular velocity of the movable torsional plate.
$\ddot{\theta}$	Angular acceleration of the movable torsional plate.
$\theta_{\max}$	Step response overshoot or limit cycle amplitude.
$\theta^*_{\max}$	Maximum step response or limit cycle that does not lead to pull-in.
θ_0	Maximum possible angular displacement of movable torsional plate.
V_0	Applied voltage.
V_{pi}	Quasi-static pull-in voltage.
V_{spi}	Step pull-in voltage.
V_{mpi}	Modulated pull-in voltage.
E_{injected}	Energy input into the system.
E_{kinetic}	Kinetic energy stored in the system.
$E_{\text{potential}}$	Elastic potential energy stored in the system.
$E_{\text{dissipated}}$	Energy lost from the system due to damping effects.
E_{stored}	Total energy stored in the system (kinetic plus elastic potential).
V_{bias}	DC bias voltage.
V_{tot}	Total applied voltage (dc bias plus modulated actuation voltage).
ω_n	Natural resonant frequency of the mechanical system.
t_{delay}	Time delay in closed-loop system.
ω	Frequency of the applied modulated actuation signal.

I. INTRODUCTION

IN microelectromechanical systems (MEMS) parallel-plate and torsional electrostatic actuators, the pull-in phenomenon has been effectively utilized as a switching mechanism for a number of applications, including optical and radio frequency (RF) switching devices [1]–[5]. *Pull-in* is the term that describes the snapping together of parallel-plate actuators due to a bifurcation that arises from the nonlinearities of the system.

Typically the analysis of the pull-in phenomenon is performed using quasi-static assumptions. However, it has been experimentally shown that under dynamic conditions, the pull-in voltage can be different from what the quasi-static analysis predicts. Sattler *et al.* found that for a torsional switch, the quasi-static pull-in voltage is 8 V; however, when the voltage is applied as a step function, the pull-in voltage is 7.3 V [1].

In this paper, analytical and numerical solutions exploring *dynamic* pull-in of both parallel-plate and torsional actuators are put forth. Pull-in due to a step input voltage is first examined and shown to be in agreement with the results of Sattler *et al.* The analysis is then extended to a case where a modulated voltage is applied and pull-in is experienced after a number of mechanical oscillations.

For pull-in to occur, a certain amount of energy needs to be injected into the system [6], [7]. The modulated voltage pull-in technique relies on energy being accumulated in the mechanical system during the pull-in process. This allows the energy required for pull-in to be input over a number of mechanical oscillations rather than all at once. The modulated pull-in technique thus requires less *power* for pull-in and leads to substantially lower voltage level requirements. The tradeoff for this lower actuation voltage is that the time for pull-in to occur is longer.

Our analysis of dynamic pull-in indicates that the pull-in points for both the step voltage case and the modulated voltage case are shown to be dependent on the system damping, represented by the quality factor of the mechanical system. For critically damped or overdamped structures, it is found that the quasi-static analysis adequately describes pull-in, regardless of the applied potential function. However, for underdamped systems, the dynamic behavior can have a significant effect on the pull-in voltage.

II. System Model

To explore the dynamic response and pull-in of both parallel-plate and torsional electrostatic actuators, lumped parameter models have been used. All of the mechanical terms (inertia, damping, and stiffness) have been assumed to be linear. The electrostatic force term is, of course, nonlinear for both the parallel-plate and the torsional actuator cases. The important assumptions made in selecting this model are related to the squeezed film effect, the motion and shape of the moving plate, and, for doubly clamped parallel-plate structures, the axial stretching effect. Additionally, the charging and discharging of the capacitor formed by the two plates is assumed to be fast relative to the mechanical system.

The squeezed film effect can cause both the damping and the stiffness terms to become nonlinear [8]–[10]. For the lower quality factors discussed in this paper ($Q < 10$), the validity of the linear damping and stiffness assumption depends very much on the geometry of the structure. For example, the moving plate needs to have adequate squeeze film damping holes to make the nonlinear squeezed film effects negligible. For the higher quality factors discussed in this paper, the structures would need to be in a vacuum, which significantly reduces the squeezed film effect, regardless of the geometry of the structure.

In the two models that we propose, the motion of the plates has been idealized. The parallel plate is assumed to only displace in the dimension perpendicular to the plane defined by the fixed electrode, and the displacement is assumed to be the same for all points on the movable plate. The motion for the torsional case is assumed to be strictly rotational about the point where the torsional springs are attached. How well these assumptions hold

depends predominantly on the geometry of a particular device [11].

For a doubly clamped plate in a parallel-plate actuator, axial stretching can introduce a nonlinear term into the mechanical stiffness of the structure. This nonlinear effect is called the Duffing nonlinearity. The relative significance of this nonlinear term depends on the geometry of the structure as well as the residual stress present in the plate [11], [12].

In addition to these assumptions, which are intrinsic to the mathematical model, there are also assumptions implied about the electrical drive components. The assumption is that the RC time constant of the capacitor formed from the parallel-plate actuator is much smaller than the mechanical time constant. This allows the direct application of step voltages and other waveforms. If the electrical and mechanical time constants are similar, the voltage across the parallel plates would have a significant rise time as compared with the mechanical response [7]. In this case, the parallel-plate actuator is not voltage-controlled, as we have assumed, but charge-controlled. In addition, the circuit connecting the plates is always connected, allowing charges to flow freely as the voltage signals are applied. Finally, the gap between the plates is assumed to be small compared to the dimensions of the plate, allowing the capacitance to be calculated through the use of the ideal (i.e., negligible edge effects) parallel-plate capacitance formula.

While these modeling assumptions certainly do leave out a subset of electrostatic structures, the dynamic pull-in analysis provided in this paper should still provide some qualitative intuition into how those structures behave. For many electrostatic structures, the work presented in this paper should be directly applicable.

A. Parallel-Plate Model

The first electrostatic actuator model we will examine is the very common parallel-plate actuator. This type of actuator is typically modelled by the simplified diagram of Fig. 1. This model includes the assumptions discussed in Section II. The mathematical model derived from Fig. 1 is

$$m\ddot{x} + b\dot{x} + kx = \frac{\epsilon A V^2}{2(d_0 - x)^2} \qquad (1)$$

where m is the mass of the movable plate, b is the damping coefficient, k is the stiffness of the spring, ϵ is the dielectric constant of the surrounding medium, A is the area of the plate, and d_0 is the zero-potential spacing between the two electrodes. The dynamic variable x is the displacement of the plate from the position d_0 in response to the application of the potential V.[1] This model assumes that the gap between the two plates d_0 is small compared to the dimensions of the plates.

The quasi-static pull-in analysis of this system is well known and widely documented [5], [10]; however, we repeat it here to place our dynamic pull-in analysis in context. Combining (1)

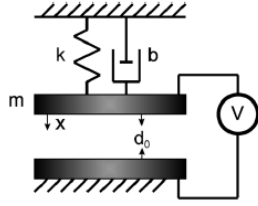[1]Nomenclature contains a list of the symbols used in this paper and their respective meaning.

67

Fig. 1. Lumped parameter model of a parallel-plate actuator.

with the quasi-static conditions $(\ddot{x} = \dot{x} = 0)$ gives the following for the required voltage for a particular equilibrium position:

$$V_0 = \sqrt{\frac{2kx(d_0 - x)^2}{\epsilon A}}. \qquad (2)$$

In the domain $0 < x < d_0$, (2) has a maximum at $x = d_0/3$. This is often referred to as the pull-in position. The equilibrium voltage associated with this point is called the pull-in voltage, since application of higher voltages will cause the system to experience a bifurcation to an equilibrium point located at $x > d_0$. Of course, this jump cannot be fully realized due to the fixed electrode; instead, the moving electrode "snaps on" to the fixed electrode. The pull-in voltage for the parallel-plate model under quasi-static conditions is

$$V_{pi} = \sqrt{\frac{8kd_0^3}{27\epsilon A}}. \qquad (3)$$

The voltage versus equilibrium plot for (2) shown in Fig. 2 indicates the pull-in voltage and position, and illustrates the system bifurcation. When the pull-in voltage is reached, the movable plate tries to jump to the equilibrium position to the right of the fixed electrode position. The isolation layer between the two electrodes will, of course, limit the plate's displacement so it will not reach the theoretical equilibrium position. The thickness of the isolation layer determines the voltage required to maintain the movable plate in the pulled-in state, referred to as the "hold" voltage [13].

B. Torsional Model

Fig. 3 shows a simple model for a torsional electrostatic actuator that, like the parallel-plate model, is based on the assumptions described earlier. From this model, the following equation of motion can be derived using a small angle approximation $(L \gg d_0)$ [1]:

$$I\ddot{\theta} + b\dot{\theta} + k\theta = \frac{\epsilon w V^2}{2\theta^2}\left[\frac{L\theta}{d_0 - L\theta} + \ln\left(1 - \frac{L\theta}{d_0}\right)\right] \qquad (4)$$

where I is the mass moment of inertia about the center of rotation, w is the width of the torsional plate, θ is the rotational displacement, L is the length of the plate from the center of rotation to the plate tip, and d_0 is the initial separation of the plates. This model is for a rectangular plate that measures $2L \times w$.

The torsional actuator also experiences pull-in. By again using a quasi-static assumption $(\ddot{\theta} = \dot{\theta} = 0)$, the following
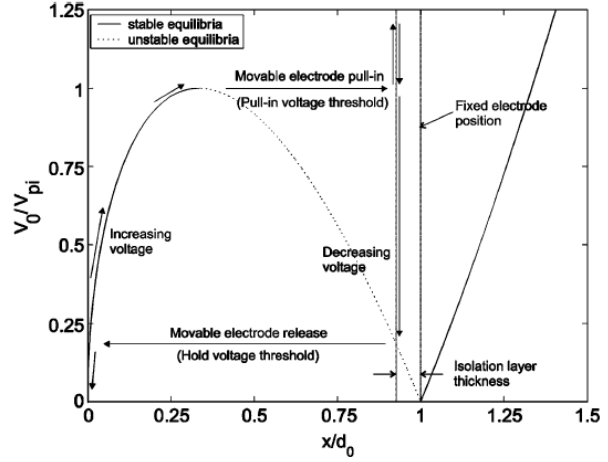

Fig. 2. Quasi-static equilibrium curve for the parallel-plate actuator from (2). The arrows showing the evolution of the equilibrium positions for increasing and decreasing voltage indicate the bifurcation in the system.
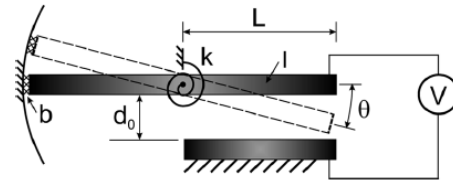

Fig. 3. Lumped parameter model for a torsional electrostatic actuator.

equation describing the voltage required for a given equilibrium position is found:

$$V_0 = \sqrt{\frac{2k\theta^3(d_0 - L\theta)}{\epsilon w\left[L\theta + (d_0 - L\theta)\ln\left(1 - \frac{L\theta}{d_0}\right)\right]}}. \qquad (5)$$

By numerically calculating the maximum of (5), the pull-in point is found to be [1]

$$\theta \approx 0.4404\theta_0 \qquad (6)$$

where θ_0 is the maximum torsional angle $(\theta_0 \approx d_0/L)$. The pull-in voltage associated with this point is given by

$$V_{pi} \approx \sqrt{0.827\frac{kd_0^3}{\epsilon w L^3}}. \qquad (7)$$

The voltage versus equilibrium curve for (5) is shown in Fig. 4. This curve is in many ways similar to the curve shown in Fig. 2, the main difference being that the local maximum (indicating the pull-in point) of the torsional curve is shifted slightly to the right of the maximum for the parallel-plate case.

III. STEP VOLTAGE RESPONSE AND PULL-IN

Perhaps the most common signal applied to parallel-plate or torsional electrostatic MEMS devices is a step voltage. For un-
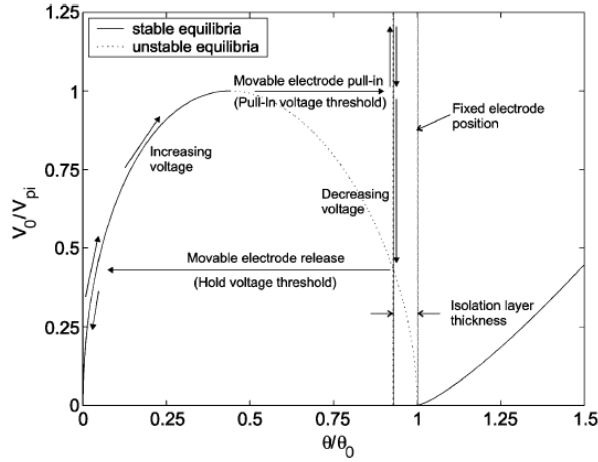
Fig. 4.   Quasi-static equilibrium curve for the torsional actuator from (5). The arrows showing the evolution of the equilibrium positions for increasing and decreasing voltage indicate the bifurcation in the system.

derdamped systems, the response of the structure to a step input causes the structure to overshoot the equilibrium position. If the overshoot is large enough, pull-in could potentially occur at voltages lower than V_{pi}.

For the step response analysis, the applied voltage will take the form

$$V(t) = V_0 U(t) \tag{8}$$

where $U(t)$ is a unit step function and V_0 is the magnitude of the voltage.

Due to the nonlinear nature of the parallel-plate and torsional models, finding an analytical solution for the step response is difficult. However, by analyzing the energy of the system, the important features of the system response, such as overshoot and pull-in, can be identified [2].

Initially, the system is at rest and has no stored energy. When the step voltage is applied, energy is injected into the system. The system stores this energy as both kinetic and potential energy. Over time, the stored energy above that associated with the equilibrium position is lost to damping. The energy balance of the system at any instant in time can thus be written as follows:

$$E_{\text{injected}} = E_{\text{kinetic}} + E_{\text{potential}} + E_{\text{dissipated}}. \tag{9}$$

The lowest possible pull-in voltage occurs when the overshoot has its maximum value. The overshoot can be maximized by setting the damping equal to zero. Under vacuum conditions, the damping can be made very small and, hence, the energy dissipation term in (9) can be neglected.

When the system is at its point of maximum overshoot, all of the stored energy is in the form of potential energy. The velocity, and, therefore, the kinetic energy, is zero at that point. By analyzing the energy of the system at this point, the decrease in the voltage required for pull-in can be calculated. We will use

this technique to analyze pull-in due to a step input for both the parallel-plate and the torsional actuators.

A. Step Voltage System Response—Parallel-Plate Case

For the parallel-plate actuator case, the stored potential energy can be expressed as

$$E_{\text{potential}} = \frac{1}{2} k x_{\max}^2 \tag{10}$$

where $x_{\max}$ is the maximum overshoot.

The energy injected into the system by the applied voltage can be found by integrating the force of the actuator over the displacement as

$$E_{\text{injected}} = \int_0^{x_{\max}} \frac{\epsilon A V_0^2}{2(d_0 - x)^2} \mathrm{d}x = \frac{\epsilon A V_0^2 x_{\max}}{2 d_0 (d_0 - x_{\max})}. \tag{11}$$

Combining (9)–(11) and setting the kinetic and dissipated energy terms to zero gives the following expression for the step voltage as a function of maximum overshoot:

$$V_0 = \sqrt{\frac{k d_0 x_{\max}(d_0 - x_{\max})}{\epsilon A}}. \tag{12}$$

Taking the derivative of (12) and setting it to zero $(\mathrm{d}V_0/\mathrm{d}x = 0)$ gives

$$x_{\max}^* = \frac{d_0}{2} \tag{13}$$

which is the position of the local maximum of (12) in the range of $0 < x < d_0$. It turns out that this corresponds to the largest maximum overshoot that can be achieved without pull-in occurring. Any increase in the step voltage would theoretically result in a maximum overshoot above d_0, due to a bifurcation similar to the quasi-static pull-in analysis. The step voltage associated with this maximum overshoot is, therefore, analogous to the quasi-static pull-in voltage expressed in (3). For this reason, we will refer to the step voltage associated with the overshoot expressed in (13) as the step pull-in voltage. It is given by

$$V_{spi} = \sqrt{\frac{k d_0^3}{4 \epsilon A}}. \tag{14}$$

Taking the ratio between the step pull-in voltage V_{spi} and the quasi-static pull-in voltage V_{pi} gives

$$\frac{V_{spi}}{V_{pi}} = \sqrt{\frac{27}{32}} \approx 0.919 \tag{15}$$

which indicates that the step pull-in voltage, for the ideal case of no damping, is about 91.9% of the quasi-static pull-in voltage. Since this solution was derived for the ideal case of no damping,
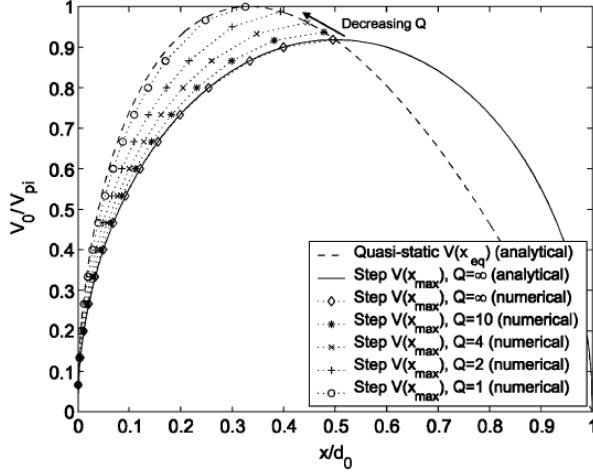
Fig. 5. Plot of the required voltage for a given maximum overshoot for various levels of damping (Q values). As the quality factor of the system decreases, the step pull-in voltage moves from the ideal step pull-in voltage with no damping to the quasi-static pull-in voltage value.

it represents a lower limit on the step pull-in voltage levels. The upper limit is provided by the quasi-static pull-in analysis.

Numerical simulations performed in Simulink of the response of the system in Fig. 1 with nonzero damping to a step voltage signal indicate that for moderate to low damping ($Q > 10$), the step pull-in voltage stays relatively close to the theoretically predicted fraction of 91.9% of the quasi-static pull-in voltage.[2] As the system damping increases, the step pull-in point follows the quasi-static equilibrium curve up until it reaches the quasi-static pull-in point, as shown in Fig. 5.

B. Step Voltage System Response—Torsional Motion

The approach used to analyze the step response of the torsional actuator is essentially the same as that used with the parallel-plate actuator. The energy relation given by (9) is again used to examine the energy at the point of maximum overshoot. For the torsional case, the energy injected into the system up to the point of maximum overshoot is given by

$$E_{\text{injected}} = \int\limits_{0}^{\theta_{\max}} \frac{\epsilon w V_0^2}{2\theta^2} \left[\frac{L\theta}{d_0 - L\theta} + \ln\left(1 - \frac{L\theta}{d_0}\right) \right] d\theta$$

$$= -\frac{1}{2}\epsilon w V_0^2 \left[\frac{1}{\theta_{\max}} \ln\left(1 - \frac{L\theta_{\max}}{d_0}\right) + \frac{L}{d_0} \right]. \quad (16)$$

The energy stored in the system at the maximum overshoot is

$$E_{\text{potential}} = \frac{1}{2}k_t\theta_{\max}^2. \quad (17)$$

If we assume no damping in the system, then the energy injected will always equal the energy stored. Solving (16) and (17)

[2]For example, numerical simulations give the ratio between the step pull-in voltage to the quasi-static pull-in voltage as 0.937 for a system quality factor of 10.

for the voltage gives the following relation between the max overshoot and the step voltage:

$$V_0 = \sqrt{\frac{-k\theta_{\max}^3}{\epsilon w \left[\ln\left(1 - \dfrac{L\theta_{\max}}{d_0}\right) + \dfrac{L\theta_{\max}}{d_0}\right]}}. \quad (18)$$

The maximum of (18) gives the maximum overshoot achieved before pull-in occurs. The location of this maximum is found numerically to be

$$\theta_{\max}^* \approx 0.645\theta_0. \quad (19)$$

This overshoot corresponds to a step pull-in voltage of

$$V_{spi} \approx \sqrt{0.687\frac{kd_0^3}{\epsilon w L^3}}. \quad (20)$$

The ratio of the step pull-in voltage to the quasi-static pull-in voltage gives

$$\frac{V_{spi}}{V_{pi}} \approx 0.911. \quad (21)$$

Again this solution was developed for a system with no damping and, therefore, represents a lower boundary on the decrease in pull-in voltage level required due to a step voltage input. Numerical simulations done in Simulink of the torsional system with increasing amounts of damping show that the step pull-in point follows the quasi-static equilibrium curve up until, at about a quality factor of one, the step pull-in occurs at the same point as the quasi-static pull-in, very much like the parallel-plate actuator case. Fig. 6 shows the analytical solution with no damping as well as the numerical solutions for various damping values compared with the quasi-static solution.

Sattler *et al.* [1] experimentally demonstrated the decreased pull-in voltage required when applying a step voltage to a torsional radio frequency (RF) MEMS switch. They found that the quasi-static pull-in voltage for their device was 8.0 V, while the step pull-in voltage was 7.30 V. These values give a ratio of 0.913 between the step pull-in voltage compared to the quasi-static pull-in voltage. As expected, this ratio is above the lower boundary defined by our analysis. However, the step pull-in point appears to be at about $0.58\theta_0$ for their experiments, which, based on our model, corresponds to a quality factor of about 3.75. For this quality factor, our analysis predicts the ratio of the quasi-static pull-in voltage to the step pull-in voltage to be 0.958, an overprediction of the experimentally observed values by about 4.5%. The small discrepancy is likely a result of the combination of small errors due to the assumptions made in our model, a lack of knowledge of the exact experimental conditions used in [1], and general experimental uncertainty.

IV. Modulated Voltage System Response and Pull-In

The analysis of the step voltage pull-in indicates that by making use of the energy storing capabilities of the mechanical
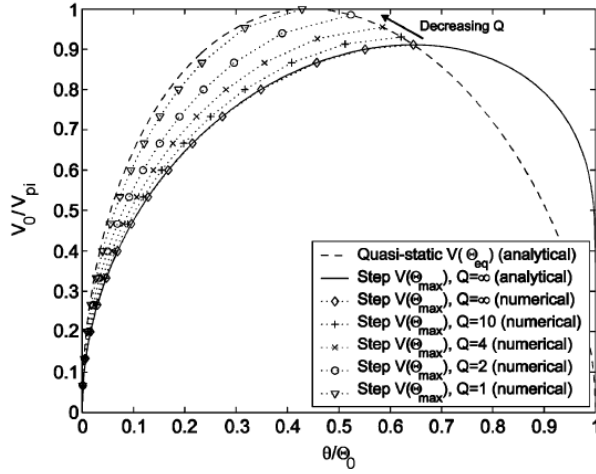
70

Fig. 6.   Plot of the required voltage for a given maximum overshoot for various levels of damping (Q values) for the torsional actuator. As the quality factor of the system decreases, the step pull-in voltage moves from the ideal step pull-in voltage with no damping to the quasi-static pull-in voltage value.

system, pull-in can be achieved at voltages lower than the levels predicted by the quasi-static analysis. This idea of leveraging the energy stored in the mechanical system can be taken even further by applying a voltage signal that is modulated according the rule

$$V = \begin{cases} V_0, & \text{if the velocity } (\dot{x} \text{ or } \dot{\theta}) > 0 \\ 0, & \text{otherwise.} \end{cases} \qquad (22)$$

The voltage signal will input energy into the mechanical system over a number of mechanical oscillations. This technique leads to larger displacements than would be possible with an unmodulated actuation signal at the same voltage level [14]. In addition to the injected energy, a certain amount of energy is lost to damping during each cycle. After some number of cycles, there are two possible outcomes. Either the system will reach a limit cycle where the energy input equals the energy lost per cycle [15], or the system will reach a pulled-in state. First, let us assume that the system reaches a limit cycle. The energy balance of the system at the limit cycle is

$$E_{\text{injected}} = E_{\text{dissipated}}. \qquad (23)$$

Deriving expressions for both terms in (23) leads to expressions for the modulated voltage levels needed for pull-in to occur. This modulated actuation technique will be explored for both the parallel-plate actuator and the torsional actuator.

A. Modulated Voltage System Response—Parallel-Plate Case

For the parallel-plate case, the energy injected per period is

$$E_{\text{injected}} = \int_{-x_{\text{max}}}^{x_{\text{max}}} \frac{\epsilon A V_0^2}{2(d_0 - x)^2} \mathrm{d}x = \frac{\epsilon A V_0^2 x_{\text{max}}}{(d_0^2 - x_{\text{max}}^2)} \qquad (24)$$

where x_{max} refers to the amplitude of the limit cycle.

The energy dissipated is found indirectly by using the definition of the quality factor along with the stored energy in the system. The quality factor definition is

$$Q = 2\pi \frac{E_{\text{stored}}}{E_{\text{dissipated}}}. \qquad (25)$$

By using this definition in the derivation, we are implicitly assuming that the displacement is sinusoidal in time. Due to the nonlinearities of the system, this is not exactly true. However, for moderate- to high-quality factors ($Q > 10$), the assumption is quite reasonable.[3]

At the point of maximum displacement x_{max}, all of the stored energy is in the form of elastic potential energy. The stored energy can thus be expressed as

$$E_{\text{stored}} = \frac{1}{2}kx_{\text{max}}^2. \qquad (26)$$

By combining (23)–(26), it is possible to find a relationship for the modulated voltage level V_0 required for a given amplitude limit cycle. This relationship is

$$V_0 = \sqrt{\frac{\pi k x_{\text{max}}(d_0^2 - x_{\text{max}}^2)}{\epsilon A Q}}. \qquad (27)$$

The amplitude of the limit cycle which corresponds to the maximum voltage that leads to a limit cycle can be found by taking the derivative of (27) and setting it to zero ($\mathrm{d}V_0/\mathrm{d}x = 0$). This gives

$$x_{\text{max}}^* = \frac{d_0}{\sqrt{3}} \approx 0.577 d_0. \qquad (28)$$

The voltage associated with the limit cycle amplitude in (28) is referred to as the modulated pull-in voltage V_{mpi}. For any voltage V_0 above this voltage, the system will pull-in after some number of mechanical oscillations. By combining (27) and (28), the modulated pull-in voltage is found to be

$$V_{mpi} = \sqrt{\frac{2\pi k d_0^3}{3\sqrt{3}\epsilon A Q}}. \qquad (29)$$

The ratio of the modulated pull-in voltage V_{mpi} to the quasi-static pull-in voltage V_{pi} is

$$\frac{V_{mpi}}{V_{pi}} = \sqrt{\frac{3\sqrt{3}\pi}{4Q}} \approx 2.02\sqrt{\frac{1}{Q}}. \qquad (30)$$

This indicates that for a system with a quality factor of 100, the modulated pull-in voltage would be only 20% of the quasi-static pull-in voltage. This is a significant decrease in the required pull-in voltage. Systems with higher quality factors can lead to even lower voltage level requirements. Fig. 7 gives the

[3]An alternative derivation, where a sinusoidal displacement is assumed explicitly and the dissipated energy is calculated directly, gives identical results.
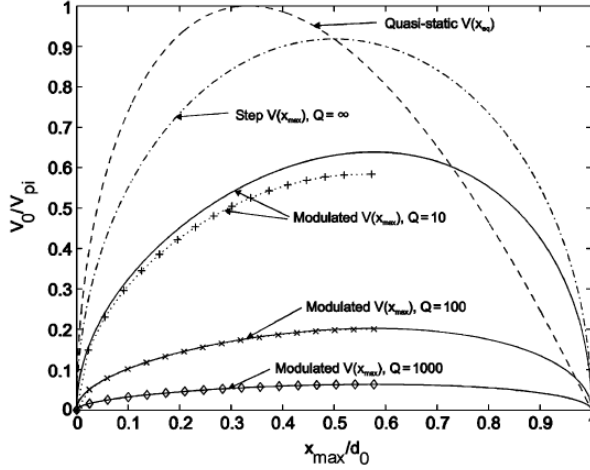
Fig. 7. Numerical and analytical curves of the modulated voltage required for particular limit cycle amplitudes for parallel-plate systems with quality factors of 10, 100, and 1000. The analytical solutions from (27) are the solid lines. The numerical simulation results are given by the data points. For $Q = 10$, the numerical and analytical solution show some discrepancy due to the sinusoidal motion assumption used in the analytical derivation. For comparison, the quasi-static equilibrium curve (2) and the step response curve (12) are also plotted. The peak of each curve defines that curve's pull-in voltage and position.
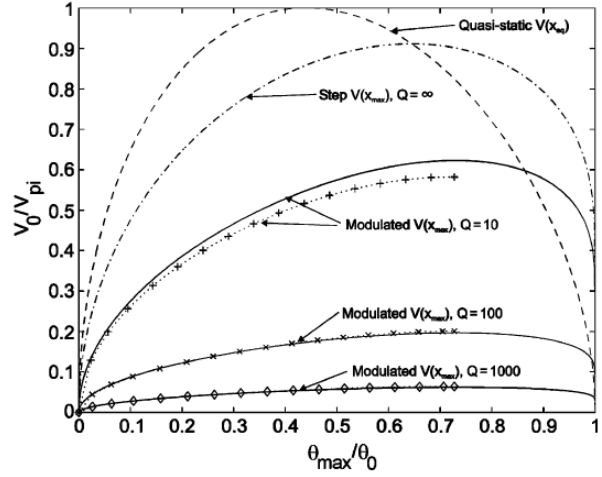

Fig. 8. Numerical and analytical curves of the modulated voltage required for particular limit cycle amplitudes for torsional systems with quality factors of 10, 100, and 1000. The analytical solutions from (33) are the solid lines. The numerical simulation results are given by the data points. For $Q = 10$, the numerical and analytical solution show some discrepancy due to the sinusoidal motion assumption used in the analytical derivation. For comparison, the quasi-static equilibrium curve (5) and the step response curve (18) are also plotted. The peak of each curve defines that curve's pull-in voltage and position.

curves for the parallel-plate actuator's response to the modulated voltage for quality factors of 10, 100, and 1000. The quasi-static and ideal (no damping) step response curves are also included for comparison.

B. Modulated Voltage System Response—Torsional Case

We now analyze the response of a torsional electrostatic actuator to an applied voltage that follows the rule given in (22). The analysis for this case follows the same approach for the parallel-plate case. The energy dissipated is found indirectly by combining the definition of the quality factor [see (25)] of the system with the energy stored in the system at the limit cycle. The energy stored at the limit cycle is calculated at the peak amplitude of the oscillation ($\theta_{\max}$), when all the energy is stored as elastic potential energy. The equation for the total stored energy is

$$E_{\text{stored}} = \frac{1}{2}k\theta_{\max}^2. \tag{31}$$

The energy injected over one oscillation at the limit cycle is

$$E_{\text{injected}} = \int_{-\theta_{\max}}^{\theta_{\max}} \frac{\epsilon w V_0^2}{2\theta^2}\left[\frac{L\theta}{d_0 - L\theta} + \ln\left(1 - \frac{L\theta}{d_0}\right)\right]d\theta$$

$$= -\frac{\epsilon w V_0^2}{2\theta_{\max}}\ln\left(1 - \frac{L^2\theta_{\max}^2}{d_0^2}\right). \tag{32}$$

By combining (23), (25), (31), and (32), the solution for the voltage required for a given limit cycle is found to be

$$V_0 = \sqrt{-\frac{2\pi k\theta_{\max}^3}{\epsilon w Q \ln\left(1 - \frac{L^2\theta_{\max}^2}{d_0^2}\right)}}. \tag{33}$$

The maximum of this function gives the pull-in point of the torsional actuator. Calculating the maximum of (33) numerically indicates that the pull-in limit cycle amplitude is

$$\theta_{\max}^* \approx 0.731\theta_0 \tag{34}$$

which corresponds to a modulated pull-in voltage of

$$V_{mpi} \approx \sqrt{3.21\frac{kd_0^3}{\epsilon w Q L^3}}. \tag{35}$$

The ratio of the modulated pull-in voltage to the quasi-static pull-in voltage gives

$$\frac{V_{mpi}}{V_{pi}} \approx 1.97\sqrt{\frac{1}{Q}}. \tag{36}$$

Fig. 8 shows the effect of the quality factor on the limit cycle curves and pull-in points versus the quasi-static equilibrium curve and the system step response. The modulated voltage leads to significant reductions in the voltage requirements for pull-in of the torsional electrostatic actuator, very much like the parallel-plate actuator.

V. DISCUSSION

In torsional and parallel-plate modulated pull-in and step pull-in, the quality factor of the system is the key parameter affecting the decrease in required actuation voltage. Fig. 9 shows the effect of the quality factor on the ratio of the dynamic pull-in voltage (step and modulated) with the quasi-static pull-in voltage for the parallel-plate case. The torsional case has virtually the same dependence on quality factor as the
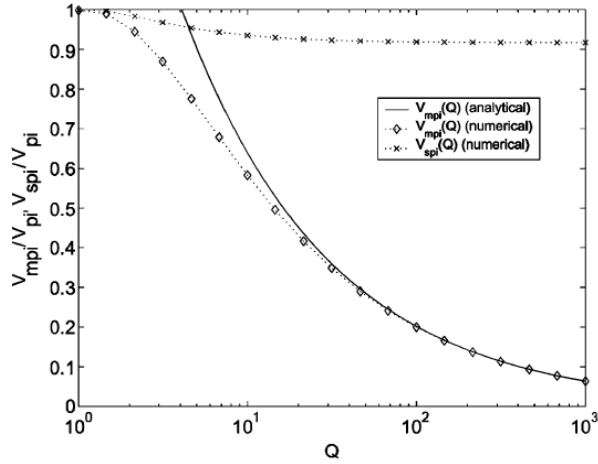
Fig. 9. V_{spi} and V_{mpi} as a function of the quality factor for a parallel-plate electrostatic actuator. For all values of Q greater than one, the modulated pull-in voltage is less than the step pull-in voltage. (The torsional system has an almost identical dependence on Q.)
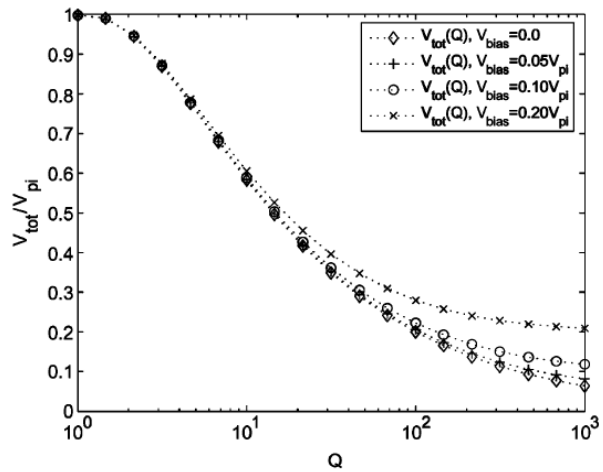

Fig. 10. Numerical analysis of a closed-loop parallel-plate implementation with a dc bias voltage applied showing the total required voltage for pull-in as a function of quality factor. The total voltage is the sum of the bias voltage and the amplitude of the modulated voltage signal. (The torsional system has an almost identical dependence on Q.)

parallel-plate case (the difference between the two cases is $<1.5\%$). It is interesting to note that for all damping levels the modulated pull-in voltage is less than or equal to the step pull-in voltage.

The waveform used in the modulated pull-in analysis provides the greatest transfer of energy and, hence, the lowest pull-in voltage of any waveform in a voltage limited situation; however, in principle any waveform that provides a net positive injection of energy with each cycle could be used. These alternative waveforms also lead to a decrease in the voltage level required for pull-in compared with the quasi-static case.

Torsional electrostatic actuators commonly have two fixed electrodes in symmetrically opposite positions, such that the movable electrode can be pulled-in by rotating in either the positive or negative θ directions [1]. In fact, some parallel-plate actuators have also been fabricated with top and bottom fixed electrodes, enabling two pulled-in positions as well [16]. For electrostatic switches with two opposing fixed electrodes, the modulated pull-in performance can be enhanced by applying a modulated voltage to both fixed electrodes. This allows energy to be input throughout the entire mechanical oscillation and would lead to a further decrease in the modulated pull-in voltage by a factor of $1/\sqrt{2}$ (for fixed electrodes that are symmetrically located relative to the moving electrode).

A. Practical Limitations of a Modulated Pull-In System

In the analysis of modulated pull-in of parallel-plate and torsional actuators, ideal feedback control of the system was assumed [see (22)]. In practice, there are a number of physical limitations that will diminish the performance of the modulated pull-in technique. In this section, we analyze the physical limitations that have the greatest potential impact and that are common to most parallel-plate and torsional electrostatic actuator systems.

Fundamentally, there are two ways to implement a modulated pull-in system. The first method utilizes a feedback control system where the sign of the velocity is sensed by some means which would then control the applied voltage. The second method is open-loop control. There are unique physical limitations to both techniques.

In a feedback control implementation, many sensing techniques could be used, including capacitive, piezoresistive, piezoelectric, or optical sensing. Capacitive sensing is the most likely candidate since no additional sensing structure needs to be put in place, as opposed to the other sensing methods. In fact, this kind of capacitive feedback control system for an electrostatic system has already been developed for MEMS filters and oscillators [17]–[20]. For these devices, the operational goal is to simply resonate, i.e., achieve a limit cycle. To achieve pull-in with a similar circuit requires that the gain of the feedback loop be increased above the level that results in a limit cycle.

The voltage level required to achieve pull-in by a capacitive feedback control circuit implementation is higher than that predicted by the ideal case discussed in Section IV. Capacitive sensing of motional current typically requires a dc bias voltage applied to the parallel plates, which causes a certain amount of electrostatic softening and a reduction of the total pullback force of the mechanical system. A secondary limitation of capacitive feedback control, or any other feedback implementation, is the effect of the time delay in the control loop.

The effect of a dc bias voltage on the performance of the parallel-plate system is shown in Fig. 10. The torsional system has a virtually identical dependence on Q. For these simulations, the applied voltage is
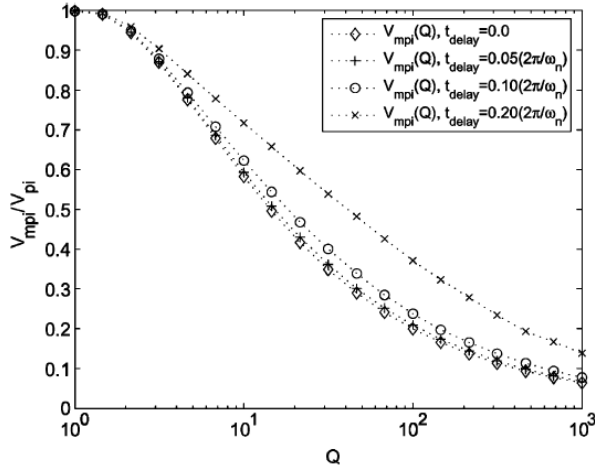
$$V_{tot} = V_{mpi} + V_{\text{bias}} \qquad (37)$$

Fig. 11. Numerical simulation of V_{mpi} as a function of quality factor for a closed-loop parallel-plate system with a delay in the feedback signal. (The torsional system has an almost identical dependence on Q.)
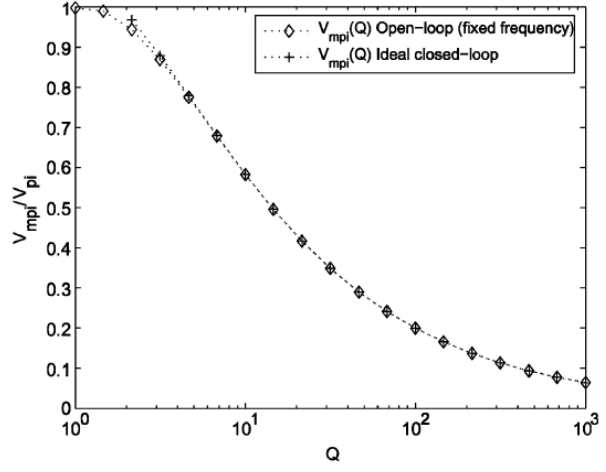

Fig. 12. V_{mpi} for a fixed frequency, open-loop implementation compared with the ideal system discussed in Section IV-A as a function of the quality factor for a parallel-plate electrostatic actuator. For all quality factors greater than five, the fixed frequency implementation performs as well as the ideal closed-loop implementation. (The torsional system has an almost identical dependence on Q.)

where V_{bias} is the dc bias voltage. In the analysis, V_{bias} is set at some fraction of the quasi-static pull-in voltage V_{pi}.

It can be seen from Fig. 10 that the bias voltage causes little deviation of V_{tot} from the ideal modulated pull-in voltage for systems with low and intermediate quality factors. For systems with high quality factors, the bias voltage becomes the dominating voltage component.

The effect of time delay on the modulated pull-in voltage is shown in Fig. 11 for the parallel-plate system. The torsional system has essentially identical behavior. These simulations were performed with a time delay that is some fraction of the time of one free oscillation of the mechanical system. Although the effect of the time delay is strongest for systems with intermediate quality factors, the relative change in V_{mpi}/V_{pi} is largest at high-quality factors. This results from the electrostatic damping effect being dependent on both the applied voltage level and the number of oscillations required until pull-in occurs.

The actual bias voltage and time delay of any particular system will depend on the characteristics of that system; however, these results indicate that even with a rather large bias voltage or time delay, significant reductions in the pull-in voltage can still be achieved using a modulated pull-in signal.

The open-loop implementation has some significant advantages over the closed-loop implementation. Open-loop systems do not suffer from the effects of time delays or bias voltages. They also are simpler to implement than closed-loop systems.

For the simulations of the open-loop implementation, a constant-frequency signal is applied to achieve pull-in.[4] Fig. 12 shows the modulated pull-in voltage for a parallel-plate system as a function of quality factor. The torsional system's modulated pull-in voltage has a virtually identical dependence on quality

[4]An open-loop control circuit can potentially have a nonconstant signal frequency; however, optimizing the frequency modulation of the circuit to match the system resonant frequency shift during operation would be challenging.
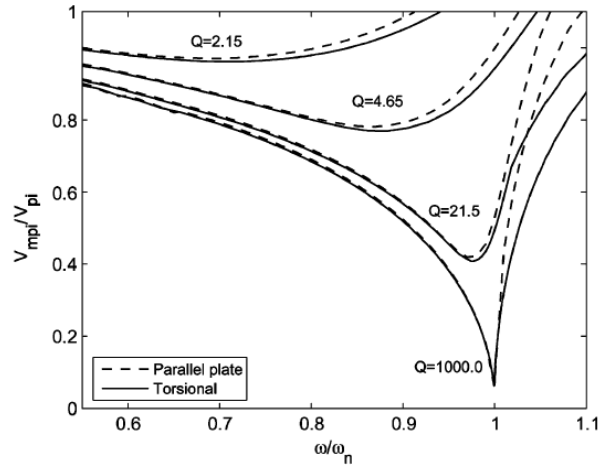

Fig. 13. Numerical analysis of V_{mpi} for a fixed frequency, open-loop control implementation as a function of the signal frequency for both parallel-plate and torsional electrostatic actuators for a range of quality factors.

factor. It is seen that for quality factors greater than about five, the open-loop implementation performance is essentially identical to the ideal performance described in Section IV.

To achieve this level of performance, the frequency of the applied voltage signal needs to be carefully set. Due to the electrostatic nonlinearities, the optimum actuation signal frequency is generally not at the mechanical resonant frequency. Fig. 13 shows the modulated pull-in voltage required as a function of the signal frequency normalized to the natural frequency of the mechanical system for parallel-plate and torsional systems with a range of quality factors. The optimal signal frequency is shifted away from the mechanical natural frequency due to the shift in the system resonant frequency resulting from the applied voltage. As expected, the very high-quality factor

systems, which require small modulated voltage signals for pull-in, have the smallest resonant frequency shifts.

One of the most significant drawbacks to the open-loop implementation is that the frequency of the voltage signal needs to be carefully trimmed to each individual device. High-quality factor systems would require especially fine trimming. Open-loop implementations are also susceptible to any kind of drift in the system that would shift the optimal signal frequency away from the set signal frequency.

One final physical limitation that affects both open-loop and closed-loop implementations is the voltage required to hold the switch in the pulled-in state. The modulated pull-in technique can lead to pull-in voltages that are significantly lower than the quasi-static pull-in voltage typically used as a minimum actuation voltage. This reduction in actuation voltage needs to be balanced with the thickness of the insulating layer between the two electrodes for isolation. If the insulating film between the electrodes is too thick, it is possible that the modulated pull-in voltage level will be lower than the hold voltage of the system. In this case, the hold voltage becomes the limiting voltage level of the system [13].

VI. Conclusion

In this paper, we have shown that the dynamic nature of parallel-plate and torsional electrostatic actuators can have a significant impact on the voltage needed to pull-in the actuator. In particular, it was shown that for the ideal case of no damping an applied step voltage can achieve pull-in with only 91.9% of the quasi-statically predicted pull-in voltage for parallel-plate actuators, and for torsional actuators only 91.2% of the quasi-statically predicted pull-in voltage is required. It was also shown that by applying a voltage that is modulated at the mechanical resonance of the actuator, significant decreases in voltage levels needed for pull-in can be achieved. For instance, for a system with a quality factor of 1000, the voltage level required for pull-in is less than 10% of the quasi-static pull-in voltage for both parallel-plate and torsional actuators. The decrease in pull-in voltage for both the step and modulated input voltages is strongly dependent on the damping in the system.

The impact of these dynamic pull-in techniques could be very significant for electrostatic parallel-plate and torsional actuators used as switching structures in microwave, RF, or optical MEMS applications. To create reliable switching structures, it has been necessary to have a high-actuation voltage, much higher than levels used by integrated circuits. By utilizing these dynamic pull-in techniques, low-voltage actuation can be achieved without sacrificing mechanical stiffness and reliability. This would allow direct integration of reliable MEMS switching structures into standard integrated circuits without the need of voltage up-converters. In addition, electrostatic MEMS filters and oscillators, which need to avoid pull-in resulting from modulated actuation, can also benefit this dynamic pull-in analysis.

References

[1] R. Sattler, F. Plötz, G. Fattinger, and G. Wachutka, "Modeling of an electrostatic torsional actuator: demonstrated with an RF MEMS switch," *Sens. Actuators A, Phys.*, vol. 97–98, pp. 337–346, April 2002.

[2] G. N. Nielson, "Micro-Opto-Mechanical Switching and Tuning for Integrated Optical Systems," Ph.D. dissertation, Dept. Mech. Eng., MIT, Cambridge, MA, 2004.

[3] O. Solgaard, S. F. A. Sandejas, and D. M. Bloom, "Deformable grating optical modulator," *Opt. Lett.*, vol. 17, no. 9, pp. 688–690, May 1992.

[4] G. A. Feather and D. W. Monk, "The digital micromirror device for projection display," in *Proc. IEEE 7th Annu. Int. Conf. Wafer Scale Integration*, 1995, pp. 43–51.

[5] G. M. Rebeiz, *RF MEMS Theory, Design, and Technology*. Hoboken, NJ: Wiley, 2003.

[6] J. B. Muldavin and G. M. Rebeiz, "Nonlinear electro-mechanical modeling of MEMS switches," in *Proc. IEEE MTT-S Int. Microwave Symp. Digest*, 2001, vol. 3, pp. 2119–2122.

[7] L. M. Castañer and S. D. Senturia, "Speed-energy optimization of electrostatic actuators based on pull-in," *IEEE J. Microelectromech. Syst.*, vol. 8, no. 3, pp. 290–298, Sep. 1999.

[8] J. B. Starr, "Squeeze-film damping in solid-state accelerometers," in *Proc. Solid-State Sensor and Actuator Workshop (Tech. Dig.)*, 1990, pp. 44–47.

[9] T. Veijola, H. Kuisma, and J. Lahdenpera, "Model for gas film damping in a silicon accelerometer," in *Int. Conf. Solid-State Sensor and Actuators (Transducers '97)*, 1997, vol. 2, pp. 1097–1100.

[10] S. D. Senturia, *Microsystem Design*. Norwell, MA: Kluwer, 2001.

[11] M. I. Younis and A. H. Nayfeh, "A study of the nonlinear response of a resonant microbeam to an electric actuation," *Nonlinear Dyn.*, vol. 31, no. 1, pp. 91–117, Jan. 2003.

[12] E. K. Chan, E. C. Kan, R. W. Dutton, and P. M. Pinsky, "Nonlinear dynamic modeling of micromachined microwave switches," in *Proc. IEEE MTT-S Int. Microwave Symp. Digest*, 1997, pp. 1511–1514.

[13] Y. Choi, K. Kim, and M. G. Allen, "A magnetically actuated, electrostatically clamped high current MEMS switch," in *Proc. ASME 2001 Int. Mechanical Engineering Congr. Exposition, MEMS*, 2001, vol. 3, pp. 83–87.

[14] S. R. Bhalotra, J. D. Mansell, H. L. Kung, and D. A. B. Miller, "Parallel-plate MEMS mirror design for large on-resonance displacement," in *Proc. IEEE/LEOS 2000 Int. Conf. Optical MEMS*, 2000, pp. 93–94.

[15] J. M. T. Thompson and H. B. Stewart, *Nonlinear Dynamics and Chaos*, 2nd ed. West Sussex, U.K.: Wiley, 2002.

[16] D. Peroulis, S. P. Pacheco, K. Sarabandi, and L. P. B. Katehi, "Electromechanical considerations in developing low-voltage RF MEMS switches," *IEEE Trans. Microw. Theory Tech.*, vol. 51, no. 1, pp. 259–270, Jan. 2003.

[17] F. D. Bannon, III, J. R. Clark, and C. T.-C. Nguyen, "High-Q HF microelectromechanical filters," *IEEE J. Solid-State Circuits*, vol. 35, no. 4, pp. 512–526, Apr. 2000.

[18] C. T.-C. Nguyen, "Frequency-selective MEMS for miniaturized low-power communication devices," *IEEE Trans. Microw. Theory Tech.*, vol. 47, no. 8, pp. 1486–1503, Aug. 1999.

[19] J. Bienstman, H. A. C. Tilmans, E. J. E. A. Peeters, M. Steyaert, and R. Puers, "An oscillator circuit for electrostatically driven silicon-based one-port resonators," *Sens. Actuators A, Phys.*, vol. 52, no. 1–3, pp. 179–186, Mar. 1996.

[20] H. A. C. Tilmans and R. Legtenberg, "Electrostatically driven vacuum-encapsulated polysilicon resonators Part II. Theory and performance," *Sens. Actuators A, Phys.*, vol. 45, no. 1, pp. 67–84, Oct. 1994.

Gregory N. Nielson (S'02–M'03) received the B.S. degree in mechanical engineering from Utah State University, Logan, in 1998 and the M.S. and Ph.D. degrees in mechanical engineering from the Massachusetts Institute of Technology (MIT), Cambridge, in 2000 and 2004, respectively.

He is currently a Truman Fellow at Sandia National Laboratories, Albuquerque, NM. His research interests include the design, modeling, and fabrication of MEMS devices for free space and waveguided optical applications with particular emphasis on integrated photonic devices.

75

George Barbastathis (M'03) was born in Athens, Greece, on January 20, 1971. He received the Electrical and Computer Engineer's degree from the National Technical University of Athens, Athens, Greece, in April 1993 and the M.Sc. and Ph.D. degrees in electrical engineering from the California Institute of Technology, Pasadena, in June 1994 and October 1997, respectively.

After postdoctoral work at the University of Illinois, Urbana-Champaign, he joined the faculty at the Massachusetts Institute of Technology (MIT), Cambridge, in March 1999, where he is currently the Associate Professor of Mechanical Engineering. His research areas are in information photonics, i.e., the use of light and optoelectronics for information processing, with emphasis on sensing, imaging, and interconnects. His research group specializes in 3-D optical systems, such as volume holograms and nonperiodic high-index contrast structures. Another area of research interest is the nanostructured origami 3-D fabrication and assembly method for constructing 3-D nanophotonic elements and other 3-D nanostructures. His past research accomplishments include the holographic method of shift multiplexing, an interferometric corneal topographer, volume holographic confocal microscopy, resonant holography, and the first-ever real-time four-dimensional (spatial and spectral) optical microscope.

Dr. Barbastathis is a member of the Optical Society of America. He is the recipient of the 3M Innovation Award (1999) and the NSF Young Investigator Award (2000), and is presently serving as Topical Editor for the *Journal of the Optical Society of America A (Vision and Image Science)*.

76

Appendix B

**Table B1 Design parameters of the different micromirror device designs.**

device #	mirror poly layer	spring poly layer	mirror plate dimension (µm)	mirror thickness (µm)	spring length (µm)	spring width (µm)	spring thickness (µm)	electrode gap (µm)
1	1	2	20	1	3.5	1	1.5	0.5
2	1	2	20	1	3.5	1.5	1.5	0.5
3	1	2	20	1	5	1	1.5	0.5
4	1	2	20	1	10	1	1.5	0.5
5	1	2	20	1	10	1.5	1.5	0.5
6	1	2	25	1	3.5	1	1.5	0.5
7	1	2	25	1	3.5	1.5	1.5	0.5
8	1	2	25	1	5	1	1.5	0.5
9	1	2	25	1	10	1	1.5	0.5
10	1	2	25	1	10	1.5	1.5	0.5
11	1	2	25	1	3.5	1	1.5	0.5
12	1	2	30	1	3.5	1.5	1.5	0.5
13	1	2	30	1	5	1	1.5	0.5
14	1	2	30	1	10	1	1.5	0.5
15	1	2	30	1	10	1.5	1.5	0.5
16	1	2	30	1	3.5	1.5	1.5	0.5
17	1	2	40	1	3.5	2	1.5	0.5
18	1	2	20	1.5	1.5	2	1.5	0.3
19	1	2	20	1.5	1.5	2	1.5	0.3
20	1	2	20	1.5	5	2	1.5	0.3
21	1	2	20	1.5	5	1.5	1.5	0.3
22	1	2	25	1.5	1.5	2	1.5	0.3
23	1	2	25	1.5	1.5	2	1.5	0.3
24	1	2	25	1.5	3.5	2	1.5	0.3
25	1	2	25	1.5	5	2	1.5	0.3
26	1	2	25	1.5	5	1.5	1.5	0.3
27	1	2	30	1.5	1.5	2	1.5	0.3
28	1	2	30	1.5	1.5	2	1.5	0.3
29	1	2	30	1.5	3.5	2	1.5	0.3
30	1	2	30	1.5	5	2	1.5	0.3
31	1	2	30	1.5	5	1.5	1.5	0.3
32	2	1	40	1.5	1	2	1	0.3

Appendix C

defl vs voltage C:/greg/torsional_mirror/d1/r2
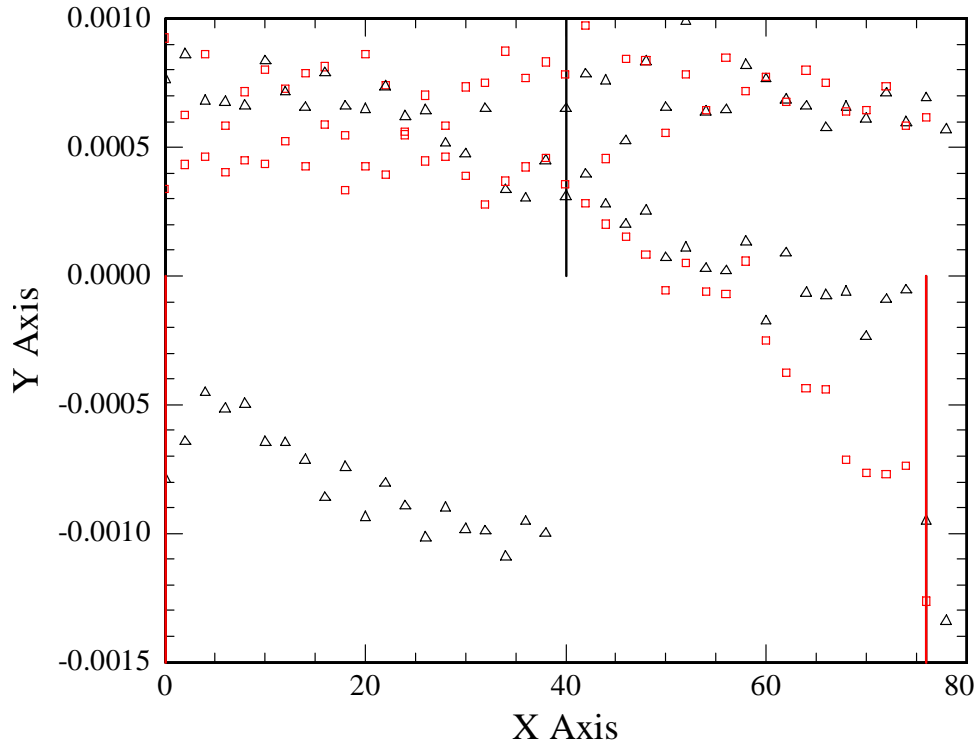
defl vs voltage C:/greg/torsional_mirror/d2/r5

78
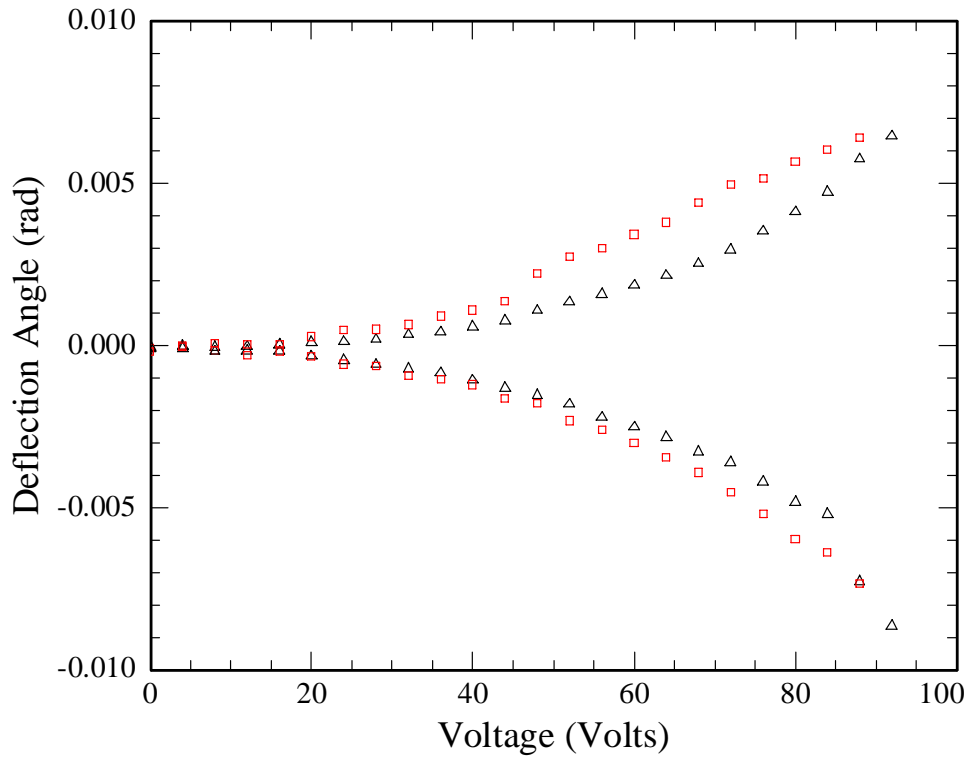
defl vs voltage C:/greg/torsional_mirror/d3/r3
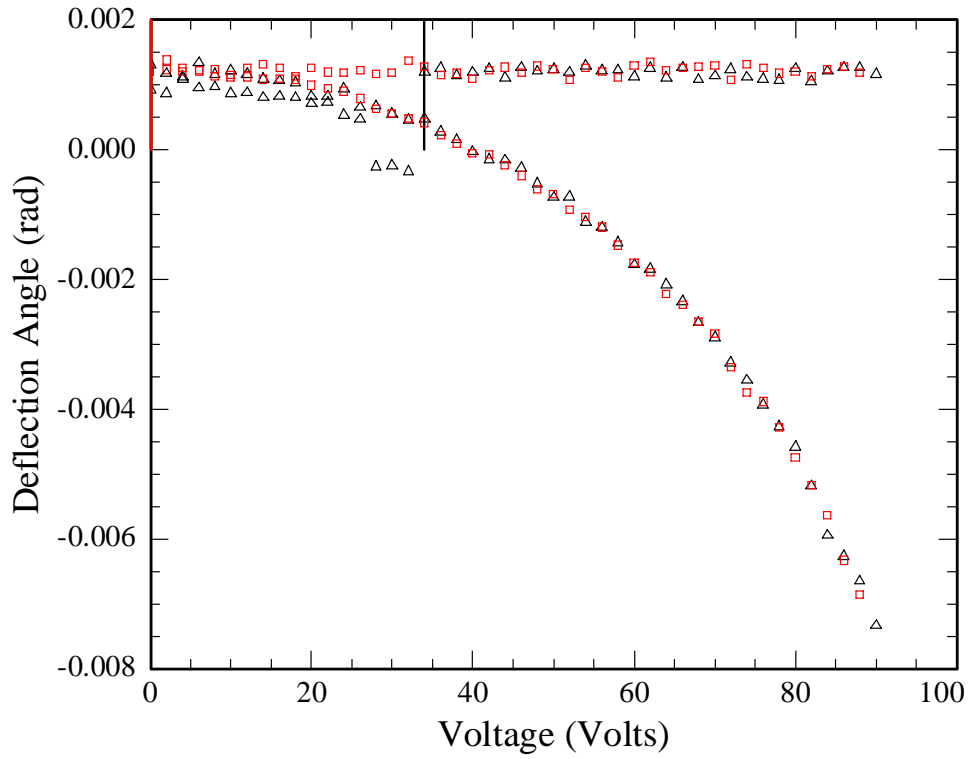
defl vs voltage C:/greg/torsional_mirror/d4/r3
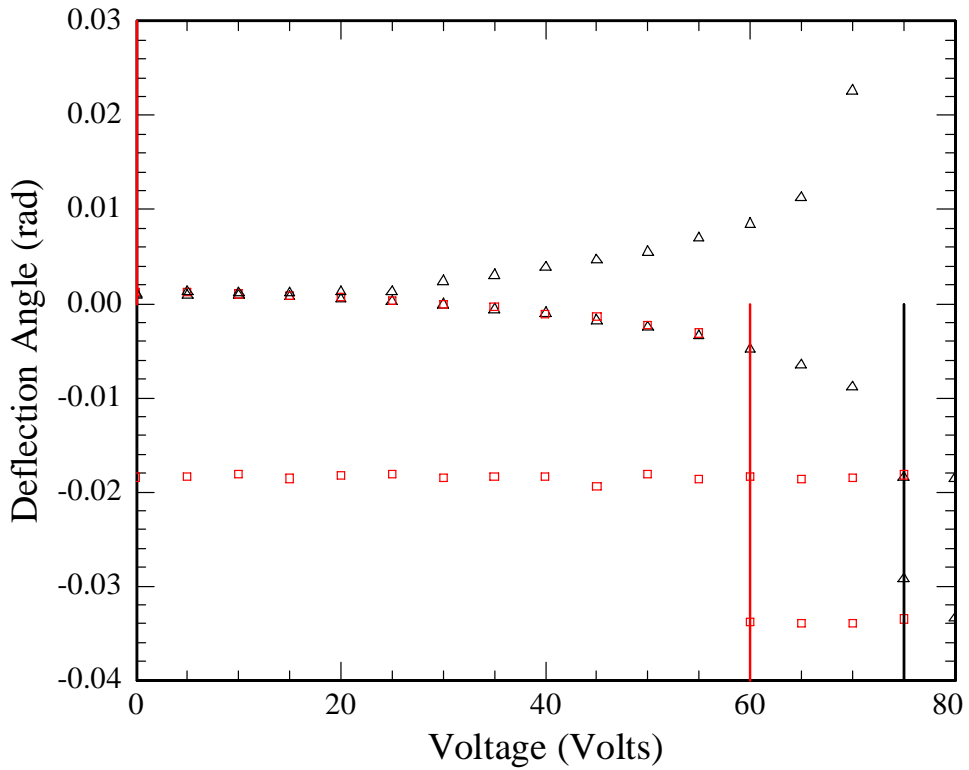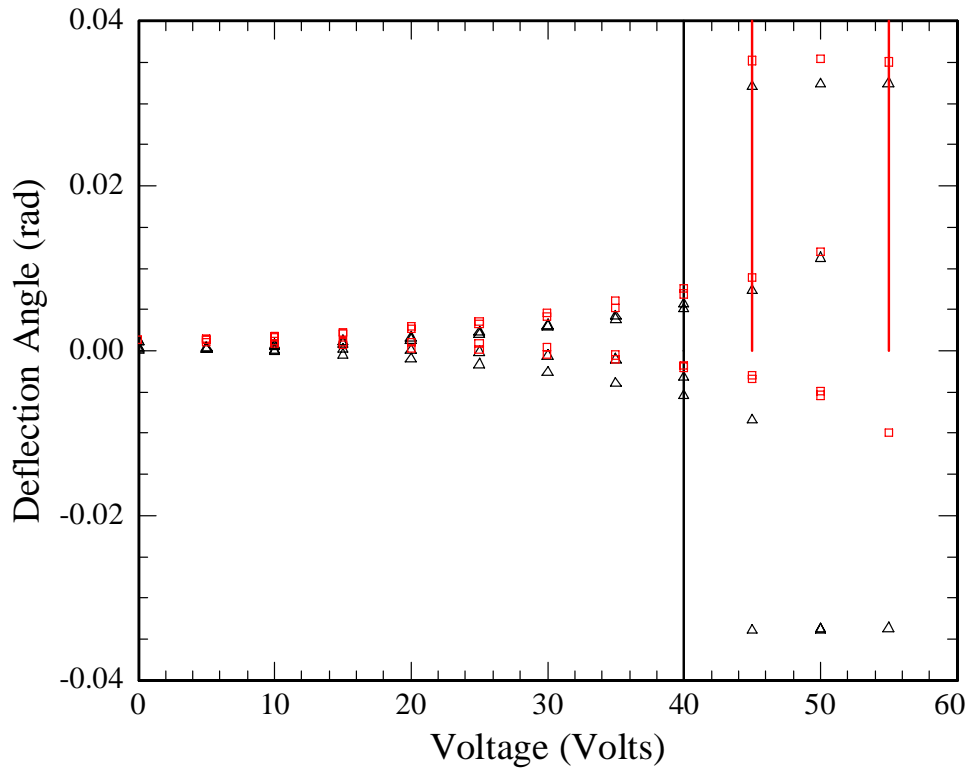
defl vs voltage C:/greg/torsional_mirror/d5/r2
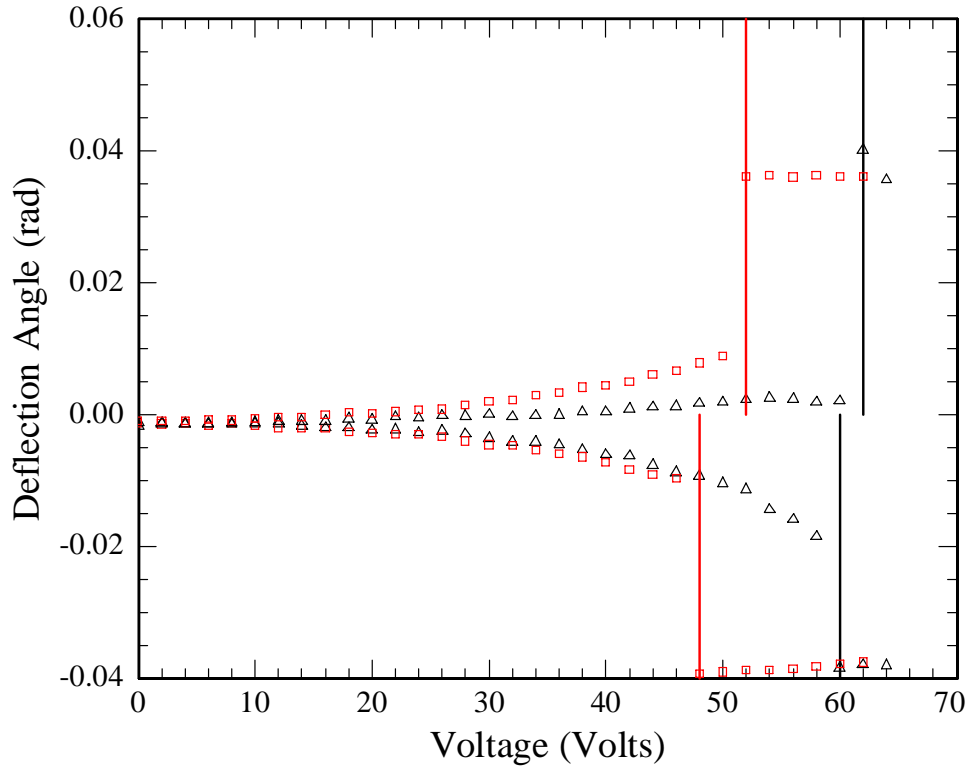
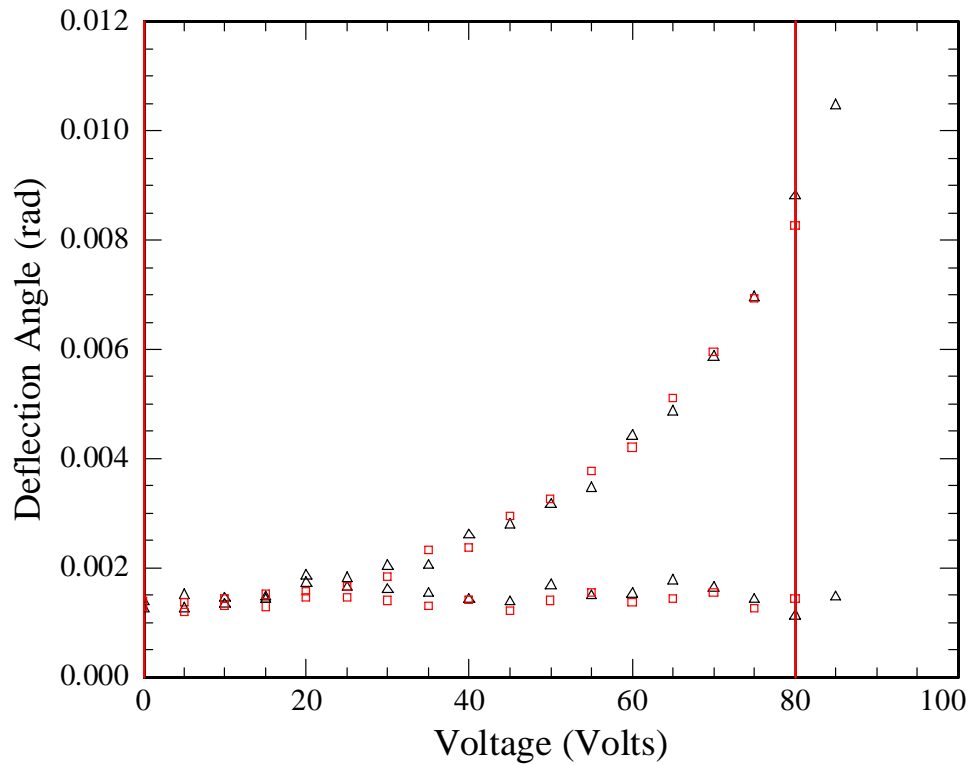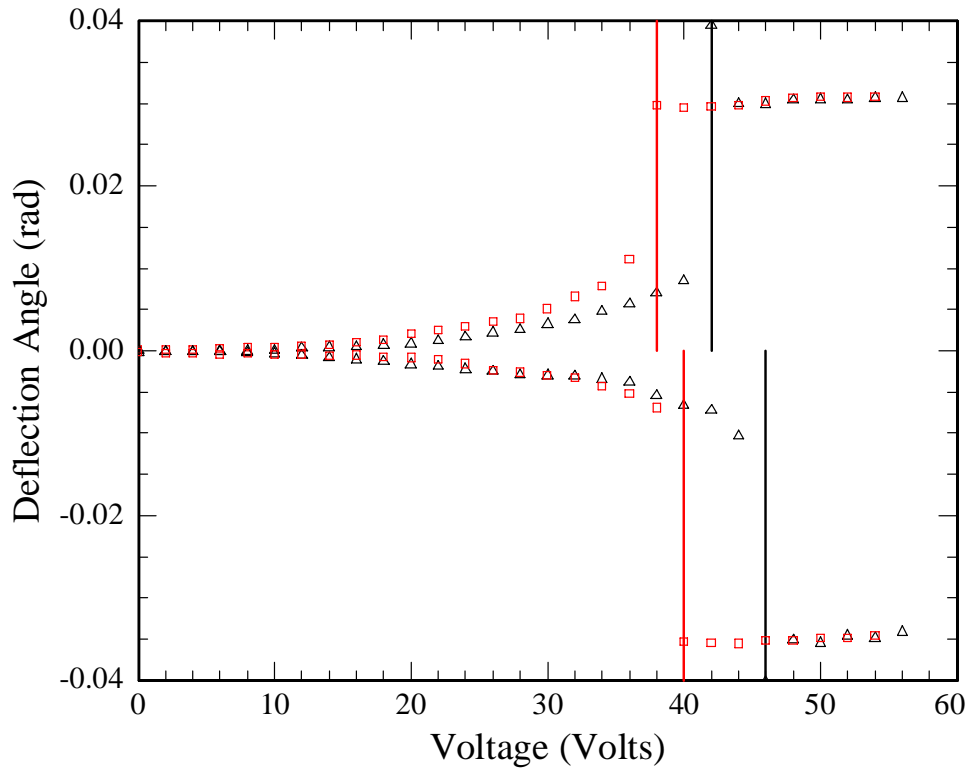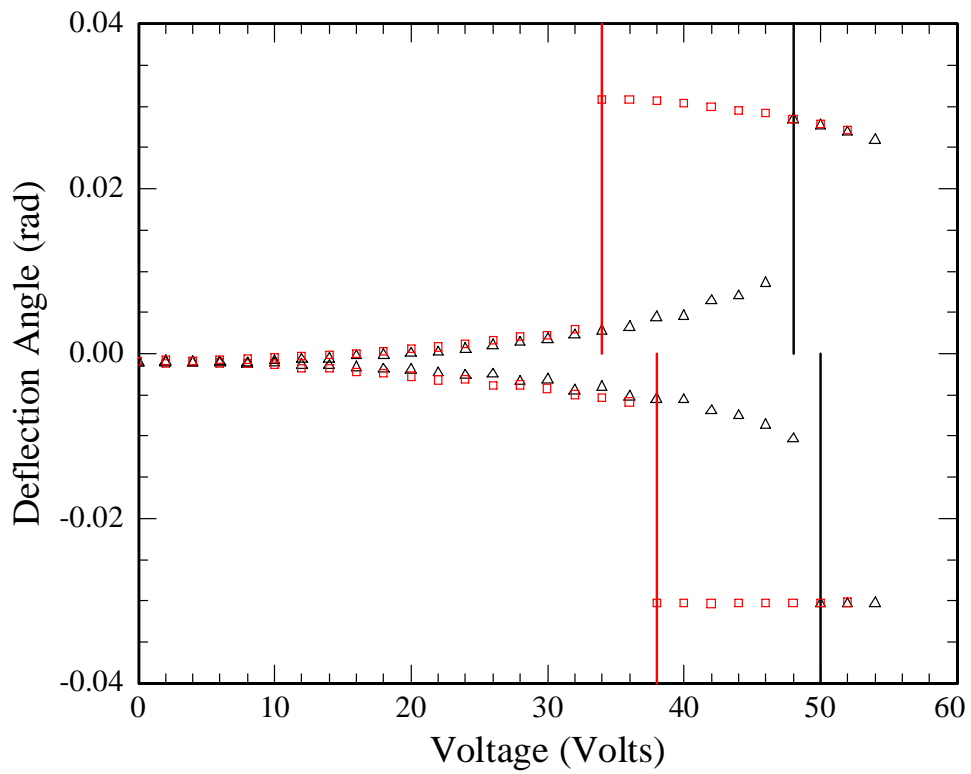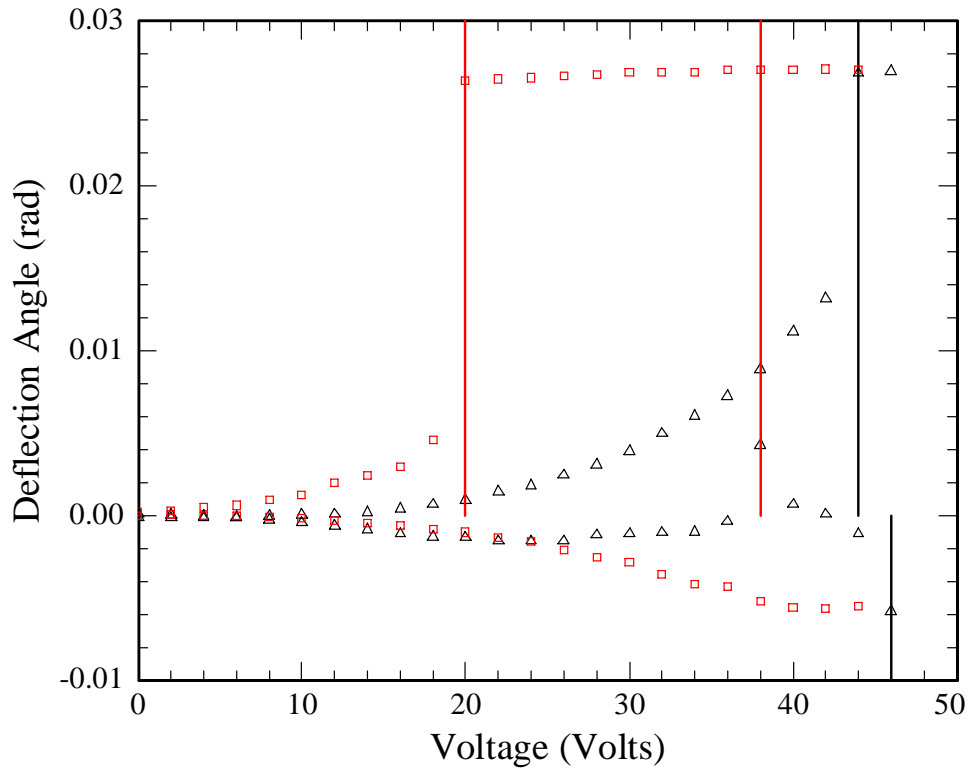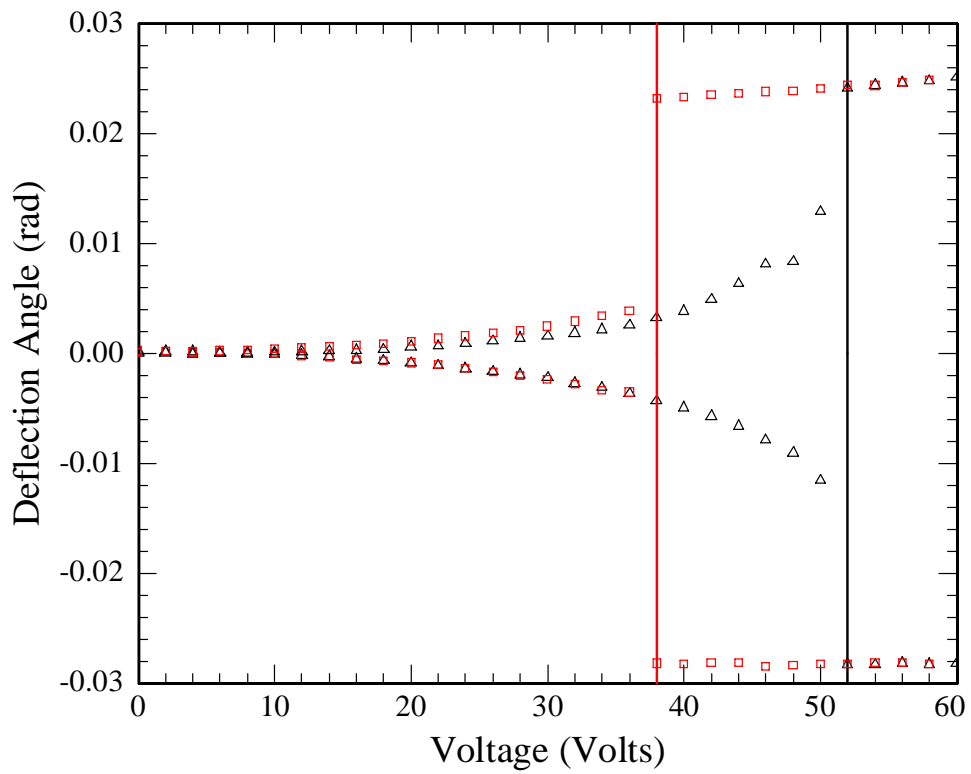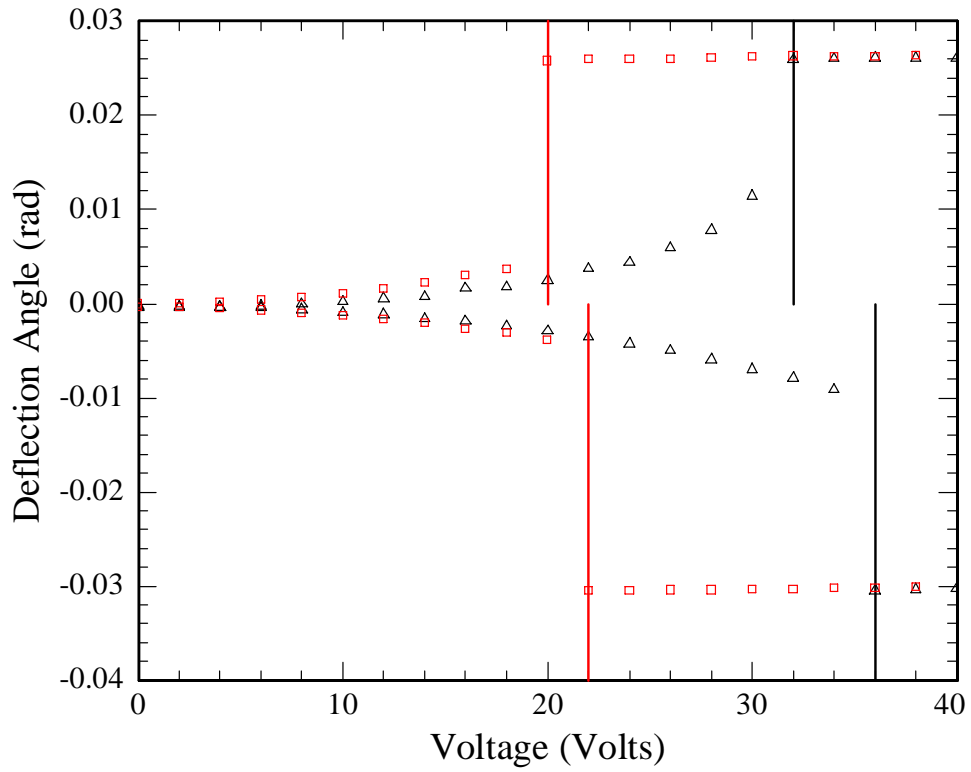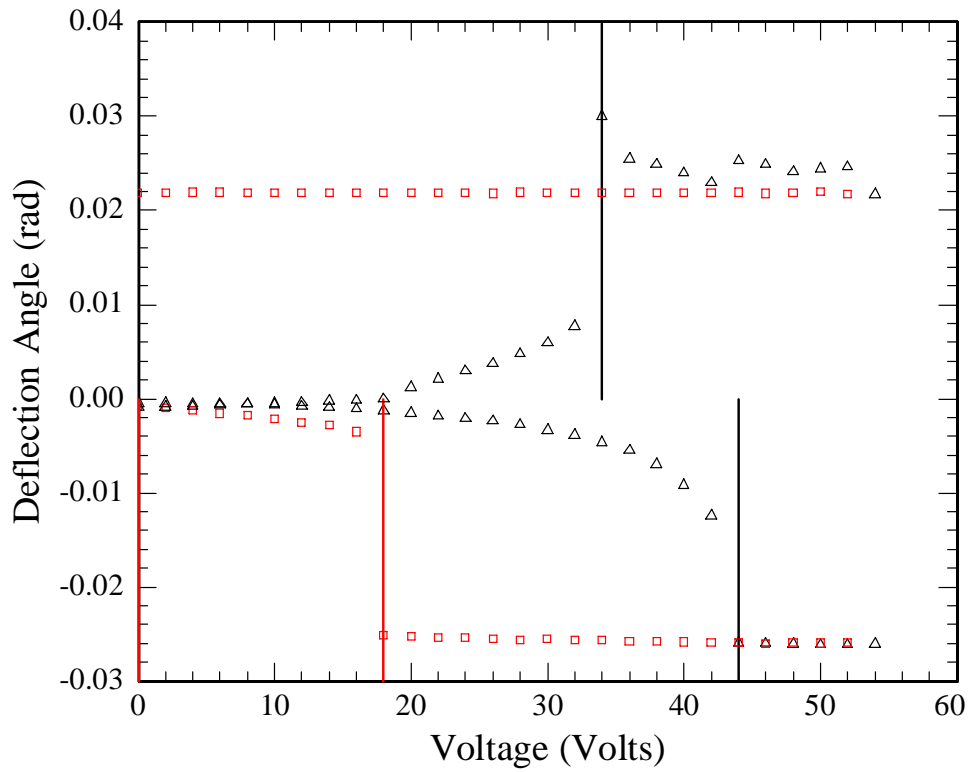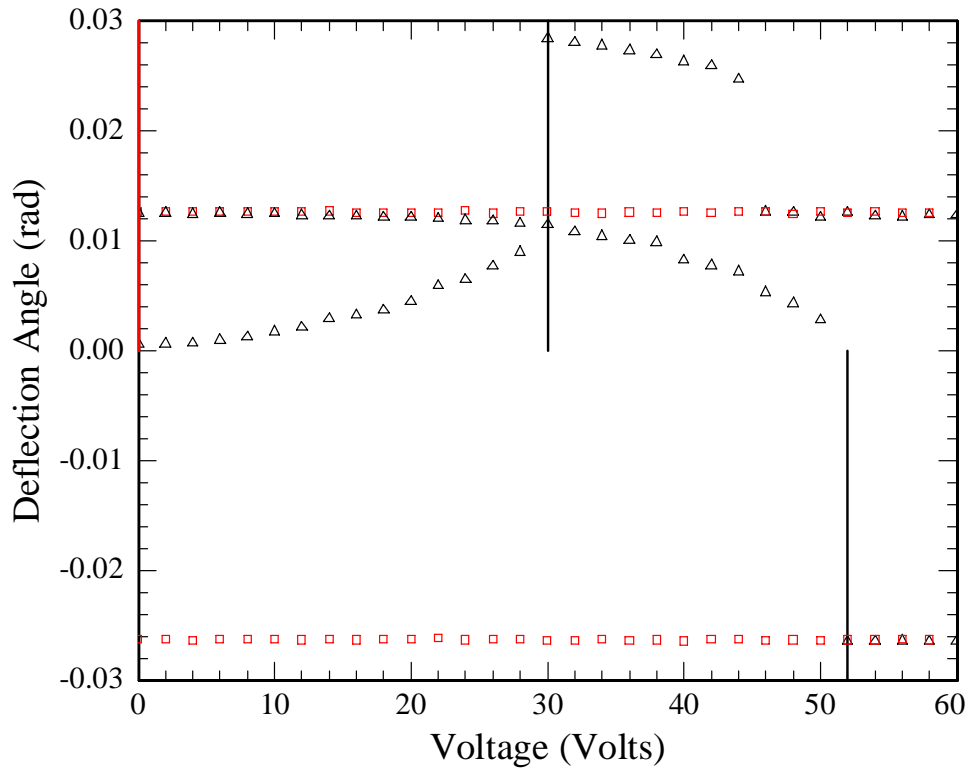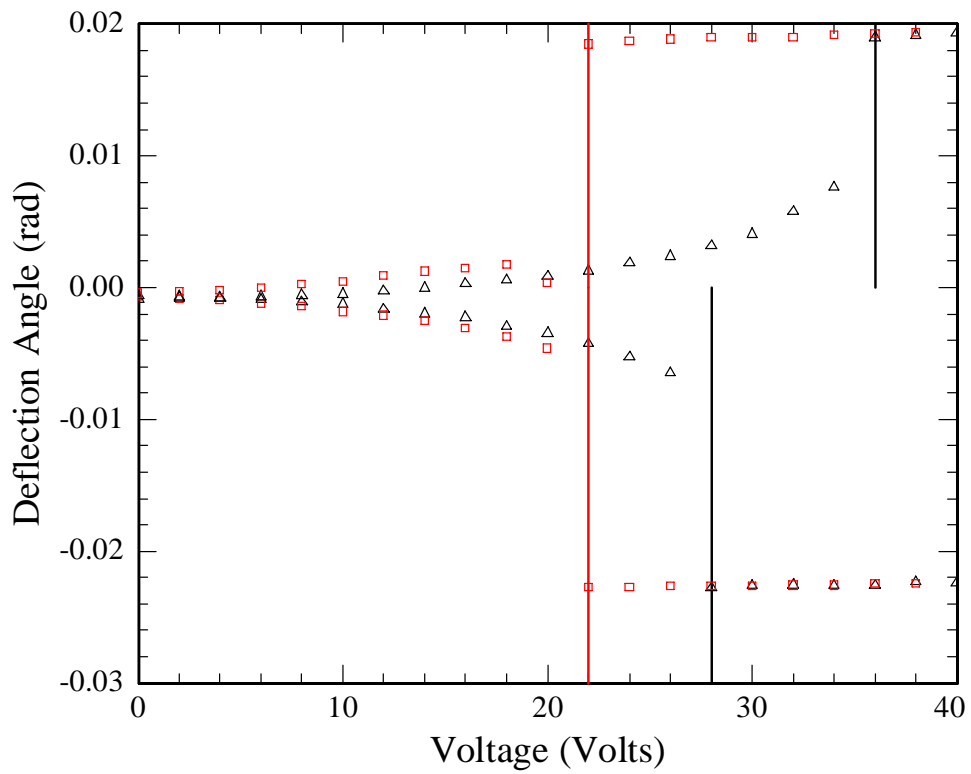## defl vs voltage C:/greg/torsional_mirror/d6/r1
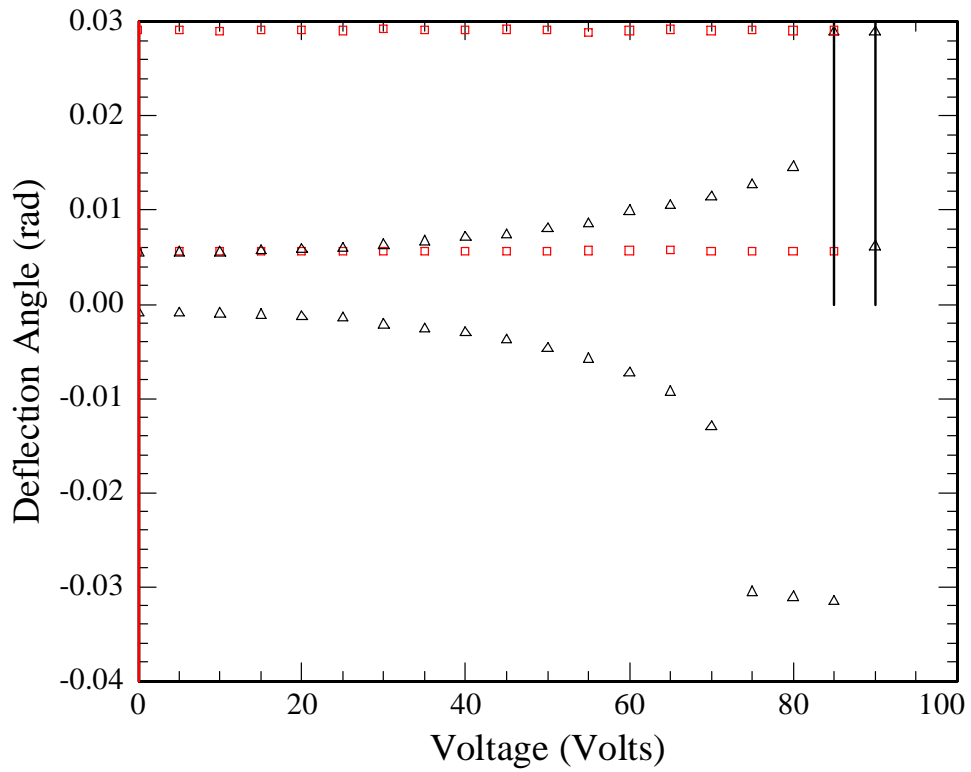
defl vs voltage C:/greg/torsional_mirror/d7

defl vs voltage C:/greg/torsional_mirror/d8/r5

defl vs voltage C:/greg/torsional_mirror/d9/r2

defl vs voltage C:/greg/torsional_mirror/d10/r3

defl vs voltage C:/greg/torsional_mirror/d11/r2

defl vs voltage C:/greg/torsional_mirror/d12/r2

defl vs voltage C:/greg/torsional_mirror/d13/r2
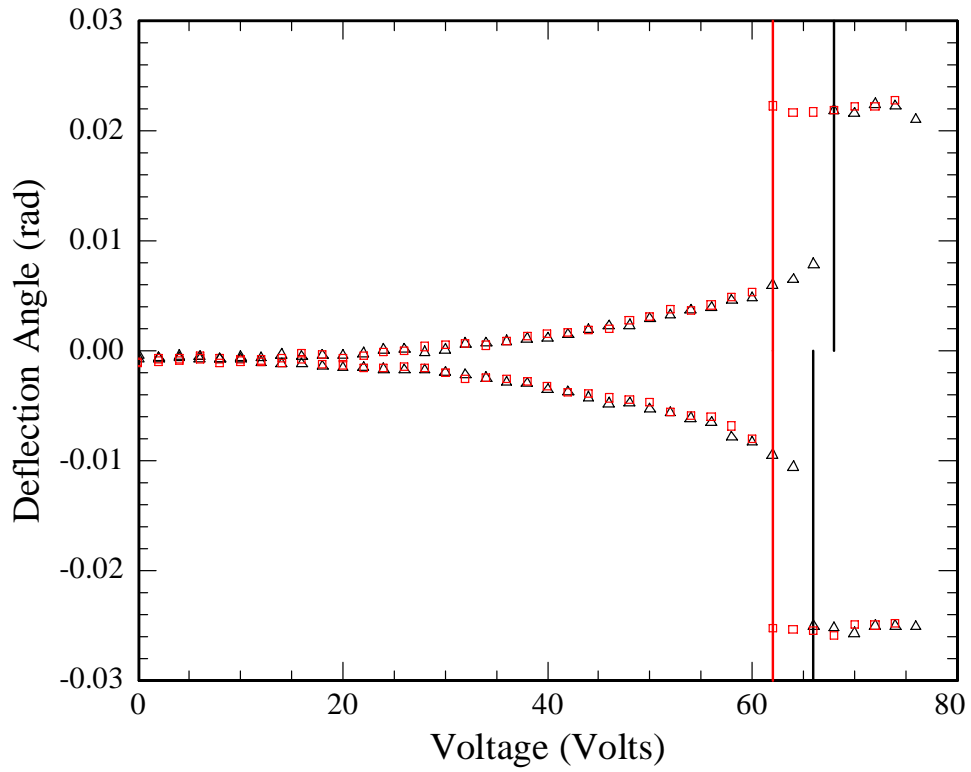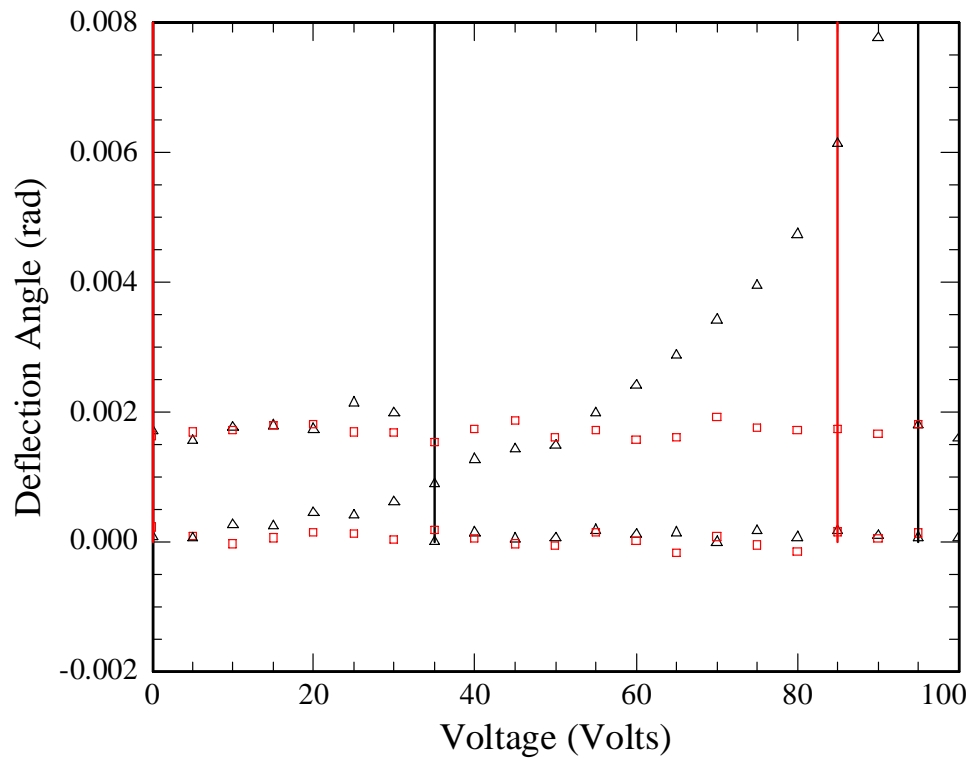
defl vs voltage C:/greg/torsional_mirror/d14/r2

defl vs voltage C:/greg/torsional_mirror/d15

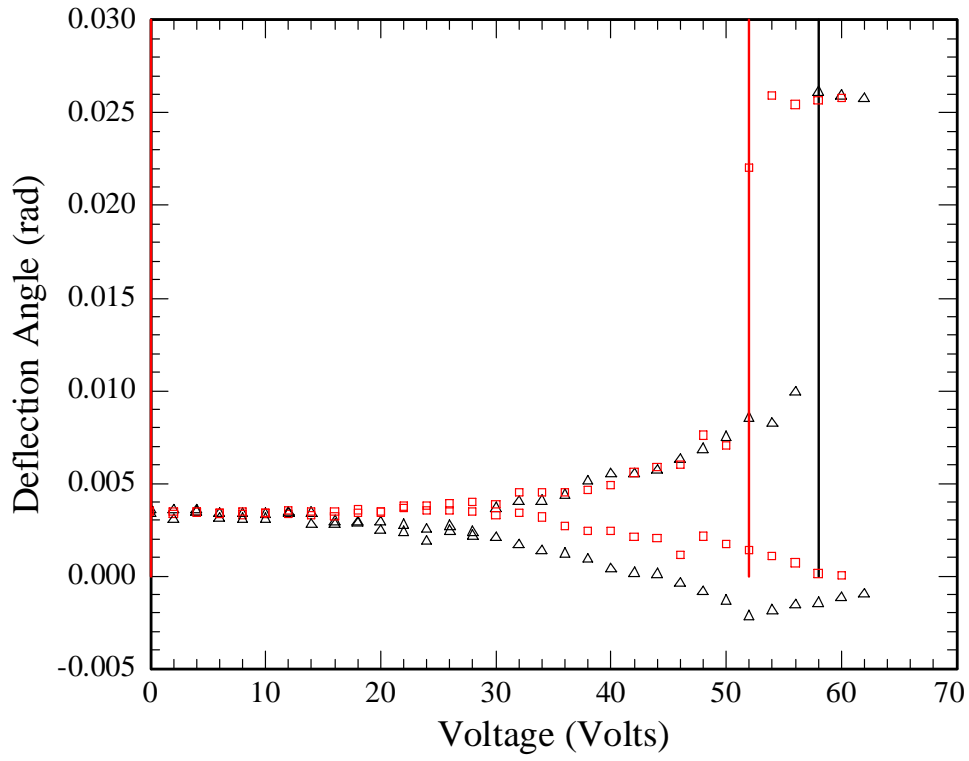defl vs voltage C:/greg/torsional_mirror/d16/r4

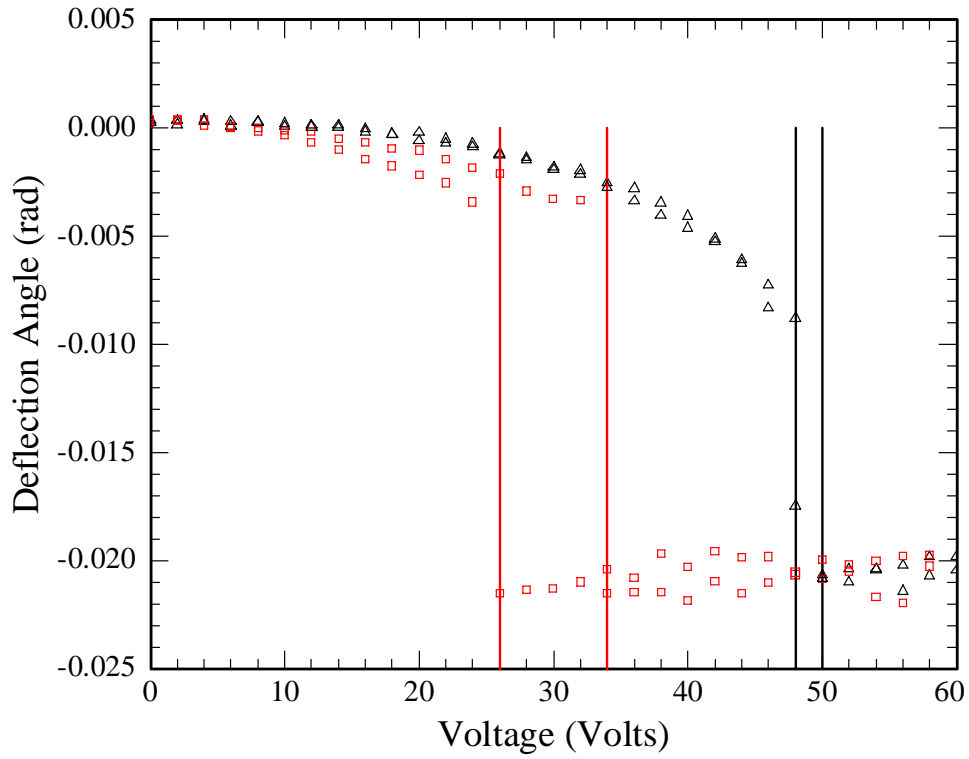## defl vs voltage C:/greg/torsional_mirror/d17/r4

defl vs voltage C:/greg/torsional_mirror/d18/r4

defl vs voltage C:/greg/torsional_mirror/d19/r3

defl vs voltage C:/greg/torsional_mirror/d20/r2

defl vs voltage C:/greg/torsional_mirror/d21/r2

defl vs voltage C:/greg/torsional_mirror/d22/r2

defl vs voltage C:/greg/torsional_mirror/d23/r2

defl vs voltage C:/greg/torsional_mirror/d24/r2

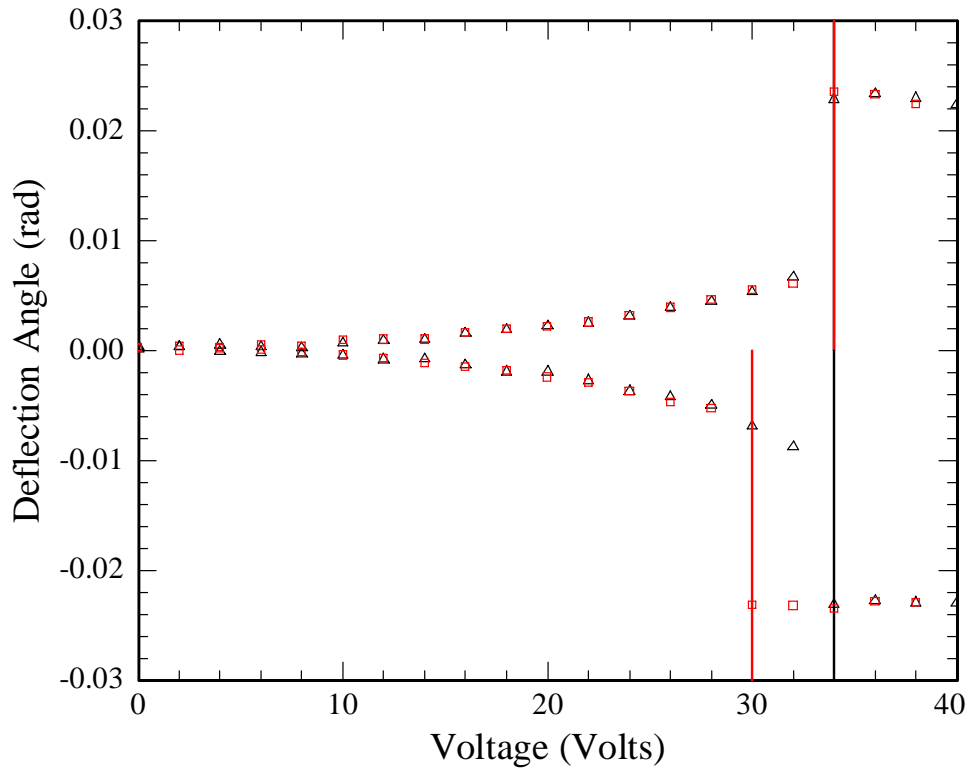## defl vs voltage C:/greg/torsional_mirror/d25/r2

defl vs voltage C:/greg/torsional_mirror/d26/r3
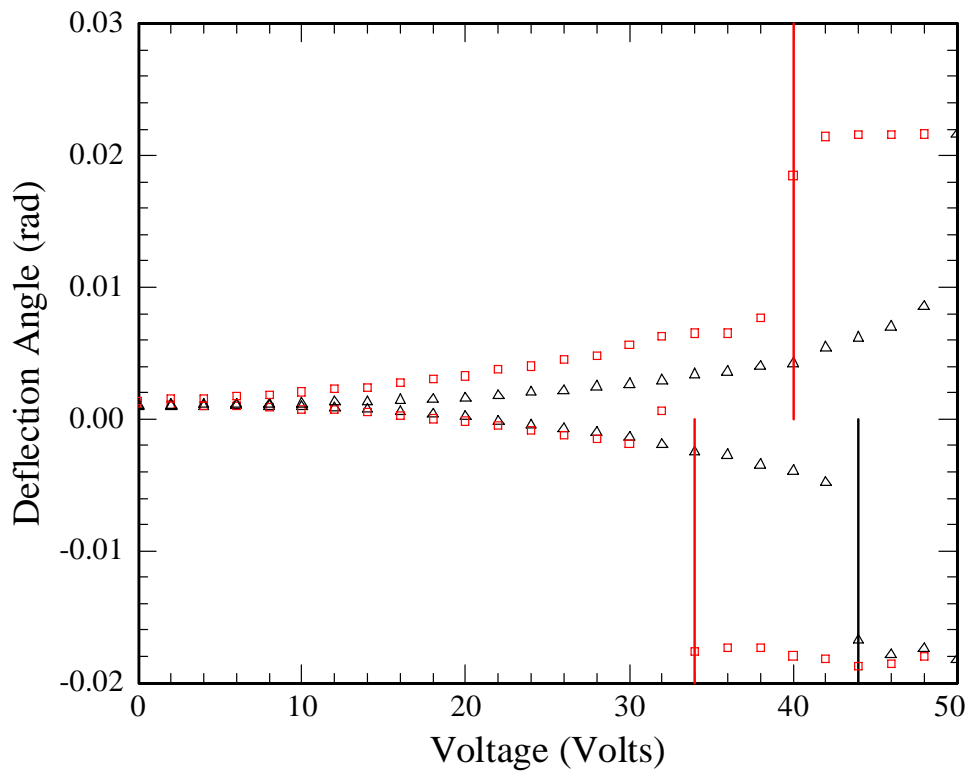
defl vs voltage C:/greg/torsional_mirror/d27/r2

defl vs voltage C:/greg/torsional_mirror/d28/r2

defl vs voltage C:/greg/torsional_mirror/d29/r4
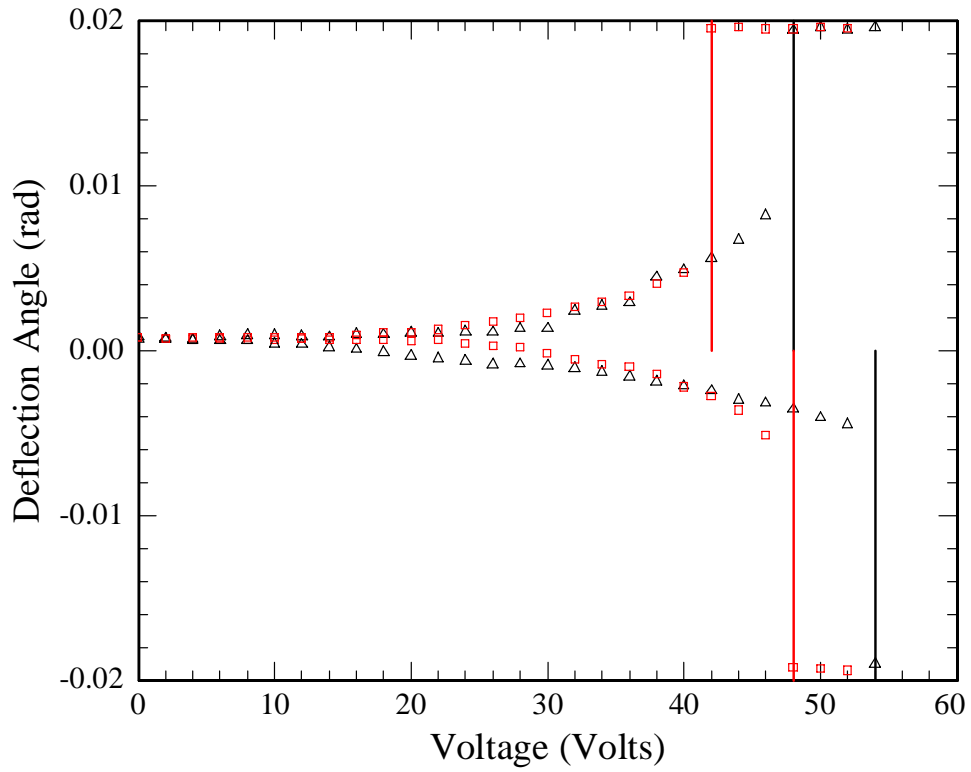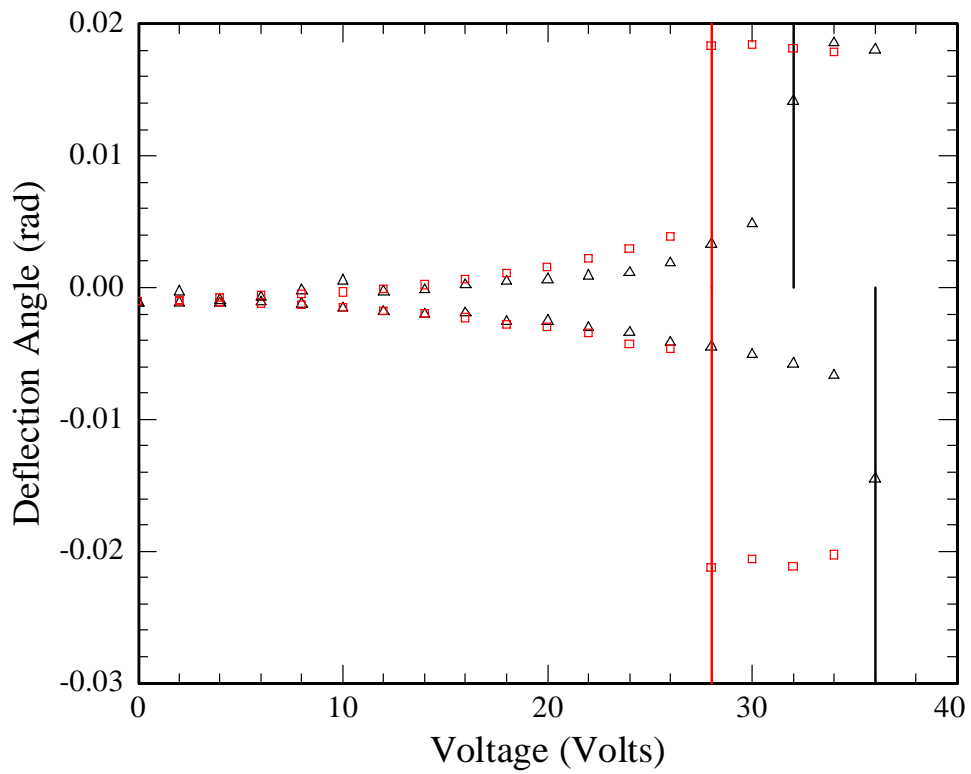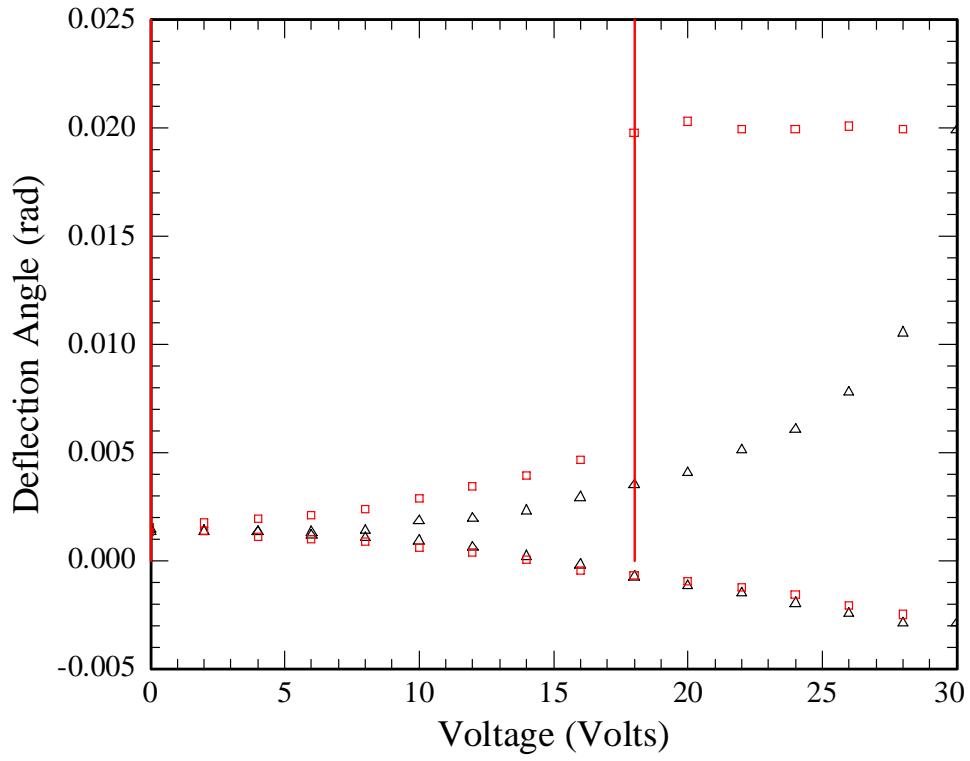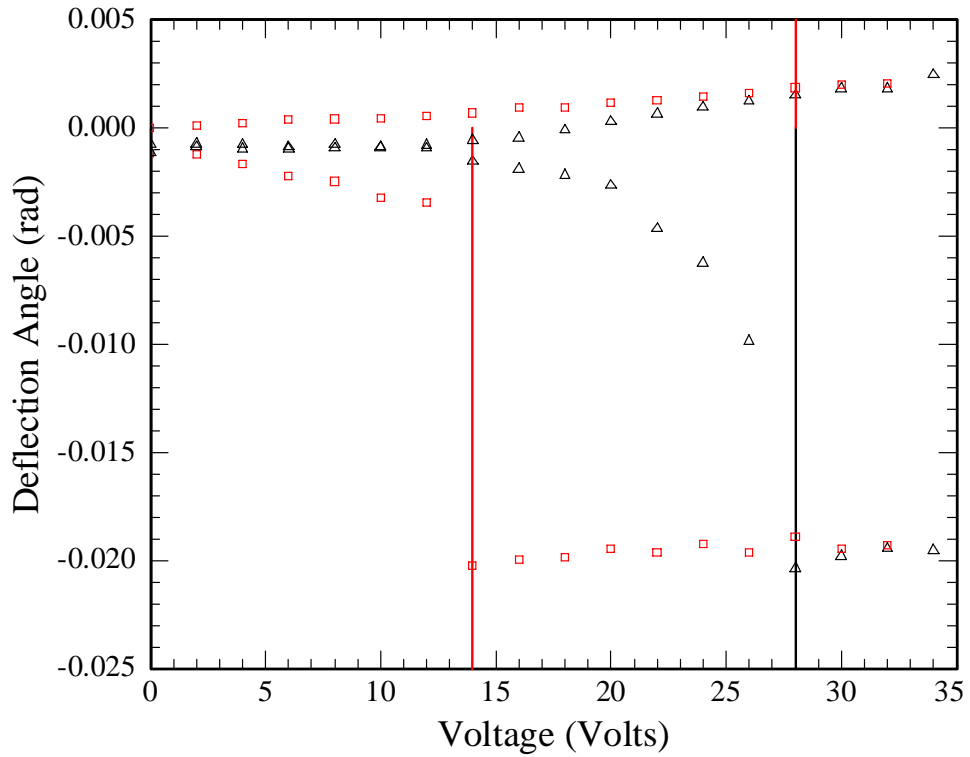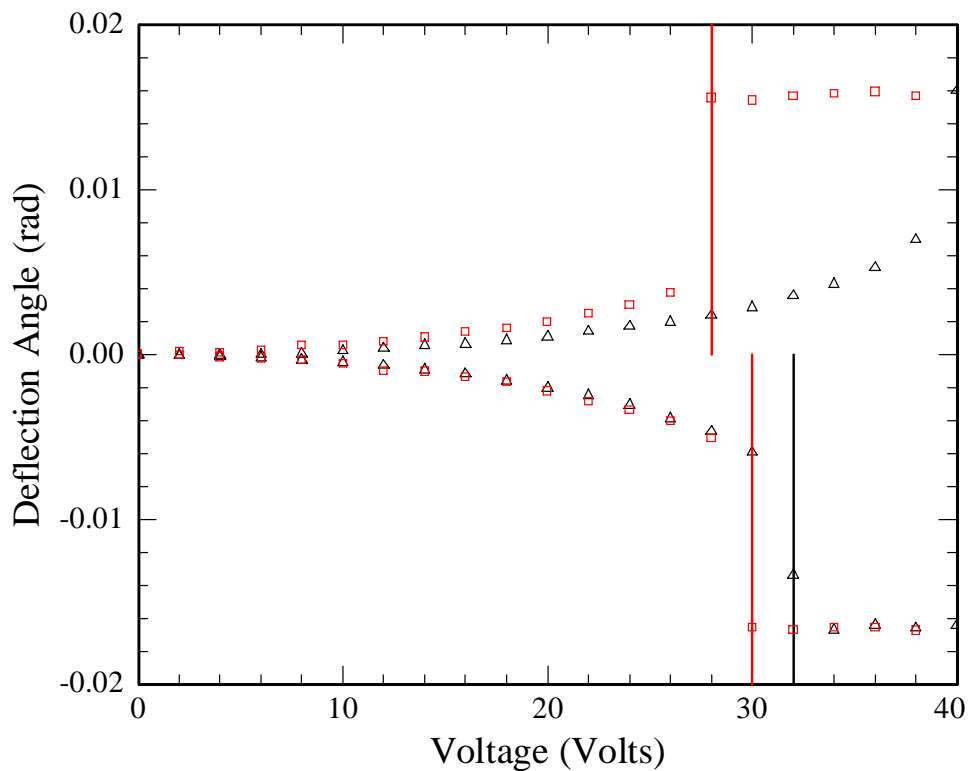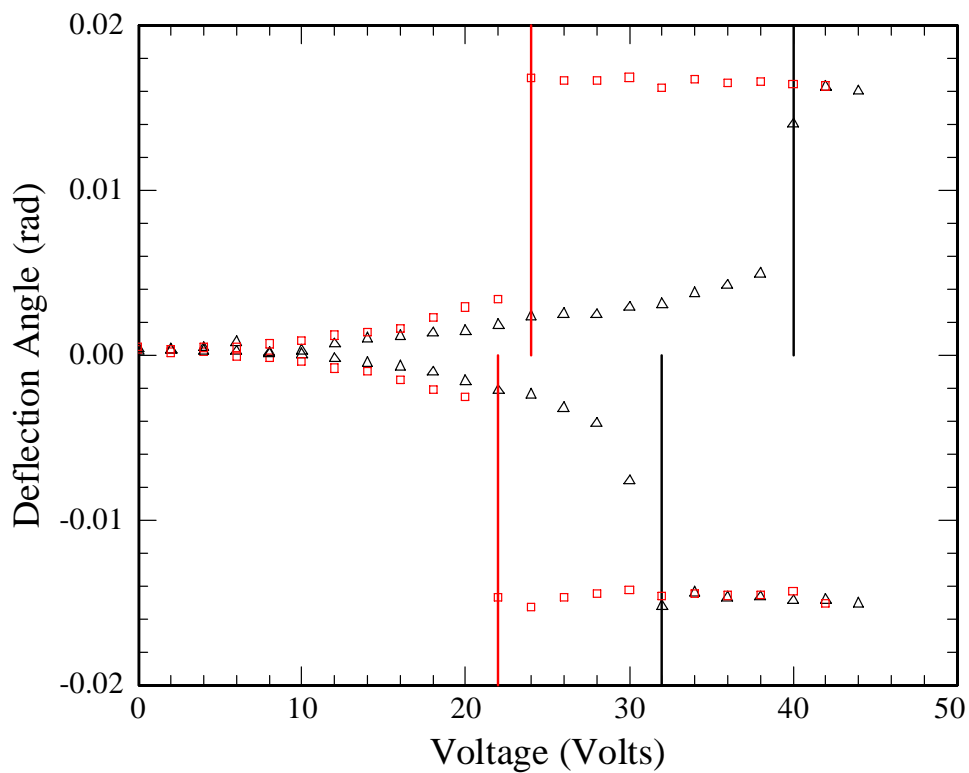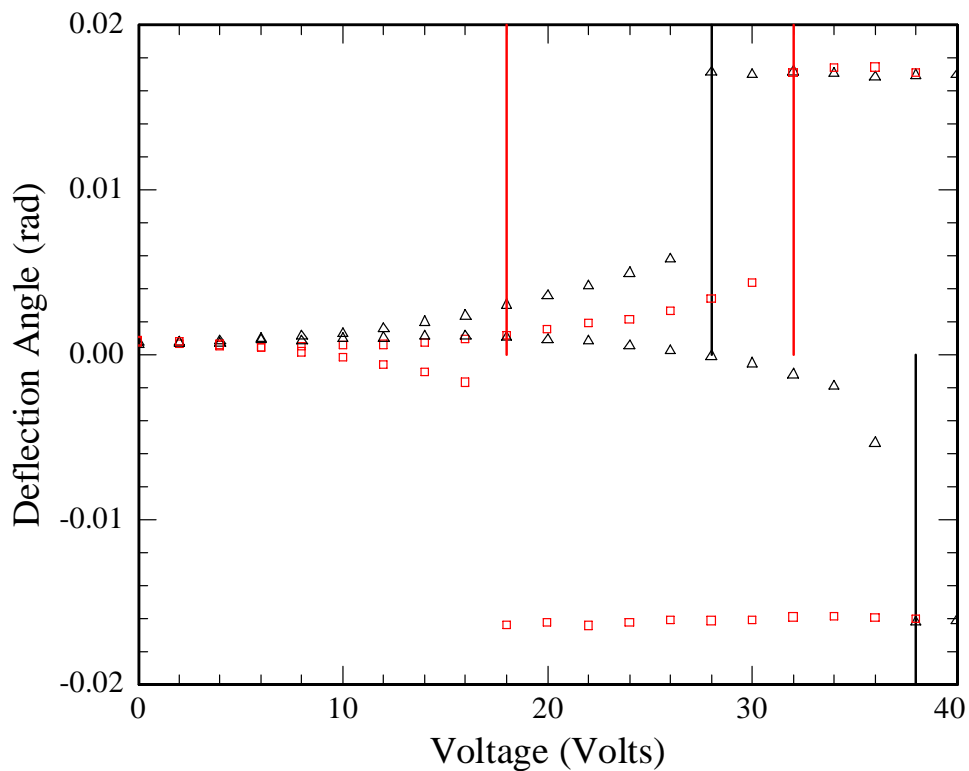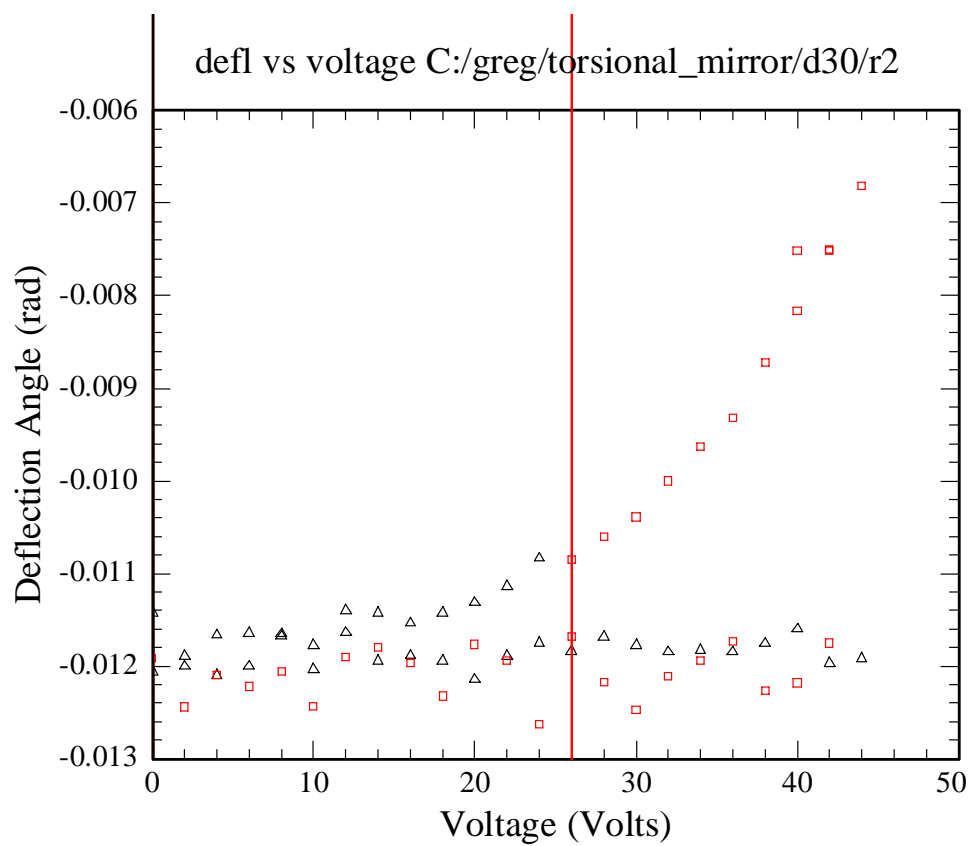
defl vs voltage C:/greg/torsional_mirror/d30/r2

92

defl vs voltage C:/greg/torsional_mirror/d31/r2
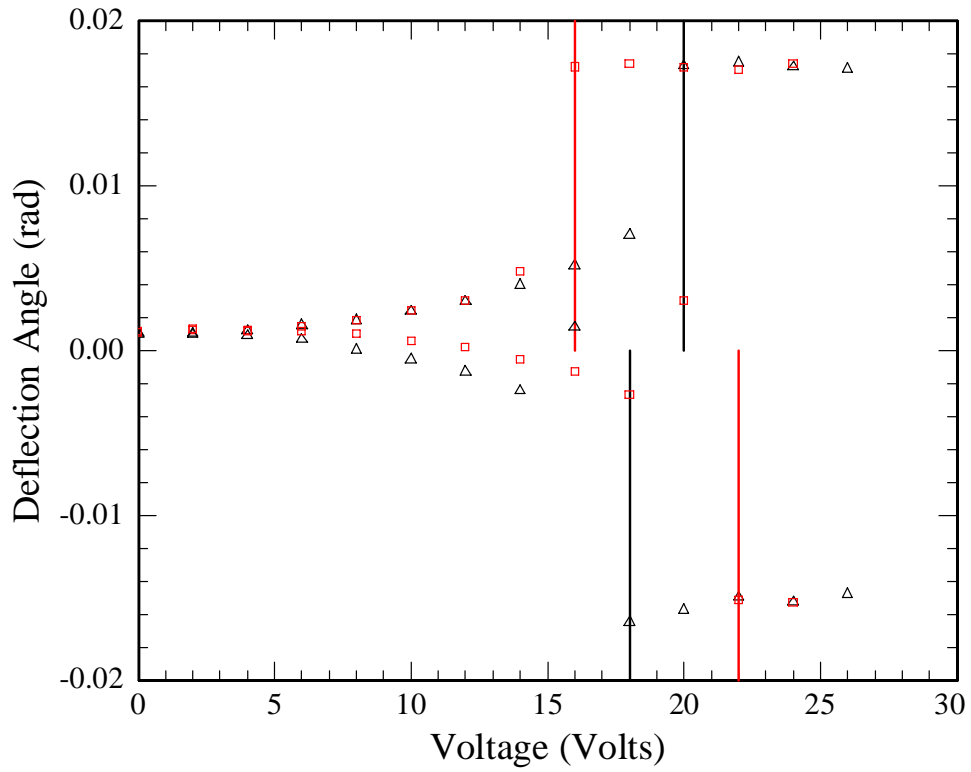
defl vs voltage C:/greg/torsional_mirror/d32/r4
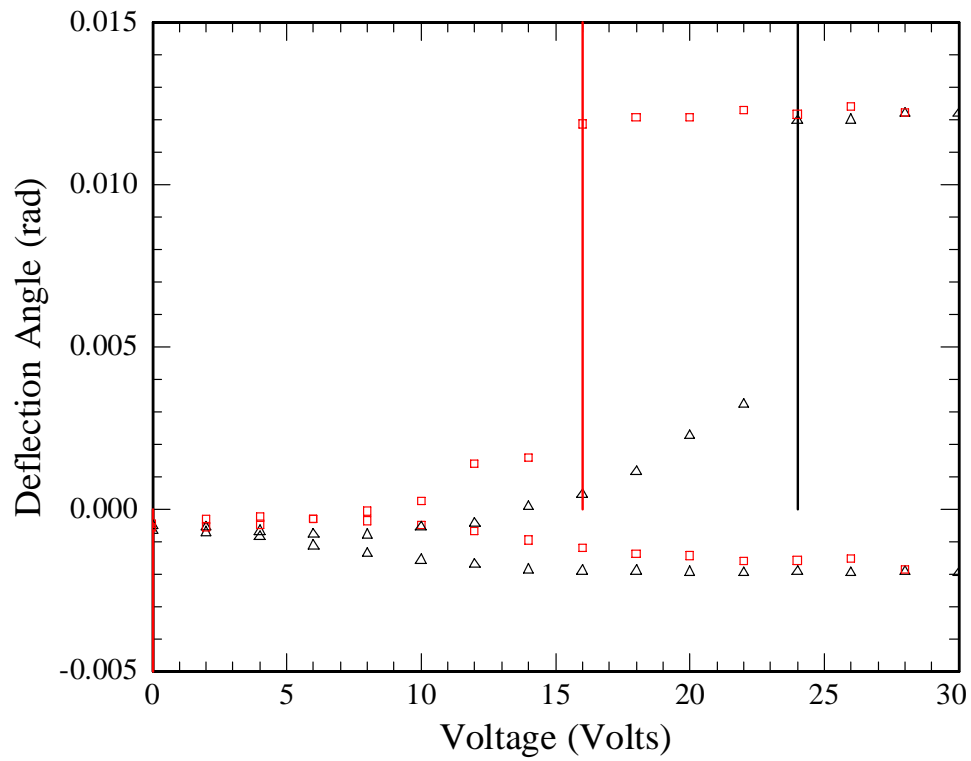
Appendix D

Table D.1 Dimensions of MEMS switch structures described in Section 5.1. Dimensions are given in microns.
Electrode designation indicates whether the fixed electrodes were straight (str) or curved (crv).

Designation	Length	Width	Gap	Electrode
1-1	35	0.75	0.5	str
1-2	30	1.25	0.4	str
1-3	30	1	0.4	str
1-4	30	0.75	0.4	str
1-5	20	0.75	0.4	str
1-6	20	2	0.4	str
1-7	20	2	0.5	str
1-8	17.5	0.75	0.4	str
2-1	50	1	0.5	str
2-2	50	1	0.75	crv
2-3	50	1	0.75	str
2-4	50	1.5	0.5	str
2-5	40	1	0.5	str
2-6	40	1.25	0.5	str
2-7	40	0.75	0.5	str
2-8	35	1	0.5	str
3-1	70	1	1	str
3-2	70	1	1	crv
3-3	60	1	1	crv
3-4	60	1	0.75	crv
3-5	60	1	0.75	str
3-6	60	1.5	0.5	str
3-7	60	1.5	0.75	crv
3-8	60	2	0.5	str
4-1	80	1.5	0.75	crv
4-2	80	1.5	0.75	str
4-3	70	2	0.5	str
4-4	70	1.5	0.75	str
4-5	70	1.5	0.75	crv
4-6	70	1.5	0.5	str
4-7	70	1	0.75	str
4-8	70	1	0.75	crv

Table D.2 Dimensions of MEMS switch structures described in Section 5.1. Dimensions are given in microns. Electrode designation indicates whether the fixed electrodes were straight (str) or curved (crv).

Designation	Length	Width	Gap	Electrode
5-1	90	1.5	1	crv
5-2	90	1.5	1	str
5-3	90	2	1	crv
5-4	90	2	0.5	str
5-5	90	2	0.75	crv
5-6	90	2	0.75	str
5-7	80	1	1	crv
5-8	80	1	1	str
6-1	100	2	0.75	str
6-2	100	2	0.75	crv
6-3	100	1.5	0.75	str
6-4	100	1.5	0.75	crv
6-5	100	1.5	1	str
6-6	100	1.5	1	crv
6-7	100	1	1	str
6-8	100	1	1	crv
7-1	120	2	0.75	str
7-2	120	2	0.75	crv
7-3	110	2	1	str
7-4	110	2	1	crv
7-5	120	1.5	1	str
7-6	120	1.5	1	crv
7-7	120	2	1	str
7-8	120	2	1	crv
8-1	140	1.25	1	str
8-2	140	1.25	1	crv
8-3	140	1.5	1	str
8-4	140	1.5	1	crv
8-5	140	1.75	1	str
8-6	140	1.75	1	crv
8-7	140	2	1	str
8-8	140	2	1	crv

Appendix E

Table E.1 Design parameters for the different integrated optical MEMS switch designs described in Section 5.6 for modules (die) A, B, and C.

Mod	Device #		Optical Parameters							
			Coupling length	Coupling gap (closed)	Coupling gap (open)	Coupling gap (rest)	Length	Width	Overlap	Gap
A	1		1.00E-04	1.00E-07	8.00E-07	4.50E-07	1.00E-04	5.00E-07	0.00E+00	4.50E-07
A	2		1.00E-04	1.25E-07	8.00E-07	4.63E-07	1.00E-04	5.25E-07	2.50E-08	4.38E-07
A	3		1.00E-04	1.50E-07	8.00E-07	4.75E-07	1.00E-04	5.50E-07	5.00E-08	4.25E-07
A	4		1.00E-04	1.75E-07	8.00E-07	4.88E-07	1.00E-04	5.75E-07	7.50E-08	4.13E-07
A	5		1.00E-04	2.00E-07	8.00E-07	5.00E-07	1.00E-04	6.00E-07	1.00E-07	4.00E-07
A	6		1.00E-04	2.25E-07	8.00E-07	5.13E-07	1.00E-04	6.25E-07	1.25E-07	3.88E-07
A	7		1.00E-04	2.50E-07	8.00E-07	5.25E-07	1.00E-04	6.50E-07	1.50E-07	3.75E-07
A	8		1.00E-04	2.75E-07	8.00E-07	5.38E-07	1.00E-04	6.75E-07	1.75E-07	3.63E-07
B	1		8.00E-05	1.00E-07	8.00E-07	4.50E-07	8.00E-05	5.00E-07	0.00E+00	4.50E-07
B	2		8.00E-05	1.25E-07	8.00E-07	4.63E-07	8.00E-05	5.25E-07	2.50E-08	4.38E-07
B	3		8.00E-05	1.50E-07	8.00E-07	4.75E-07	8.00E-05	5.50E-07	5.00E-08	4.25E-07
B	4		8.00E-05	1.75E-07	8.00E-07	4.88E-07	8.00E-05	5.75E-07	7.50E-08	4.13E-07
B	5		8.00E-05	2.00E-07	8.00E-07	5.00E-07	8.00E-05	6.00E-07	1.00E-07	4.00E-07
B	6		8.00E-05	2.25E-07	8.00E-07	5.13E-07	8.00E-05	6.25E-07	1.25E-07	3.88E-07
B	7		8.00E-05	2.50E-07	8.00E-07	5.25E-07	8.00E-05	6.50E-07	1.50E-07	3.75E-07
B	8		8.00E-05	2.75E-07	8.00E-07	5.38E-07	8.00E-05	6.75E-07	1.75E-07	3.63E-07
C	1		6.00E-05	1.00E-07	8.00E-07	4.50E-07	6.00E-05	5.00E-07	0.00E+00	4.50E-07
C	2		6.00E-05	1.25E-07	8.00E-07	4.63E-07	6.00E-05	5.25E-07	2.50E-08	4.38E-07
C	3		6.00E-05	1.50E-07	8.00E-07	4.75E-07	6.00E-05	5.50E-07	5.00E-08	4.25E-07
C	4		6.00E-05	1.75E-07	8.00E-07	4.88E-07	6.00E-05	5.75E-07	7.50E-08	4.13E-07
C	5		6.00E-05	2.00E-07	8.00E-07	5.00E-07	6.00E-05	6.00E-07	1.00E-07	4.00E-07
C	6		6.00E-05	2.25E-07	8.00E-07	5.13E-07	6.00E-05	6.25E-07	1.25E-07	3.88E-07
C	7		6.00E-05	2.50E-07	8.00E-07	5.25E-07	6.00E-05	6.50E-07	1.50E-07	3.75E-07
C	8		6.00E-05	2.75E-07	8.00E-07	5.38E-07	6.00E-05	6.75E-07	1.75E-07	3.63E-07

Table E.2 Design parameters for the different integrated optical MEMS switch designs described in Section 5.6 for modules (die) D, E, and F.

Mod	Device #		length	Optical Parameters							
			length	gap (closed)	gap (open)	gap (rest)	Length	Width	Overlap	Gap
D	1		5.00E-05	1.00E-07	8.00E-07	4.50E-07	5.00E-05	5.00E-07	0.00E+00	4.50E-07
D	2		5.00E-05	1.25E-07	8.00E-07	4.63E-07	5.00E-05	5.25E-07	2.50E-08	4.38E-07
D	3		5.00E-05	1.50E-07	8.00E-07	4.75E-07	5.00E-05	5.50E-07	5.00E-08	4.25E-07
D	4		5.00E-05	1.75E-07	8.00E-07	4.88E-07	5.00E-05	5.75E-07	7.50E-08	4.13E-07
D	5		5.00E-05	2.00E-07	8.00E-07	5.00E-07	5.00E-05	6.00E-07	1.00E-07	4.00E-07
D	6		5.00E-05	2.25E-07	8.00E-07	5.13E-07	5.00E-05	6.25E-07	1.25E-07	3.88E-07
D	7		5.00E-05	2.50E-07	8.00E-07	5.25E-07	5.00E-05	6.50E-07	1.50E-07	3.75E-07
D	8		5.00E-05	2.75E-07	8.00E-07	5.38E-07	5.00E-05	6.75E-07	1.75E-07	3.63E-07
E	1		4.00E-05	1.00E-07	8.00E-07	4.50E-07	4.00E-05	5.00E-07	0.00E+00	4.50E-07
E	2		4.00E-05	1.25E-07	8.00E-07	4.63E-07	4.00E-05	5.25E-07	2.50E-08	4.38E-07
E	3		4.00E-05	1.50E-07	8.00E-07	4.75E-07	4.00E-05	5.50E-07	5.00E-08	4.25E-07
E	4		4.00E-05	1.75E-07	8.00E-07	4.88E-07	4.00E-05	5.75E-07	7.50E-08	4.13E-07
E	5		4.00E-05	2.00E-07	8.00E-07	5.00E-07	4.00E-05	6.00E-07	1.00E-07	4.00E-07
E	6		4.00E-05	2.25E-07	8.00E-07	5.13E-07	4.00E-05	6.25E-07	1.25E-07	3.88E-07
E	7		4.00E-05	2.50E-07	8.00E-07	5.25E-07	4.00E-05	6.50E-07	1.50E-07	3.75E-07
E	8		4.00E-05	2.75E-07	8.00E-07	5.38E-07	4.00E-05	6.75E-07	1.75E-07	3.63E-07
F	1		3.00E-05	1.00E-07	8.00E-07	4.50E-07	3.00E-05	5.00E-07	0.00E+00	4.50E-07
F	2		3.00E-05	1.25E-07	8.00E-07	4.63E-07	3.00E-05	5.25E-07	2.50E-08	4.38E-07
F	3		3.00E-05	1.50E-07	8.00E-07	4.75E-07	3.00E-05	5.50E-07	5.00E-08	4.25E-07
F	4		3.00E-05	1.75E-07	8.00E-07	4.88E-07	3.00E-05	5.75E-07	7.50E-08	4.13E-07
F	5		3.00E-05	2.00E-07	8.00E-07	5.00E-07	3.00E-05	6.00E-07	1.00E-07	4.00E-07
F	6		3.00E-05	2.25E-07	8.00E-07	5.13E-07	3.00E-05	6.25E-07	1.25E-07	3.88E-07
F	7		3.00E-05	2.50E-07	8.00E-07	5.25E-07	3.00E-05	6.50E-07	1.50E-07	3.75E-07
F	8		3.00E-05	2.75E-07	8.00E-07	5.38E-07	3.00E-05	6.75E-07	1.75E-07	3.63E-07

Table E.3 Design parameters for the different integrated optical MEMS switch designs described in Section 5.6 for modules (die) G, H, and I.
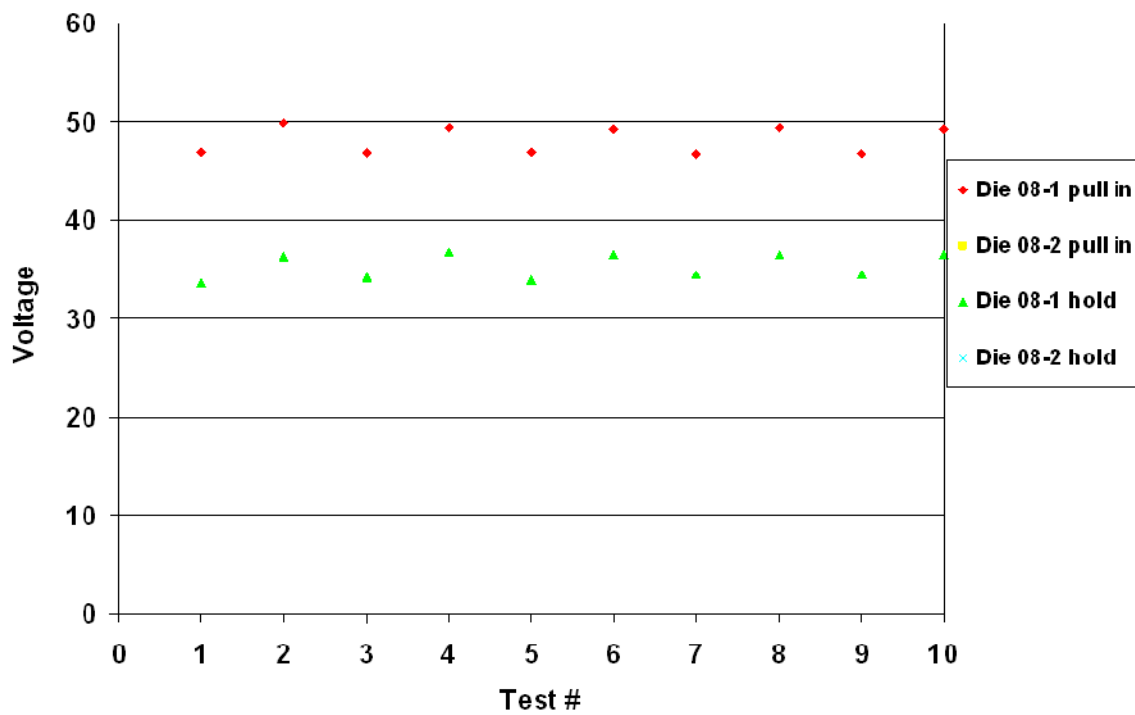
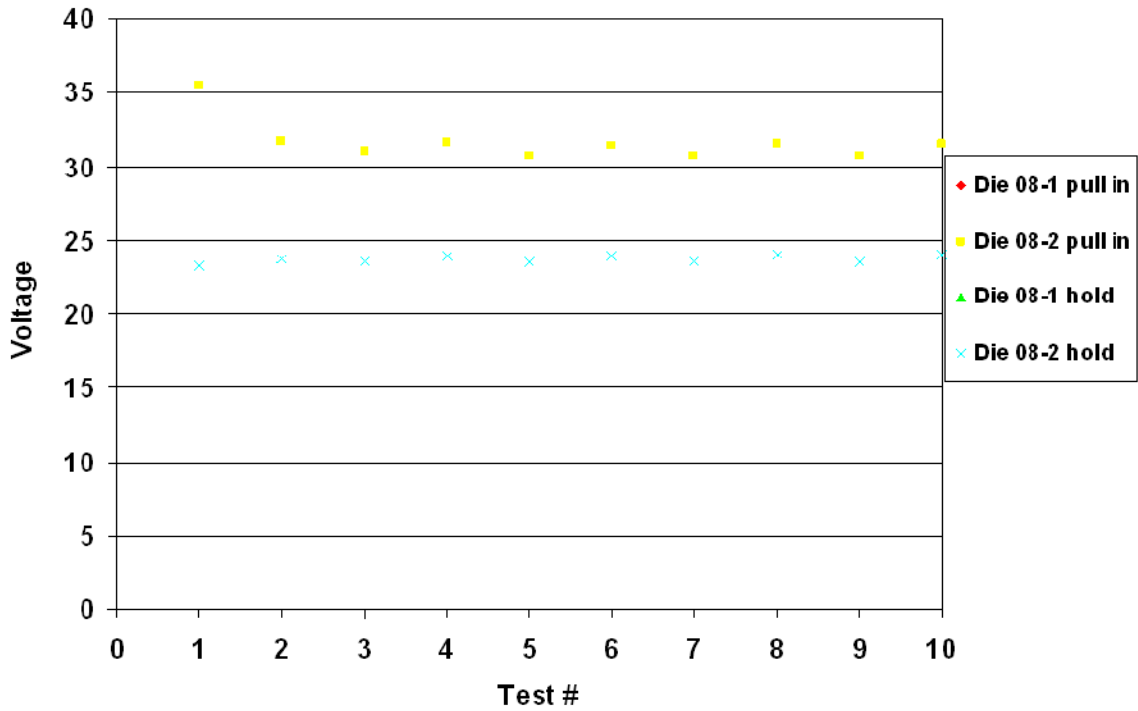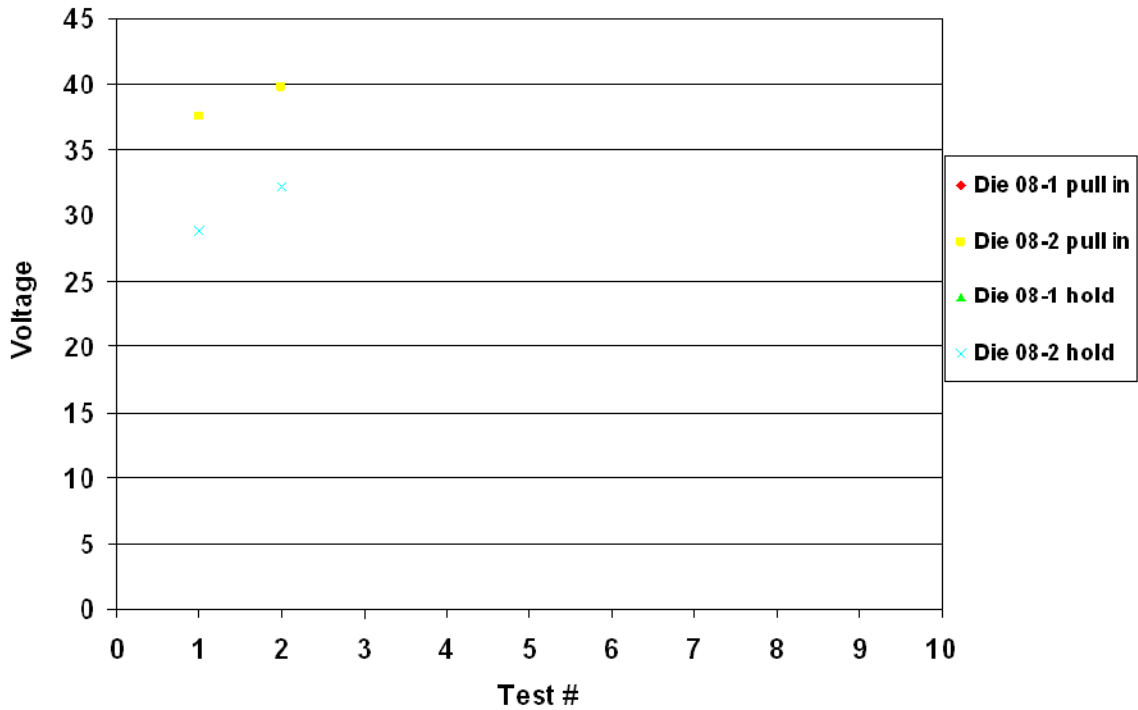| | | non-movin | ring | Optical Parameters Coupling | Coupling | Coupling | | | | |
Mod	Devic	gap	diameter	gap (closed)	gap (open)	gap (rest)	Length	Width	Overlap	Gap
G	1	1.75E-07	1.00E-05	1.00E-07	8.00E-07	4.50E-07	1.00E-04	5.00E-07	0.00E+00	4.50E-07
G	2	1.75E-07	1.00E-05	1.25E-07	8.00E-07	4.63E-07	8.00E-05	5.25E-07	2.50E-08	4.38E-07
G	3	2.00E-07	1.00E-05	1.50E-07	8.00E-07	4.75E-07	6.00E-05	5.50E-07	5.00E-08	4.25E-07
G	4	2.00E-07	1.00E-05	1.75E-07	8.00E-07	4.88E-07	1.00E-04	5.75E-07	7.50E-08	4.13E-07
G	5	2.00E-07	1.00E-05	2.00E-07	8.00E-07	5.00E-07	8.00E-05	6.00E-07	1.00E-07	4.00E-07
G	6	2.25E-07	1.00E-05	2.25E-07	8.00E-07	5.13E-07	6.00E-05	6.25E-07	1.25E-07	3.88E-07
G	7	2.50E-07	1.00E-05	2.50E-07	8.00E-07	5.25E-07	1.00E-04	6.50E-07	1.50E-07	3.75E-07
G	8	2.75E-07	1.00E-05	2.75E-07	8.00E-07	5.38E-07	6.00E-05	6.75E-07	1.75E-07	3.63E-07
H	1	1.75E-07	1.00E-05	1.00E-07	8.00E-07	4.50E-07	4.50E-05	5.00E-07	0.00E+00	4.50E-07
H	2	1.75E-07	1.00E-05	1.25E-07	8.00E-07	4.63E-07	4.50E-05	5.25E-07	2.50E-08	4.38E-07
H	3	2.00E-07	1.00E-05	1.50E-07	8.00E-07	4.75E-07	4.50E-05	5.50E-07	5.00E-08	4.25E-07
H	4	2.00E-07	1.00E-05	1.75E-07	8.00E-07	4.88E-07	4.50E-05	5.75E-07	7.50E-08	4.13E-07
H	5	2.00E-07	1.00E-05	2.00E-07	8.00E-07	5.00E-07	4.50E-05	6.00E-07	1.00E-07	4.00E-07
H	6	2.25E-07	1.00E-05	2.25E-07	8.00E-07	5.13E-07	4.50E-05	6.25E-07	1.25E-07	3.88E-07
H	7	2.50E-07	1.00E-05	2.50E-07	8.00E-07	5.25E-07	4.50E-05	6.50E-07	1.50E-07	3.75E-07
H	8	2.75E-07	1.00E-05	2.75E-07	8.00E-07	5.38E-07	4.50E-05	6.75E-07	1.75E-07	3.63E-07
I	1	1.75E-07	1.00E-05	1.00E-07	8.00E-07	4.50E-07	3.50E-05	5.00E-07	0.00E+00	4.50E-07
I	2	1.75E-07	1.00E-05	1.25E-07	8.00E-07	4.63E-07	3.50E-05	5.25E-07	2.50E-08	4.38E-07
I	3	2.00E-07	1.00E-05	1.50E-07	8.00E-07	4.75E-07	3.50E-05	5.50E-07	5.00E-08	4.25E-07
I	4	2.00E-07	1.00E-05	1.75E-07	8.00E-07	4.88E-07	3.50E-05	5.75E-07	7.50E-08	4.13E-07
I	5	2.00E-07	1.00E-05	2.00E-07	8.00E-07	5.00E-07	3.50E-05	6.00E-07	1.00E-07	4.00E-07
I	6	2.25E-07	1.00E-05	2.25E-07	8.00E-07	5.13E-07	3.50E-05	6.25E-07	1.25E-07	3.88E-07
I	7	2.50E-07	1.00E-05	2.50E-07	8.00E-07	5.25E-07	3.50E-05	6.50E-07	1.50E-07	3.75E-07
I	8	2.75E-07	1.00E-05	2.75E-07	8.00E-07	5.38E-07	3.50E-05	6.75E-07	1.75E-07	3.63E-07

Appendix F

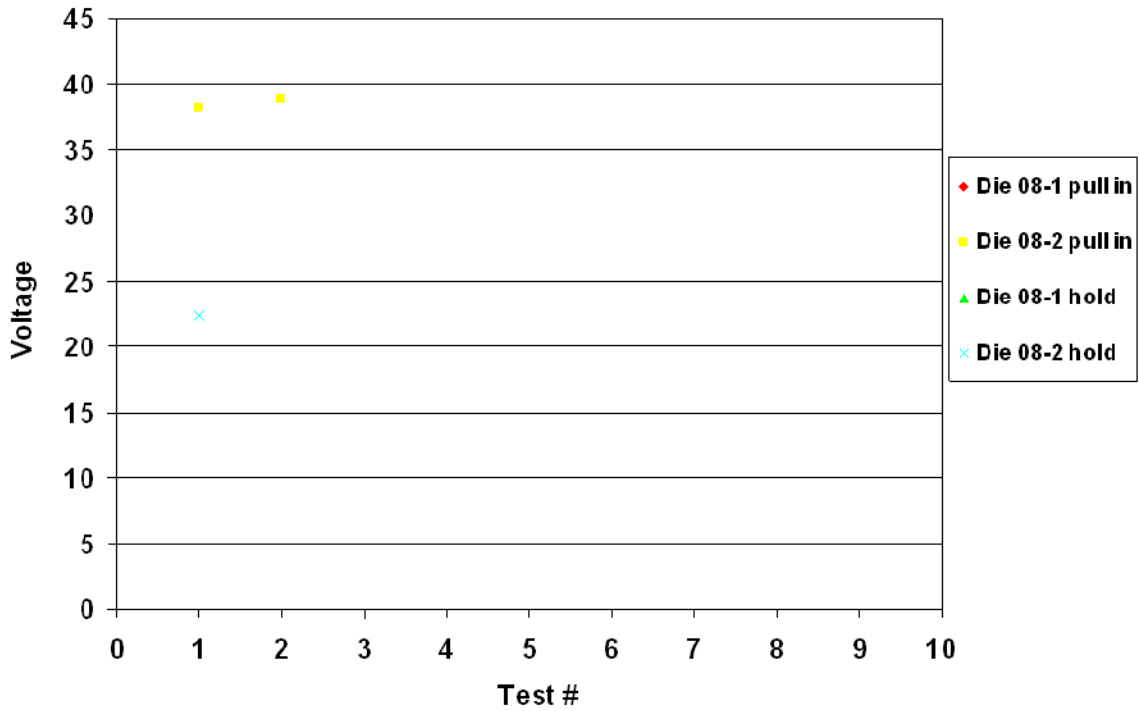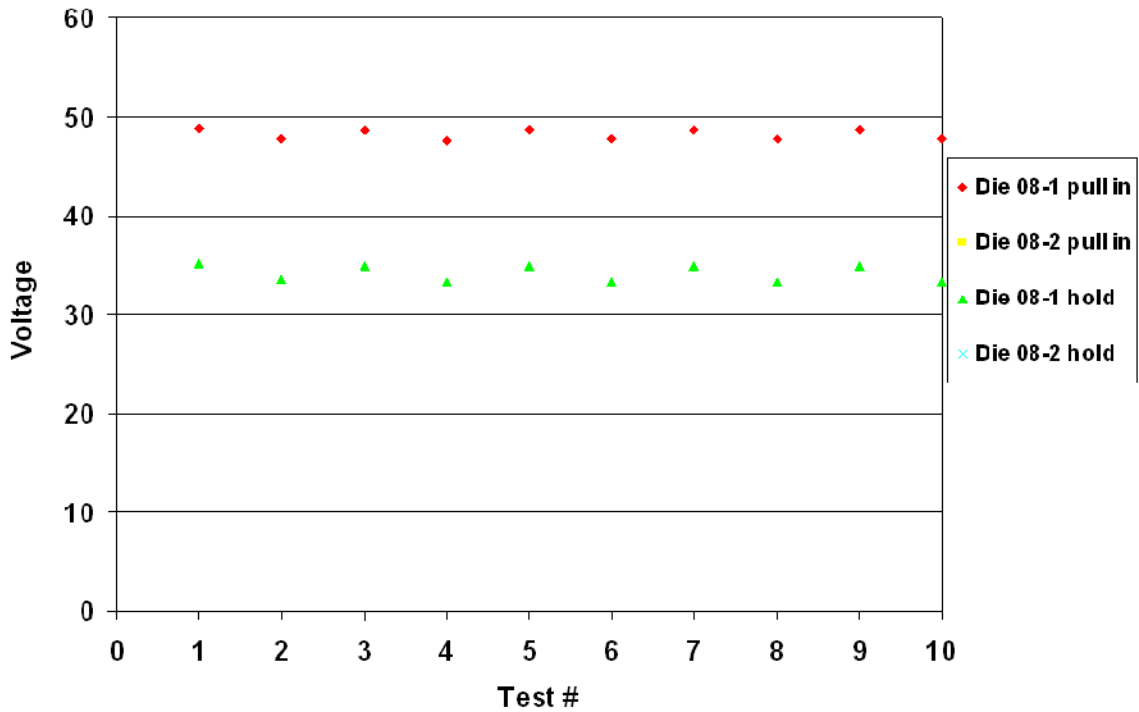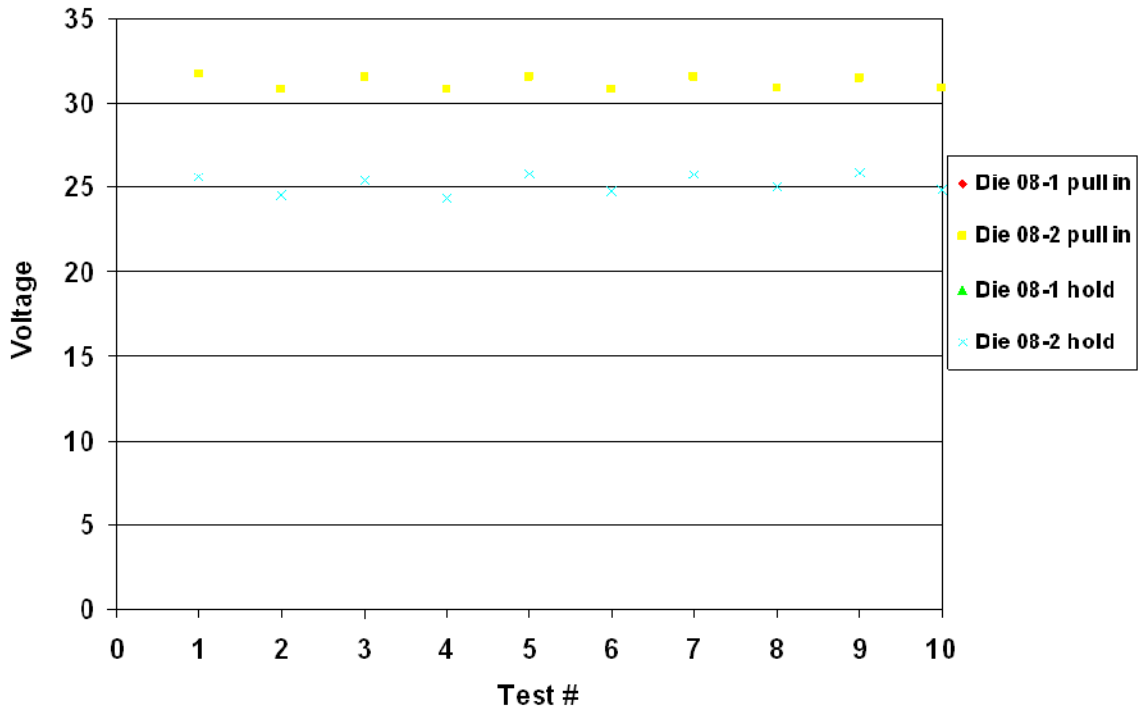## Die 08 Device 1 Left HfO$_2$ in Vacuum
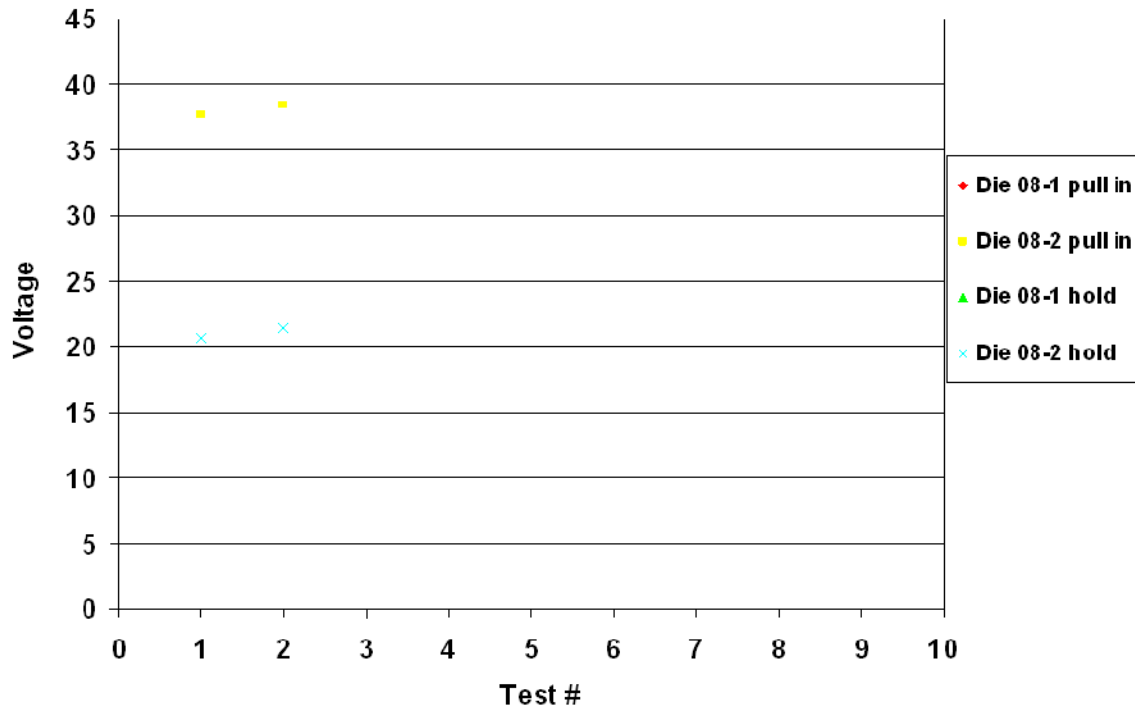
Die 08 Device 3 Left HfO$_2$ in Vacuum

Die 08 Device 4 Left HfO$_2$ in Vacuum

Legend:
- Die 08-1 pull in
- Die 08-2 pull in
- Die 08-1 hold
- Die 08-2 hold

Die 08 Device 6 Left HfO$_2$ in Vacuum

Legend:
- Die 08-1 pull in
- Die 08-2 pull in
- Die 08-1 hold
- Die 08-2 hold

Die 08 Device 1 Right HfO$_2$ in Vacuum

Legend:
- Die 08-1 pull in
- Die 08-2 pull in
- Die 08-1 hold
- Die 08-2 hold

Die 08 Device 3 Right HfO$_2$ in Vacuum

Legend:
- Die 08-1 pull in
- Die 08-2 pull in
- Die 08-1 hold
- Die 08-2 hold

Die 08 Device 4 Right HfO$_2$ in Vacuum

Die 07 Device 6 Left HfO$_2$ in Vacuum
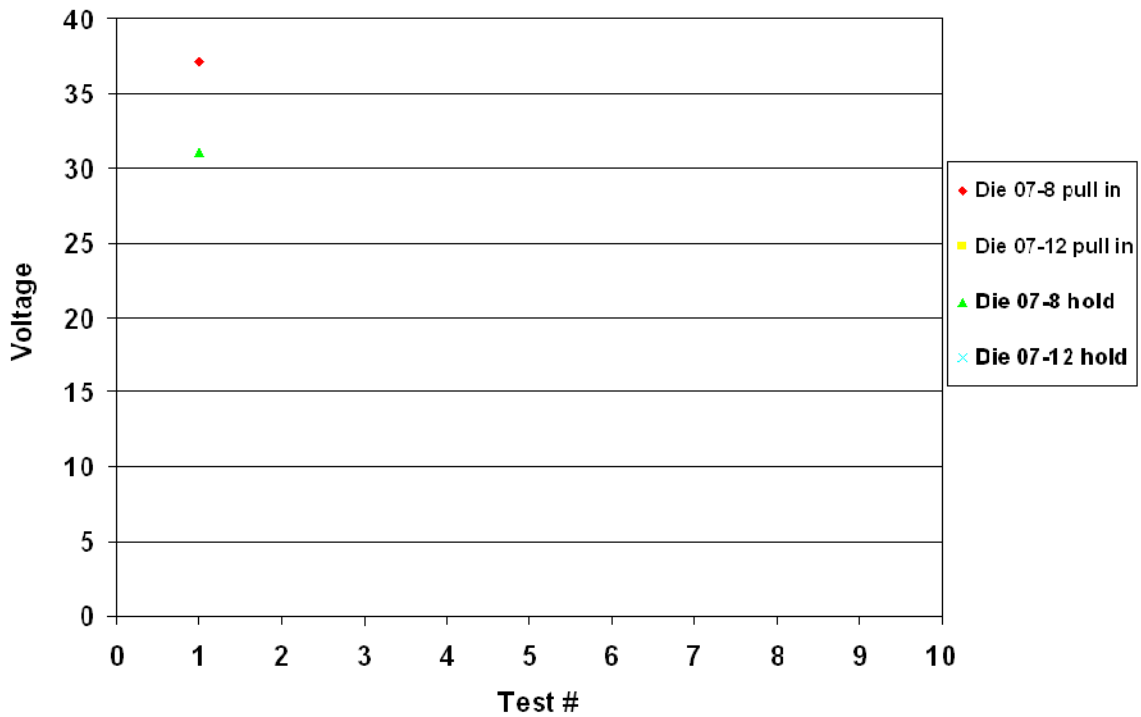
Die 07 Device 6 Right HfO$_2$ in Vacuum

Legend:
- Die 07-8 pull in
- Die 07-12 pull in
- Die 07-8 hold
- Die 07-12 hold

Voltage vs Test #

Die 08 Device 1 Left Al$_2$O$_3$ in Vacuum

Legend:
- Die 08-5 pull in
- Die 08-17 pull in
- Die 08-5 hold
- Die 08-17 hold

Voltage vs Test #
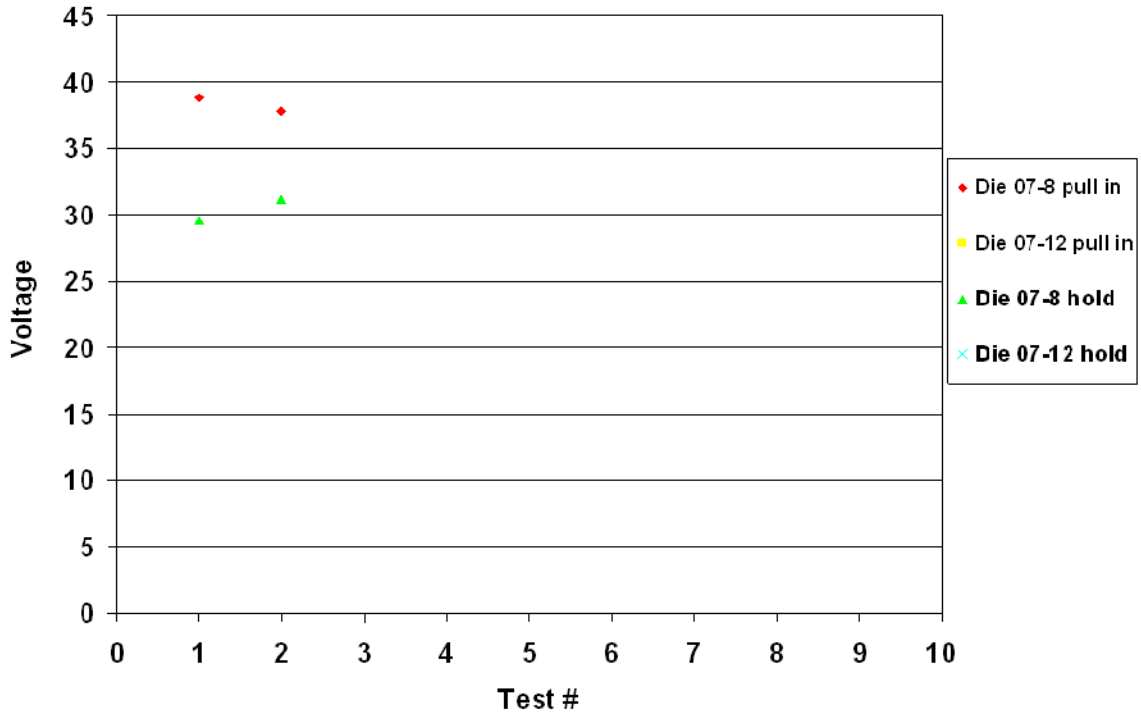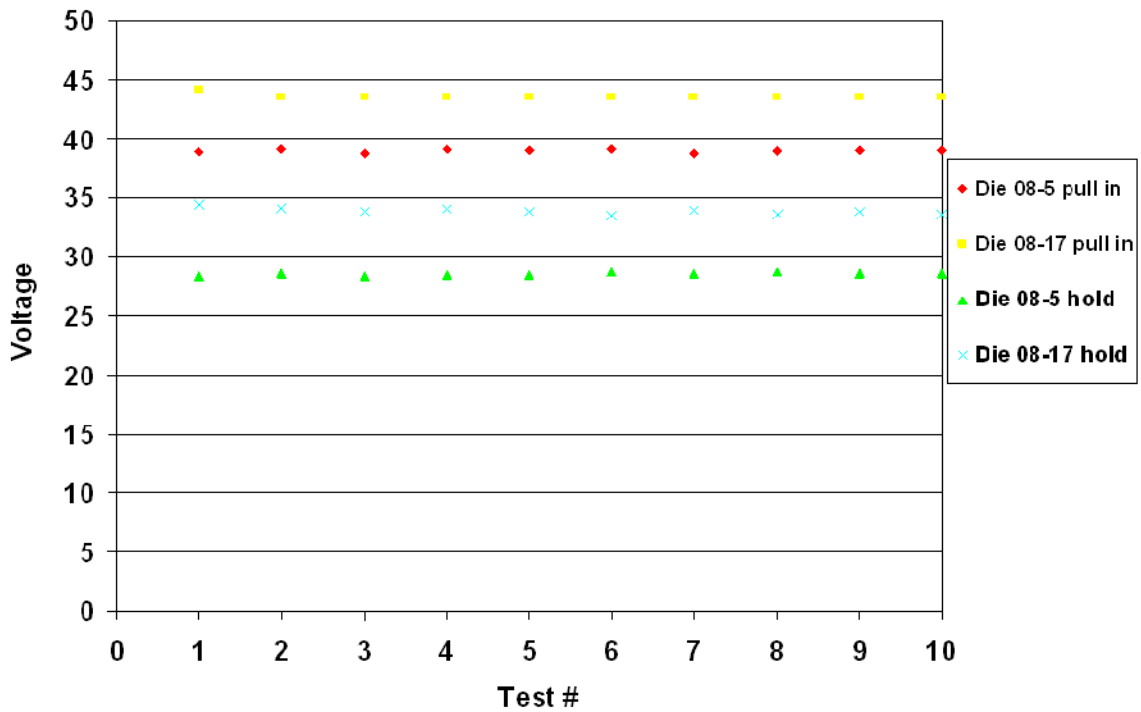
Die 08 Device 3 Left Al$_2$O$_3$ in Vacuum
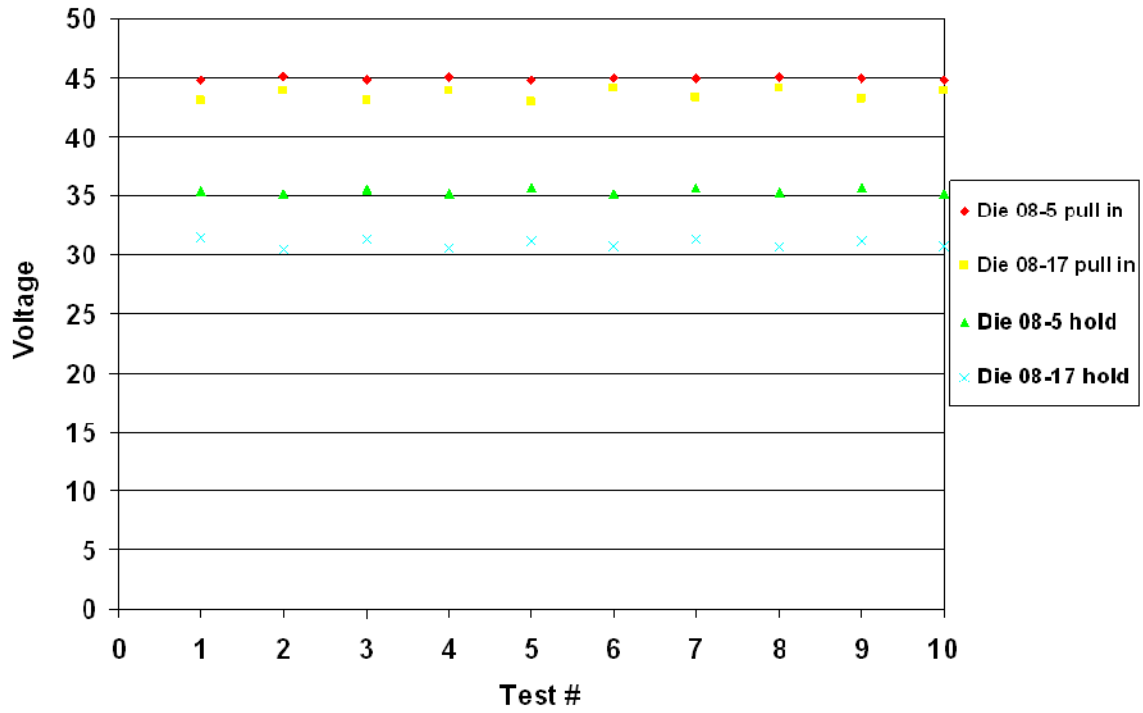
Die 08 Device 5 Left Al$_2$O$_3$ in Vacuum
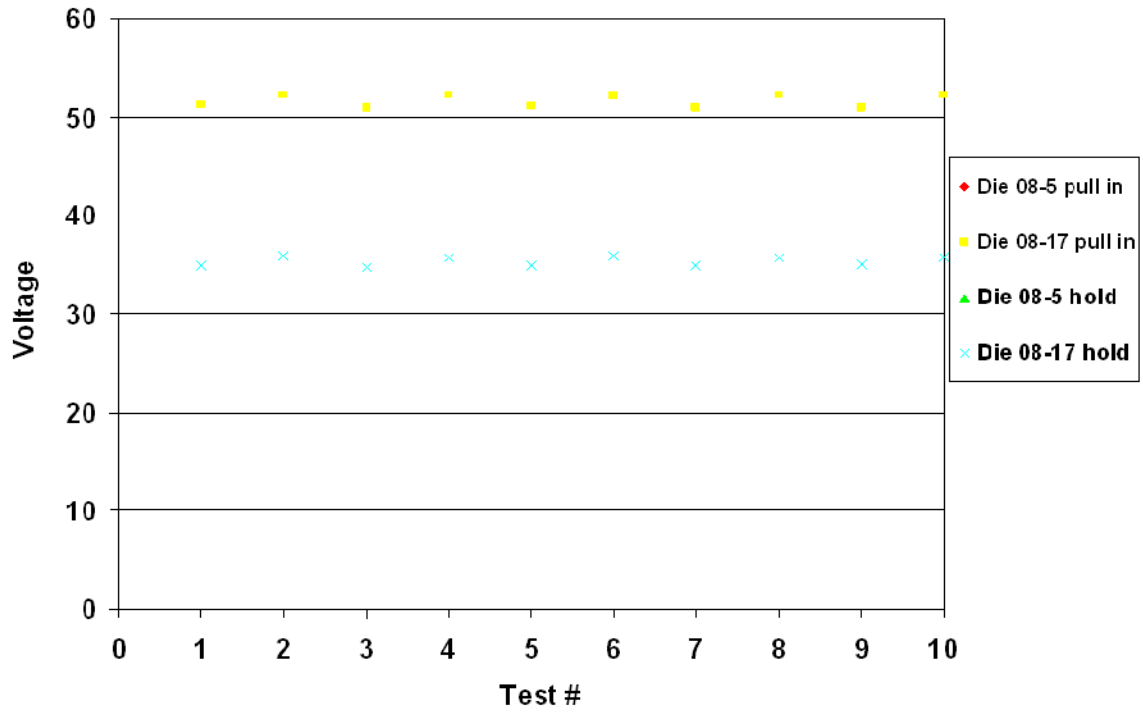
Die 08 Device 6 Left Al$_2$O$_3$ in Vacuum
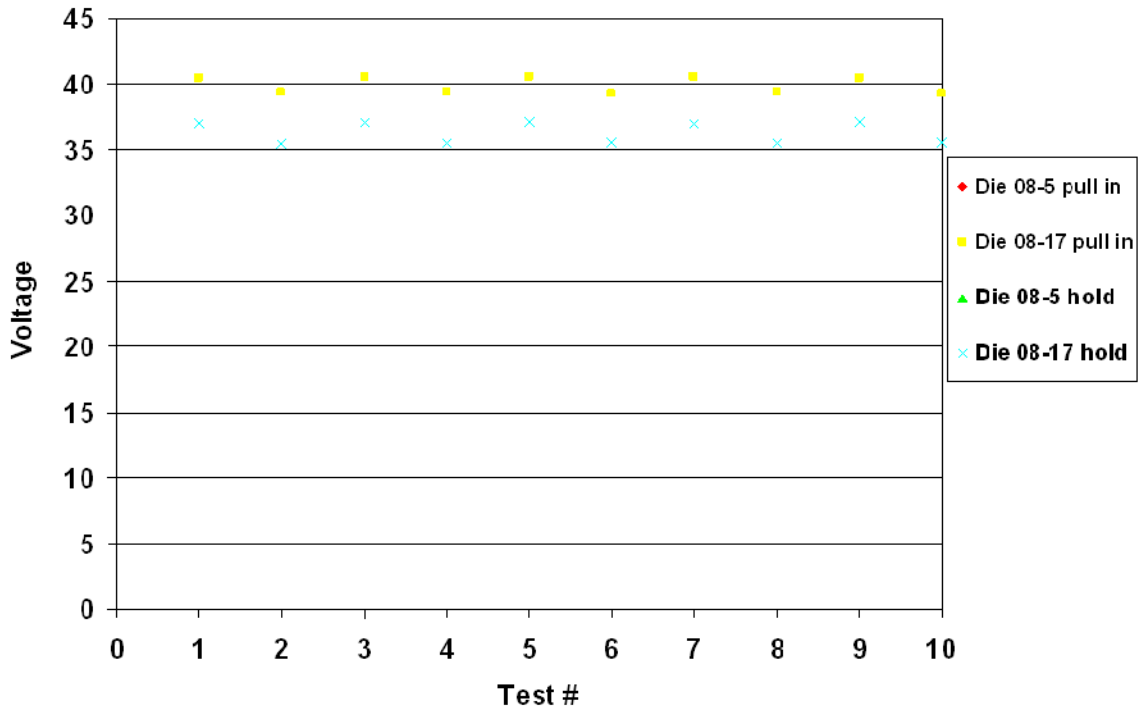
Legend:
- ◆ Die 08-5 pull in
- ■ Die 08-17 pull in
- ▲ **Die 08-5 hold**
- ✕ **Die 08-17 hold**

Die 08 Device 7 Left Al$_2$O$_3$ in Vacuum

Legend:
- ◆ Die 08-5 pull in
- ■ Die 08-17 pull in
- ▲ **Die 08-5 hold**
- ✕ **Die 08-17 hold**

Die 08 Device 1 Right Al$_2$O$_3$ in Vacuum

Legend:
- Die 08-5 pull in
- Die 08-17 pull in
- Die 08-5 hold
- Die 08-17 hold

Voltage (y-axis), Test # (x-axis)
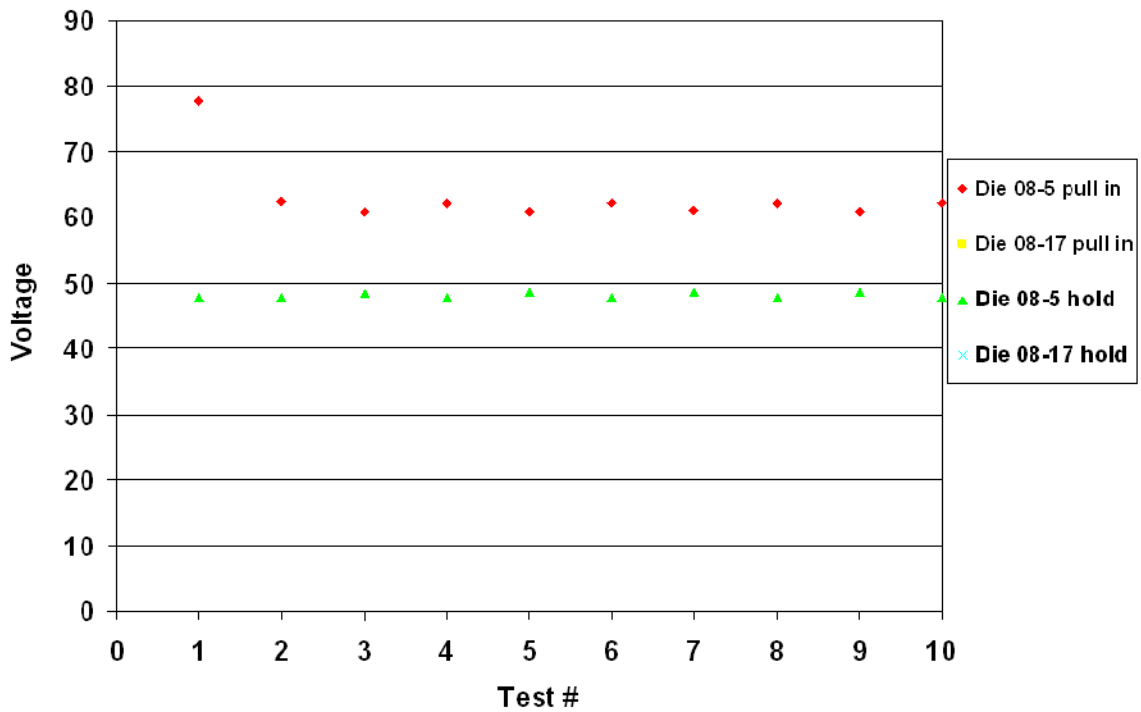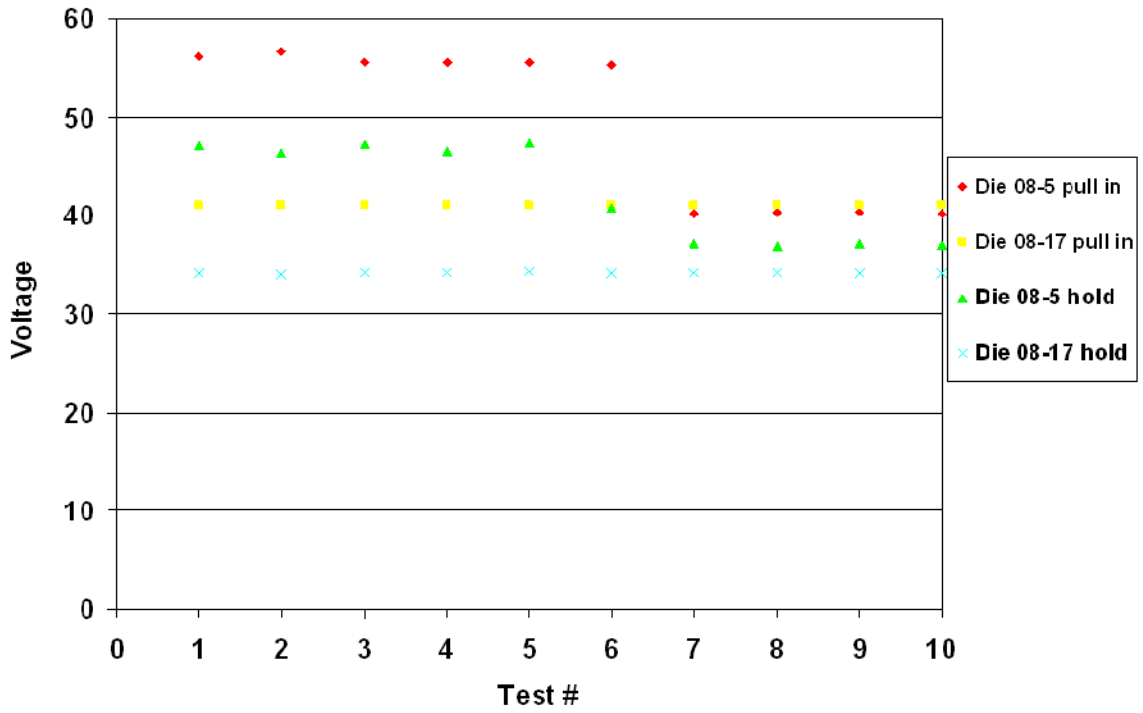
Die 08 Device 3 Right Al$_2$O$_3$ in Vacuum

Legend:
- Die 08-5 pull in
- Die 08-17 pull in
- Die 08-5 hold
- Die 08-17 hold
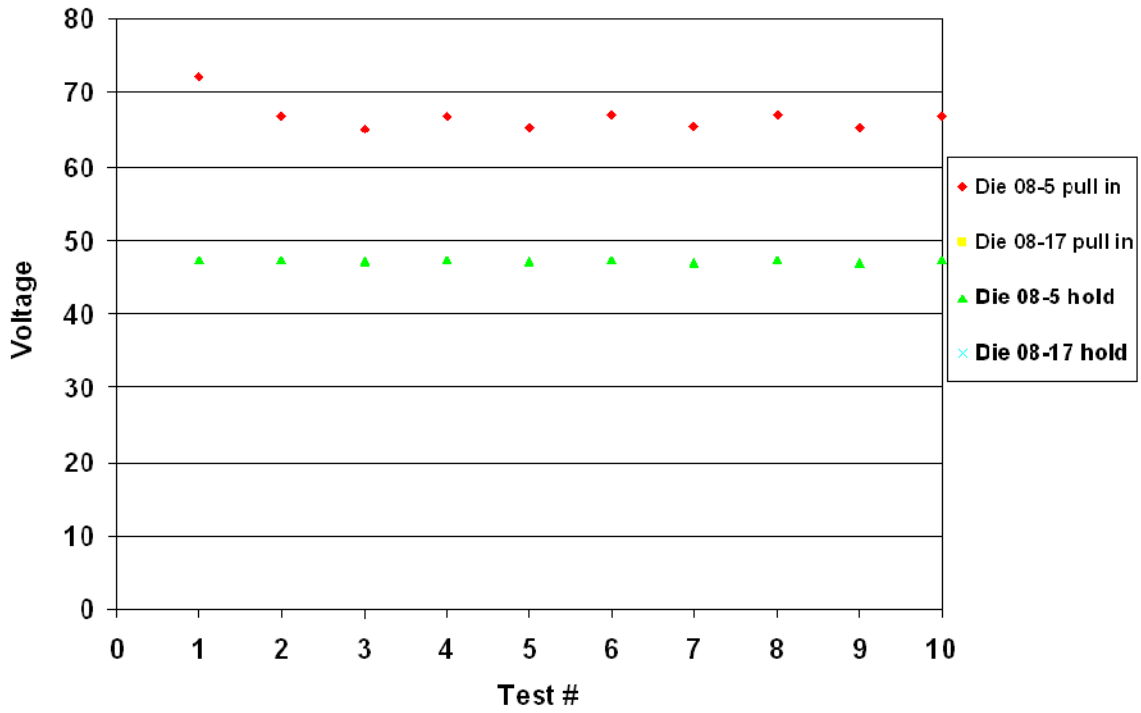
Voltage (y-axis), Test # (x-axis)
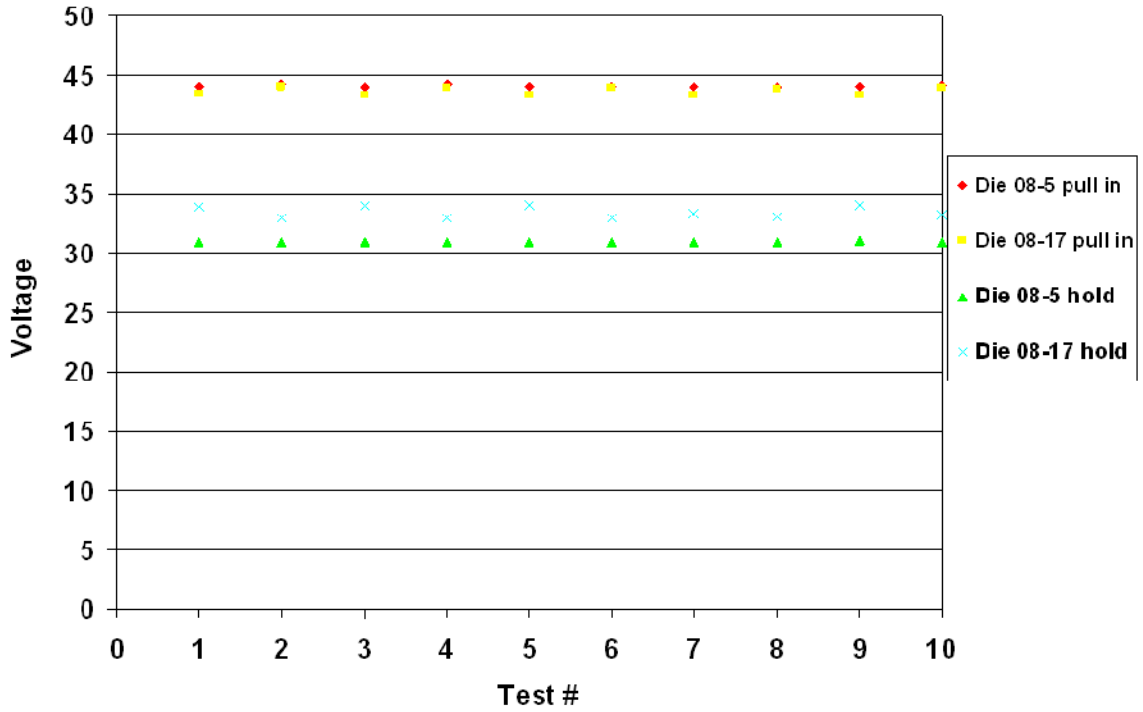
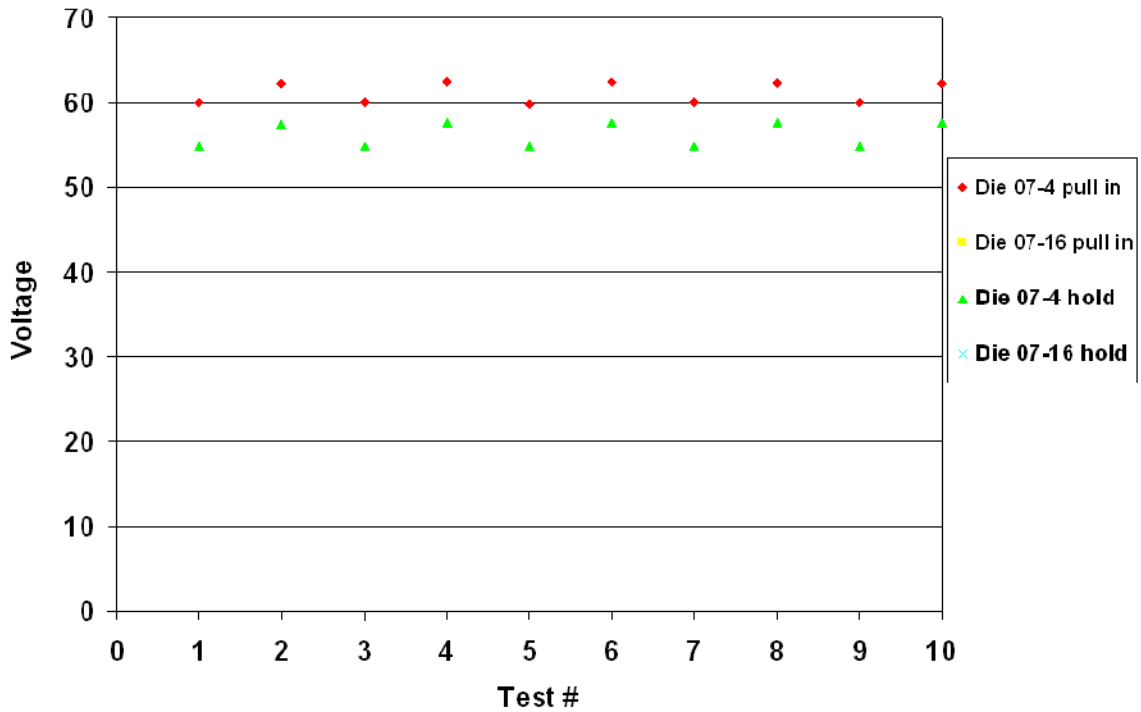# Die 08 Device 5 Right Al$_2$O$_3$ in Vacuum
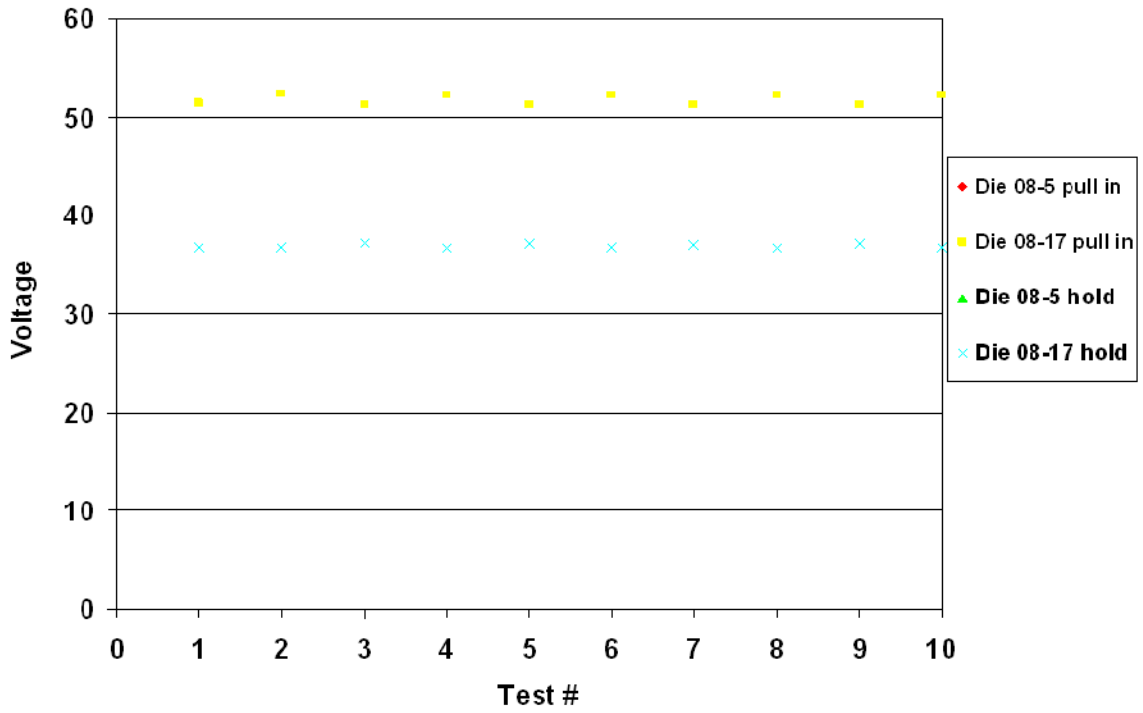
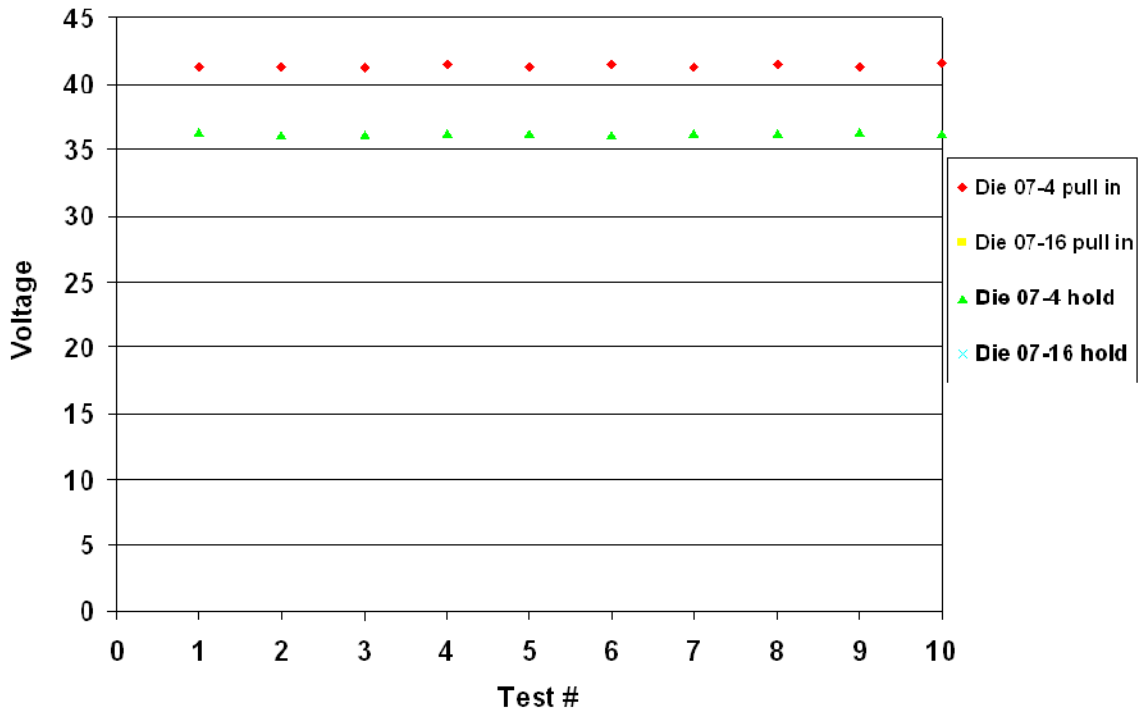# Die 08 Device 6 Right Al$_2$O$_3$ in Vacuum
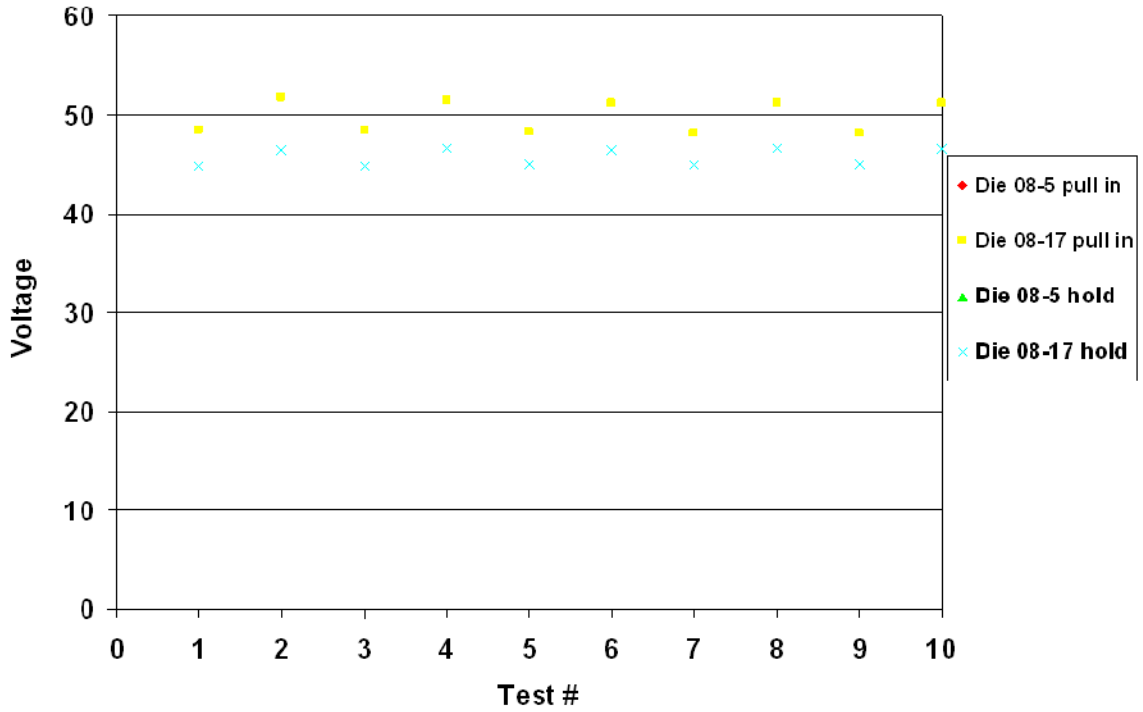
Die 08 Device 7 Right Al$_2$O$_3$ in Vacuum

Die 07 Device 1 Left Al$_2$O$_3$ in Vacuum

Die 07 Device 6 Left Al$_2$O$_3$ in Vacuum

Voltage vs Test #

Legend:
- ◆ Die 07-4 pull in
- ■ Die 07-16 pull in
- ▲ Die 07-4 hold
- × Die 07-16 hold

Die 07 Device 7 Left Al$_2$O$_3$ in Vacuum

Voltage vs Test #

Legend:
- ◆ Die 07-4 pull in
- ■ Die 07-16 pull in
- ▲ Die 07-4 hold
- × Die 07-16 hold

Die 07 Device 1 Right Al$_2$O$_3$ in Vacuum

Legend:
- ♦ Die 07-4 pull in
- ■ Die 07-16 pull in
- ▲ **Die 07-4 hold**
- × **Die 07-16 hold**

Y-axis: Voltage
X-axis: Test #

Die 07 Device 6 Right Al$_2$O$_3$ in Vacuum

Legend:
- ♦ Die 07-4 pull in
- ■ Die 07-16 pull in
- ▲ **Die 07-4 hold**
- × **Die 07-16 hold**

Y-axis: Voltage
X-axis: Test #
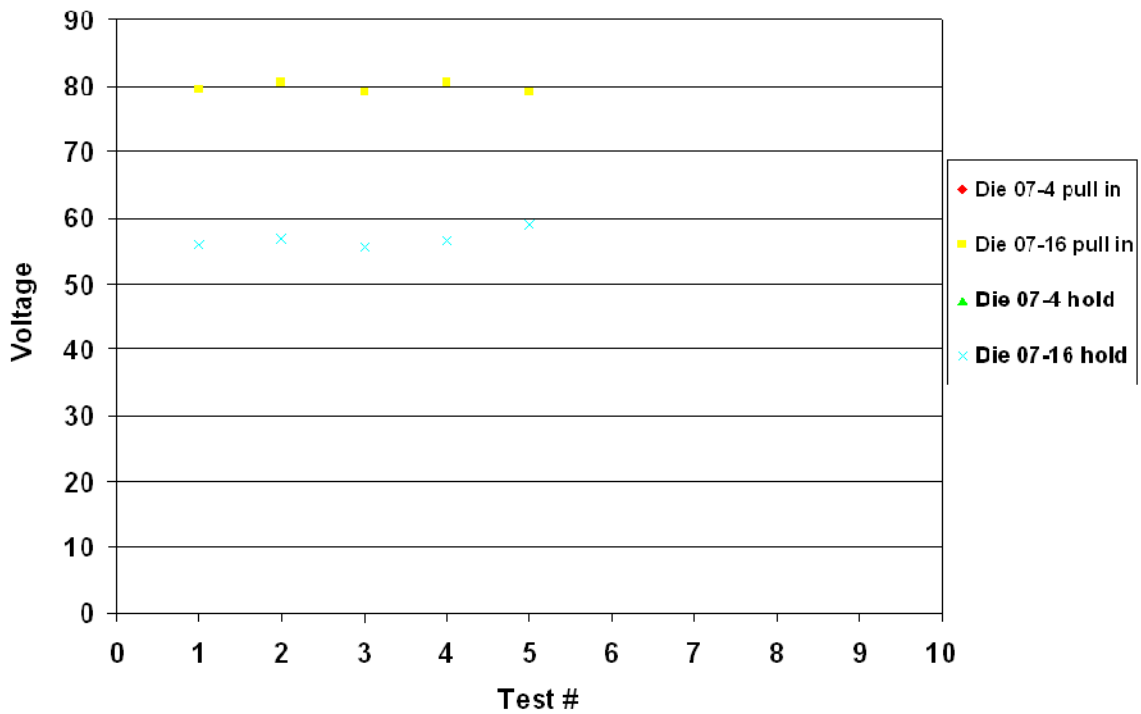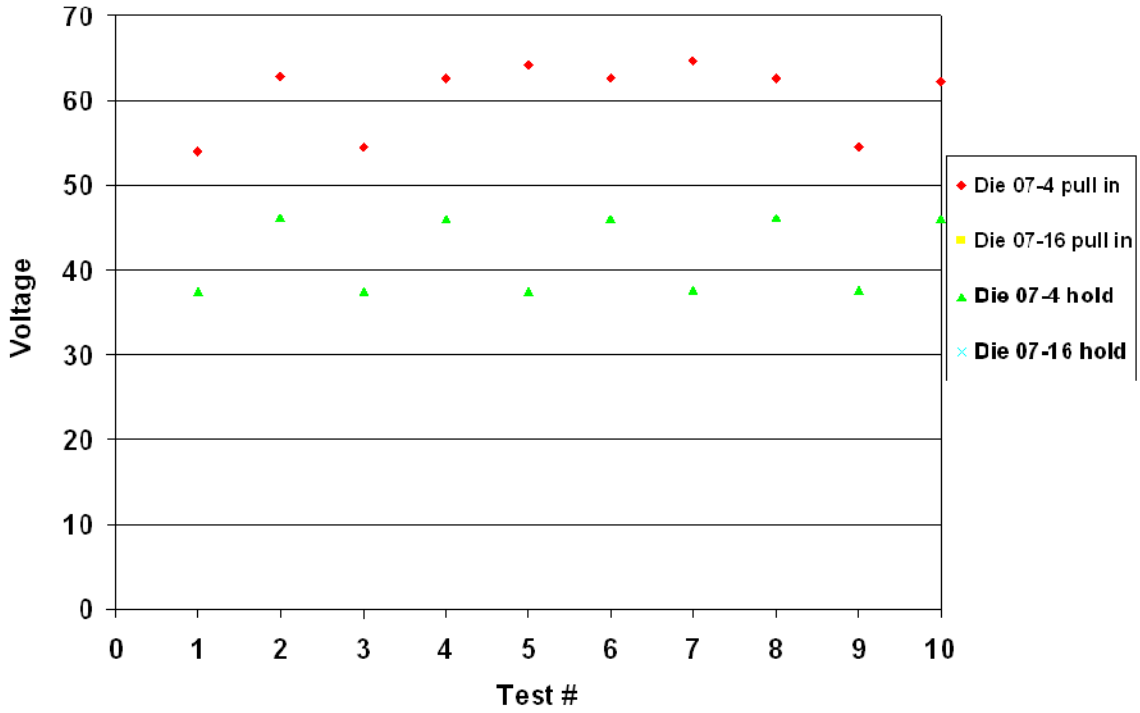
Die 07 Device 7 Right Al$_2$O$_3$ in Vacuum
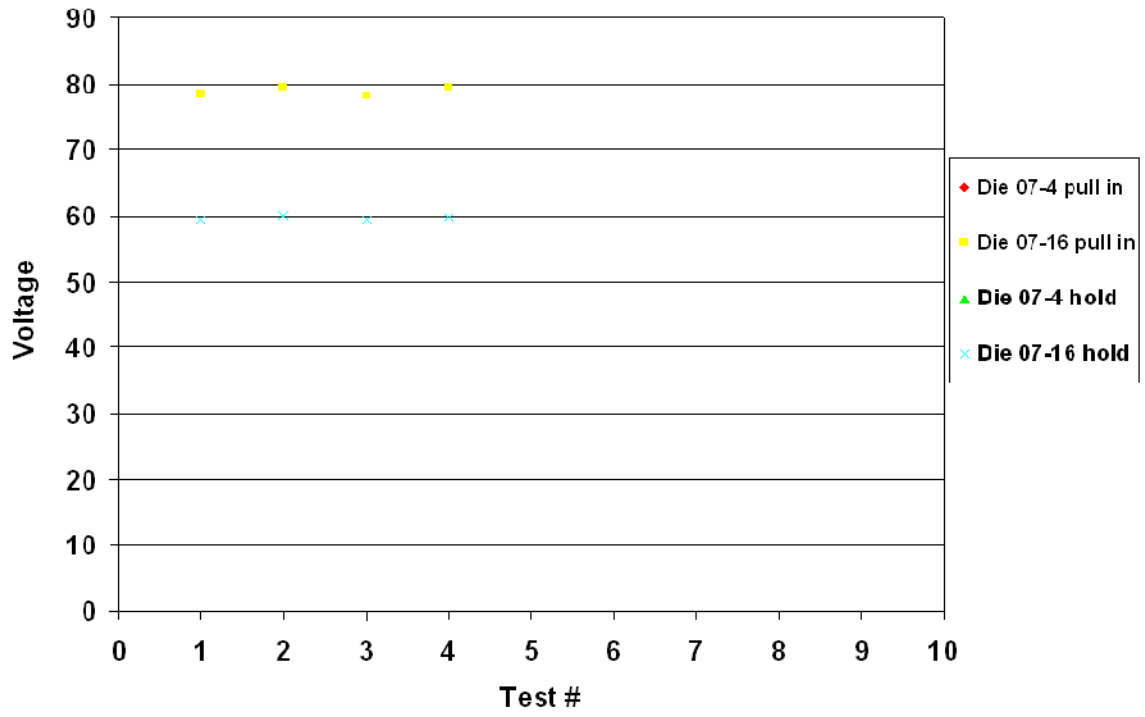
Distribution

1	MS1085	Grant Grossetete	01742	(electronic copy)
1	MS1080	David L. Luck	017491	(electronic copy)
1	MS1080	Gregory N. Nielson	017492	(electronic copy)
1	MS1069	Roy H. Olsson	017492	(electronic copy)
1	MS1080	Paul J. Resnick	017491	(electronic copy)
1	MS1080	Michael J. Shaw	017491	(electronic copy)
1	MS1085	Olga B. Spahn	01742	(electronic copy)
1	MS1082	Chris P. Tigges	01725	(electronic copy)
1	MS1082	Michael R. Watts	01727	(electronic copy)
1	MS1080	Keith Ortiz	01749	(electronic copy)
1	MS1069	Mark R. Platzbecker	017491	(electronic copy)
1	MS1077	Thomas E. Zipperian	01740	(electronic copy)
1	MS1085	Charles T. Sullivan	01742	(electronic copy)
1	MS1082	Frederick B. McCormick	01727	(electronic copy)
1	MS0123	Marie L. Garcia	01012	(electronic copy)
1	MS0123	Yolanda V. Moreno	01012	(electronic copy)
1	MS0351	Wendy R. Cieslak	01010	(electronic copy)
1	MS0351	Richard H. Stulen	01000	(electronic copy)
1	MS0899	Technical Library	09536	(electronic copy)
1	MS0123	Donna L. Chavez	01011	(electronic copy)